MASTER THESIS

Gas permeance characteristics of microporous polymer-derived ceramics

Technische Universität Wien
Institute of Chemical Technologies and Analytics
Getreidemarkt 9/164-CT
1060 Wien

Under supervision of
Ass.Prof. Dr. Thomas KONEGGER
Ao.Univ.Prof. Dipl.-Ing. Dr.techn. Roland HAUBNER

Felix Frank
Johannagasse 29-35/17/13
1050 Wien

Vienna, 15.04.2020

Acknowledgements

At first, I want to thank my advisors Roland Haubner and Thomas Konegger for making it possible to work on this topic. Without them and their instructions and help, this would all not have been possible.

Also, I want to acknowledge the funding of the project I was working on by the Austrian Science Fund FWF (P-29058).

I am also very thankful for all my colleagues at the working group 'high performance ceramics', especially for Christina Drechsel, who mentored me in the early stages of this work and was always there for me, when something did not go according to plan, and Johannes Rauchenecker, who also gave me valuable advice when I encountered problems.

I also want to acknowledge all people who are and were working in the second floor and who accompanied me through the time I was working on my thesis. I am sorry that I cannot name them all in this work, as each one of them deserves it.

My special thanks goes to all my friends offering me support, especially Felix Eder, who accompanied me the entire journey through the fascinating world that is chemistry, as well as my family, as without them, I would not be where I am today.

Last but not least, I want to thank my partner Christina, who provided me with unconditional support during my work and was never tired to cheer me up, whenever I was feeling down.

Abstract

For the separation of gas mixtures such as syngas produced during the steam reforming of hydrocarbons, the need of novel methods of gas separation for the purification of gases is steadily rising. The importance of pure gases is especially high for uses in fuel cells, as small impurities reduce their efficiency drastically.

The simplest theoretical method of separating larger gases from a small gas is size exclusion. It can be performed by using microporous asymmetric membranes with porosity smaller than 1 nm. The goal of this work was the realisation of this concept by applying layers of amorphous SiCN onto tubular supports. Further these membranes were characterised at increased temperatures.

The deposition of these layers was performed via dip-coating with polysilazane based pre-ceramic polymers. Hereby the aim was to establish a method that allows the consistent deposition of membrane layers in regard to their thickness and separation properties to maximise the selectivity of these membranes in the future. To form the aforementioned amorphous SiCN layers, the polymer layer was crosslinked in a first step and pyrolysed in a second step. As these polymers are very sensitive to water-containing atmospheres, all steps had to be performed under inert atmospheres.

To characterise the layers, a test rig was further assembled to create an environment in which the permeabilities of different gases and gas mixtures can be determined at different temperatures. The integration of the test rig was performed in a LabVIEW automated solution. A method was further developed to guarantee comparable results in the measurements.

Difficulties were encountered during the coating of the substrates, as no completely crack-free layers could be obtained. Nevertheless, promising separation properties could be observed for test membranes with low layer thickness to crack width ratio.

Kurzfassung

Um Gasmischungen wie Synthesegas, welches großtechnisch über das Steamreforming von Kohlenwasserstoffen erzeugt wird, effizient zu trennen, wächst der Bedarf an neuen Trennmethoden zur Aufreinigung von Gasen an stetig. Dieser Bedarf an hochreinen Gasen ist besonders bei Brennstoffzellen groß, da bereits kleine Verunreinigungen die Effizienz drastisch reduzieren.

Die theoretisch einfachste Methode, kleine Gase von größeren Gasen zu trennen, ist die Verwendung einer Größenausschlussmembran. Praktisch kann das erreicht werden, indem mikroporöse asymmetrische Membranen mit einem Porendurchmesser unter 1 nm eingesetzt werden. Das Ziel der Arbeit war, dieses Konzept zu verwirklichen, indem eine dünne Schicht amorphes SiCN auf tubulare Supports aufgebracht werden sollte und diese dabei entstandenen Schichten bei verschiedenen Temperaturen charakterisiert werden sollten.

Die Beschichtungen wurden mittels Dip-Coating in polysilazanbasierten präkeramischen Polymeren durchgeführt. Hier sollte eine Methode entwickelt werden, mit welcher eine reproduzierbare konsistente Beschichtung im Bezug auf Schichtdicke und Trennwirkung erreicht werden sollte, um die Selektivität dieser Membranen in weiterer Folge zu optimieren. Um die zuvor erwähnten amorphen Trennschichten zu erhalten, wurde die an der Oberfläche absorbierte Polymerschicht zunächst quervernetzt und schließlich pyrolysiert. Da die eingesetzten Polymere sehr hydrolyse- und oxidationsaffin sind, mussten alle Schritte unter inerten Bedingungen durchgeführt werden.

Um die so erhaltenen Schichten zu charakterisieren, wurde ein Prüfstand entwickelt, um ein System zu schaffen, in welchem die Permeabilitäten beliebiger Gase und Gasmischungen bei verschiedenen Temperaturen gemessen werden können. Der Prüfstand wird über eine LabVIEW integrierte Oberfläche zentral gesteuert und eine Methode entwickelt, um vergleichbare Ergebnisse zu erhalten.

Obwohl bei der Beschichtung der Substrate keine rissfreien Schichten erreicht werden konnten, wurden bei der Messung von Testmembranen mit niedrigem Riss- zu Schichtdickenverhältnis vielversprechende Trenneigenschaften beobachtet.

Contents

1 Introduction and motivation

In a world where alternative fuels such as hydrogen for use in fuel cells are steadily gaining importance, novel methods are required to efficiently separate hydrogen from other gases. This is insofar important, as the main source of industrial hydrogen is produced via the steam reforming process of hydrocarbons. In this process, hydrogen can be produced in a two step process, the first of which is the actual steam reforming, where hydrocarbons such as methane react with steam at high pressures and temperatures, forming syngas, a mixture of carbon monoxide and hydrogen with residues of the reagents. Carbon monoxide can further be used to produce hydrogen via the water gas shift (WGS) reaction:

$$\mathrm{CH_4 + H_2O \xrightarrow{T,p} H_2 + CO} \qquad \text{Steam reforming process}$$

$$\mathrm{CO + H_2O \xrightarrow{Cat,T} H_2 + CO_2} \qquad \text{WGS reaction}$$

Hydrogen produced over this route however is not directly suitable for the use in fuel cells, as fuel cells need very pure hydrogen. Even small amounts of CO reduce the efficiency of fuel cells dramatically, as shown in Fig. 1.[1]

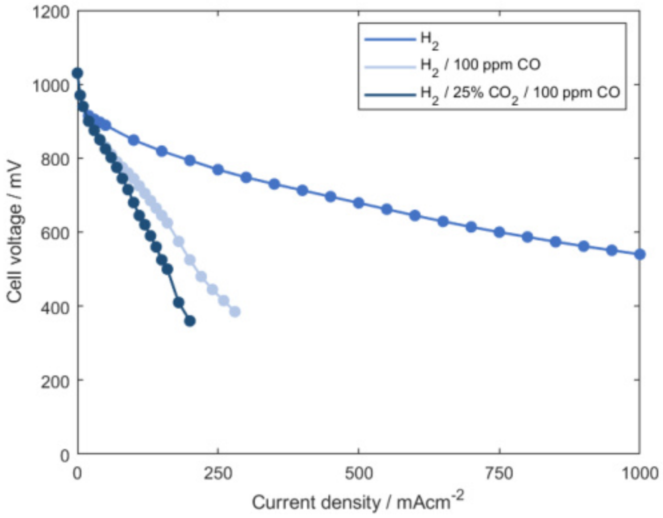

Figure 1: Effect of CO poisoning in fuel cells.[1]

As a result of this, cheap separation processes are needed to further establish hydrogen as a alternative to fossil fuels. One approach is the use of high performance membranes to lower the input energy and subsequently the cost of separation. Ceramic membranes hence show great promise, as they are very stable at high temperatures and many chemical environments. In contrast to sol-gel-derived silica membranes, which show instabilities in moist high temperature environments, and zeolite membranes, where high selectivities and acceptable permeances are very challenging to achieve,[2] ceramic membranes made over the pre-ceramic route seem to offer promising results. One example of such a membrane would be the application of polysilazane-based pre-ceramic polymer via dip-coating to obtain amorphous SiCN membrane layers, as described by Mori et al.[3]

The focus of the research done in this work was to build on the work done by Mori et al. by experimenting with parameters during the dip-coating process to optimise permeance characteristics and to measure these characteristics in a new measurement environment suitable for performing high temperature permeance experiments with different gas mixtures. This work is therefore divided into two main parts:

- the establishment of a method of preparation of asymmetric SiCN membranes by dip-coating tubular alumina supports, and
- the establishment of a membrane testing environment and the measurement of key properties of the prepared membranes.

2 Theoretical background

2.1 Non-oxidic silicon based ceramics

Silicon nitride

Silicon nitride is a very versatile and stable ceramic, which is suitable for many purposes in high temperatures and aggressive environments. Its only limitation is that it decomposes well before its melting point, which can therefore not be defined. As a consequence, silicon nitride has to be sintered using oxide additives such as Al_2O_3 and Y_2O_3.[4] Key properties of the ceramic are shown in Table 1. The properties of silicon nitride make it useful for a vast amount of high performance applications such as cutting materials, tubes, and generally parts subject to high stress.[5][6][7]

Table 1: Key properties of silicon nitride[5][6][7].

Decomposition point (°C)	1850
Max. operating temperature (°C)	
oxidising atmosphere	1300
neutral atmosphere	1600
Density (g/cm^3)	3.2
Young's modulus (GPa)	195
Flexural strength (MPa)	850
Fracture toughness ($MPam^{1/2}$)	7
Thermal conductivity ($Wm^{-1}K^{-1}$)	30.1
CTE ($10^{-6}/K$)	2.9

Silicon carbide

Silicon carbide is also a very stable ceramic with many uses in different fields of technology. It withstands even higher temperatures than silicon nitride and shows similar mechanical properties, however, due to its high melting point is also equally complex in its manufacturing. Key properties of the ceramic are shown in Table 2. These properties as well as the fact that silicon carbide shows semiconductive properties makes it perfect for uses in turbine components, heat exchangers and heating elements for electric furnaces.[8][9][10]

Table 2: Key properties of silicon carbide[8][9][10].

Decomposition point (°C)	2830
Max. operating temperature (°C)	
oxidising atmosphere	1600
neutral atmosphere	1800
Density (g/cm^3)	3.2
Young's modulus (GPa)	400
Flexural strength (MPa)	550
Fracture toughness (MPam$^{1/2}$)	4.6
Thermal conductivity (Wm^{-1}K^{-1})	120
CTE (10^{-6}/K)	4.0

2.2 Polymer-derived ceramics

Many silicon-based ceramics are very problematic in their preparation, as they cannot be sintered due to their high melting point. One way to overcome this is by the use of sintering additives, but even then, some ceramics cannot be shaped by conventional processes such as sintering. Because of that, ceramics produced by the pyrolysis of polymers have gained growing interest in recent years. The polymers used for that route of ceramic conversion are mostly containing silicon, however, also other high melting ceramics such as BN or TiN can be produced via this route.[11] Examples of such polymers are displayed in Fig. 2.

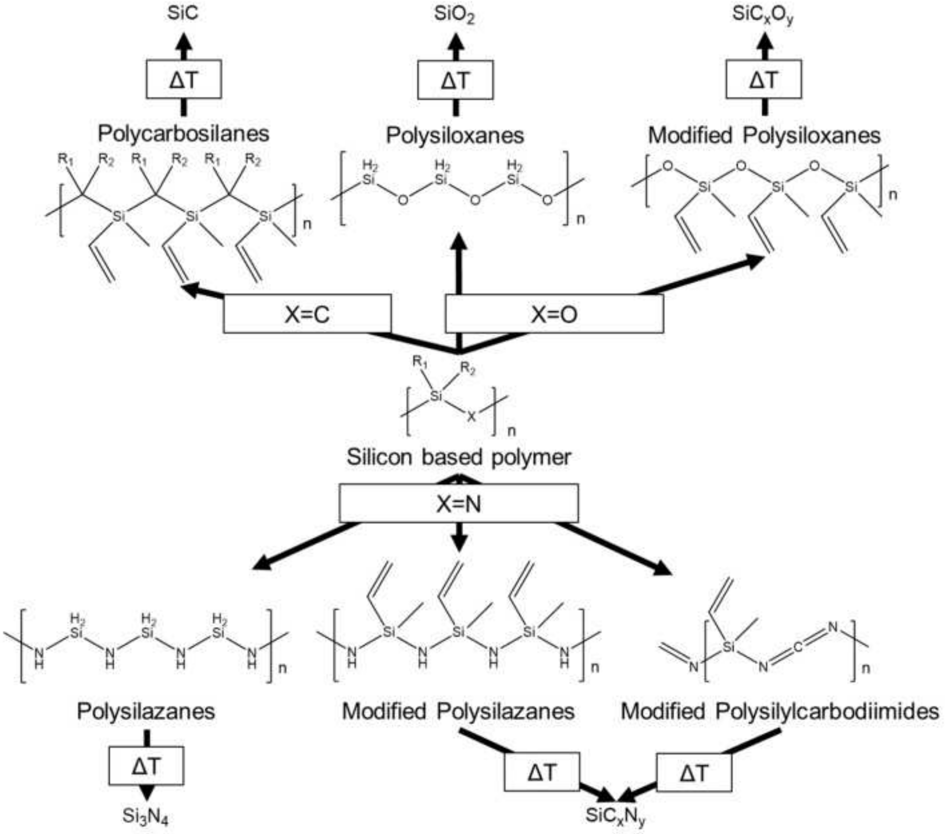

Figure 2: Schematic of different achievable ceramic materials via the pre-ceramic polymer route.

The process for the production is generally split in four parts:[12]

- Synthesis of the pre-ceramic polymer: Using chloro-organosilicon compounds as precursors, polymers can be synthesised for example by catalytic dechloronation.
- Shaping of the pre-ceramic polymer: Pre-ceramic polymers, which can either be solid or liquid, can be shaped by many different processes known in polymer science, such as injection moulding, pressing, or casting.
- Crosslinking of the shaped pre-ceramic polymer: After achieving the desired shape, the polymer has to be crosslinked at increased temperatures to stabilise that shape. This can be done in many different ways, depending on the side chains of the polymer precursor.

- Pyrolysis of the crosslinked polymer: To complete the polymer-ceramic conversion, the crosslinked polymer has to be heated to temperatures up to 1000 °C, leading to the exposition of gaseous decomposition products depending on the used polymer and the formation of the ceramic residue.

2.3 Porous ceramics as separation layers in membranes

By varying the temperature of pyrolysis, many key properties such as pore volume in porous ceramics can be controlled,[13] shown in Fig. 3.[14] One cannot, however, control pore size that way, as it seems to be determined by other parameters, which is shown in Fig. 4.[14]

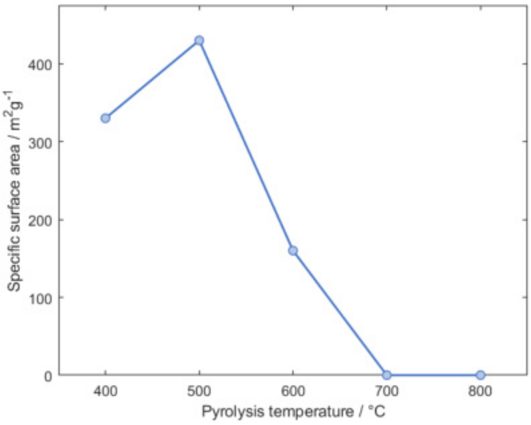

Figure 3: Resulting specific surface area when performing pyrolysis of a polyvinylsilazane at different temperatures.[14]

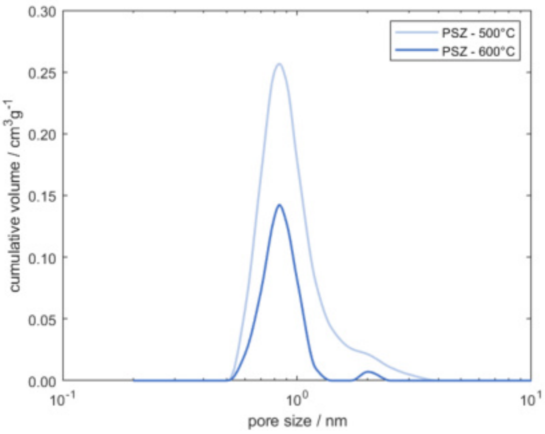

Figure 4: Resulting pore size distribution when performing pyrolysis of a polyvinylsilazane at different temperatures.[14]

The pore size of porous materials is a very important parameter for the efficiency and separating ability of size exclusion membranes. That makes a consistent definition of the term 'pore size' indispensable. In this work, all definitions are in accordance with those proposed by IUPAC.[15] Some especially important definitions are listed below:

- Pore size (or pore width) is defined as the diameter of a cylinder fitting into the smallest dimension of the pore.
- Pore sizes are categorised into three rough groups: Microporosity (with pore sizes smaller than 2 nm), mesoporosity (with pore sizes between 2 and 50 nm) and macroporosity (with pore sizes larger than 50 nm)

As this work is focused on the size exclusion separation of very small gases such as hydrogen, the focus will be laid on microporous materials. In Fig. 4, it is shown that microporosity can be reached if pre-ceramic polymers are pyrolysed, leading to pore sizes under 1 nm.[14]

To realise the concept of such a membrane, three basic elements of the membrane should be implemented:[16][17]

- A microporous separation layer, tailored to meet the requirements to separate the gas mixture efficiently
- A macroporous bulk to provide mechanical stability, as a microporous bulk would drastically reduce the permeability and thus the efficiency of the membrane
- A mesoporous intermediate layer to combat adhesion problems between the microporous and macroporous layers and to prevent the infiltration of the macroporous bulk with microporous material

This results in an asymmetric membrane design, which is schematically shown in fig. 5.

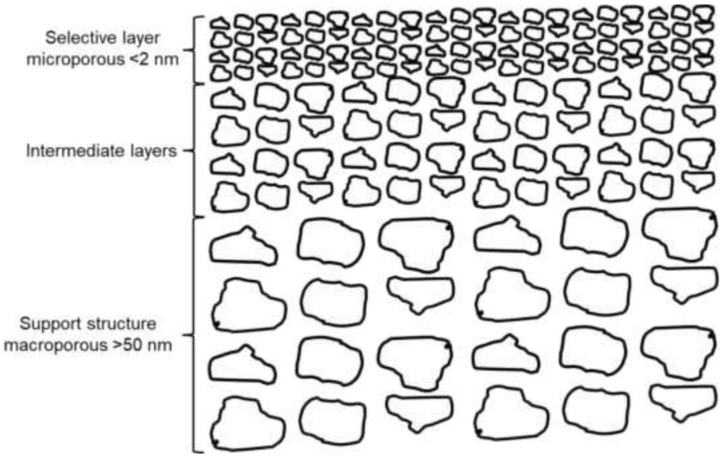

Figure 5: Schematic design of an asymmetric membrane.

2.4 Deposition of thin layers onto porous substrates

For the application of thin layers onto a substrate, many different techniques have proved to produce promising results, such as PVD, CVD, and various sol-gel processes. However, only some of them are suitable for the use with pre-ceramic polymers. In this work, the focus will be laid on dip-coating, in which the substrate is immersed in a liquid containing the coating material and subsequently pulled out of the liquid at a constant speed, leaving behind a thin layer. This process is schematically shown in Fig. 6.

The thickness of this layer h can be predicted by the Landau-Levich model (1),[18] where μ is the viscosity of the solution, U is the withdrawal speed, σ is the surface tension of the liquid, ρ is the density of the liquid, while g being gravity.

As can be seen in (1), the layer thickness of a dip-coated sample depends on liquid parameters such as the viscosity, surface tension, and density, as well as the withdrawal speed. The faster the substrate is removed from the coating liquid, the thicker the layer gets.

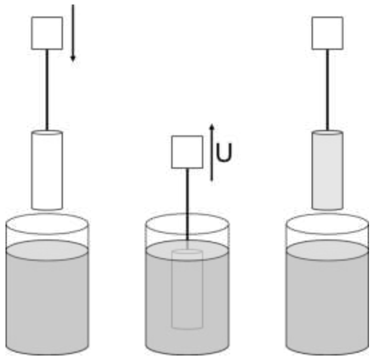

Figure 6: Schematic design of a dip-coating experiment.

$$h = 0.944 \left(\frac{\mu U}{\sigma}\right)^{\frac{1}{6}} \left(\frac{\mu U}{\rho g}\right)^{\frac{1}{2}} \tag{1}$$

2.5 Gas transport through membranes

To describe the process of the permeance of membranes consistently, a few parameters have to be defined: The mass flux F is the amount of gas which is being transported through the membrane for a standardised membrane area. The permeance P is defined as mass flux per pressure difference between the two sides of the membrane. For the selectivity, it has to be differentiated between two terms: the ideal selectivity n_{th} and the actual selectivity n_{real}. The ideal selectivity is the ratio of the permeances of two gases measured independently, whereas the actual selectivity is the ratio of the permeances of two gases measured as mixture. Equations used in this work to calculate these parameters are listed below in (2)-(3). In these equations, the two differentials are pressure increases caused by the membrane and by the leakage of the measurement system, V is the downstream volume, A is the membrane area, R is the universal gas constant, T is the temperature while Δp being the difference in pressure between the measurement cell and the feed.

$$F = \frac{(\frac{\mathrm{d}p}{\mathrm{d}t} - \frac{\mathrm{d}p_{leak}}{\mathrm{d}t})V}{ART}, \quad [F] = mols^{-1}m^{-2} \tag{2}$$

$$P = \frac{F}{\Delta p}, \quad [P] = mols^{-1}Pa^{-1}m^{-2} \tag{3}$$

For micropores, the two main forms of gas transport through membranes are Knudsen diffusion (for larger pores) and molecular sieving (for smaller pores, pore size has to be tailored exactly for the gas mixture to be separated properly).

If the mean free path of gases travelling through tubes (which can be applied to pores of membranes equivalently) is much larger than the diameter of the tube (and thus the pore size), Knudsen diffusion occurs. The mean free path of gases λ can be calculated by (4), where $\frac{N}{V}$ being the number of gas molecules per volume and d is the particle diameter. Assuming ideal gas properties $\frac{N}{V}$ can be substituted by $\frac{p}{kT}$, making the free path dependant on the pressure and the particle size. In Table 3, kinetic diameters of some gases[19][20][21] together with the resulting mean free paths (at 25 °C, 1 bar) are listed.

If micropores with pore diameters of below 2 nm are assumed, the mean free paths of all gases are high enough to assume Knudsen diffusion. For Knudsen diffusion, the permeabilities of gases are directly proportional to $\frac{1}{\sqrt{M}}$.[22] With that, theoretical Knudsen selectivities (n) for the gases in Table 3 can be calculated, which are listed in Table 4.

$$\lambda = \frac{1}{\sqrt{2}\pi\frac{N}{V}d^2} \tag{4}$$

Table 3: Mean free paths of different gases at 25 °C, 1 atm.

Molecule	Kinetic diameter (nm)	λ (nm)
H_2	0.29	110
He	0.26	137
CH_4	0.38	64.1
C_2H_6	0.39	60.9
N_2	0.36	71.5
O_2	0.35	75.6
CO_2	0.33	85.0

Table 4: Theoretical Knudsen selectivities of different gases.

Molecule	M (g/mol)	$\frac{1}{\sqrt{M}}$ ($mol^{\frac{1}{2}} g^{-\frac{1}{2}}$)	n(H_2/X)	n(He/X)
H_2	2	0.71		
He	4	0.50	1.4	
CH_4	16	0.25	2.8	2.0
N_2	28	0.19	3.7	2.6
C_2H_6	30	0.18	3.9	2.7
O_2	32	0.18	4.0	2.8
CO_2	44	0.15	4.7	3.3

For molecular sieving, as said before, the size of the pores have to be tailored exactly to achieve the desired effect. The reason for that is, that in contrast to Knudsen diffusion, the separation does not happen because of different diffusion speeds,[22] but rather because of size exclusion of larger gas particles. This leads to much higher selectivities, as shown by Ding et al., who reached H_2/CO_2 selectivities larger than 160 (compared to the Knudsen selectivity of 4.7).[23] The difference between the two ways of gas transport through membranes is shown schematically in Fig. 7.

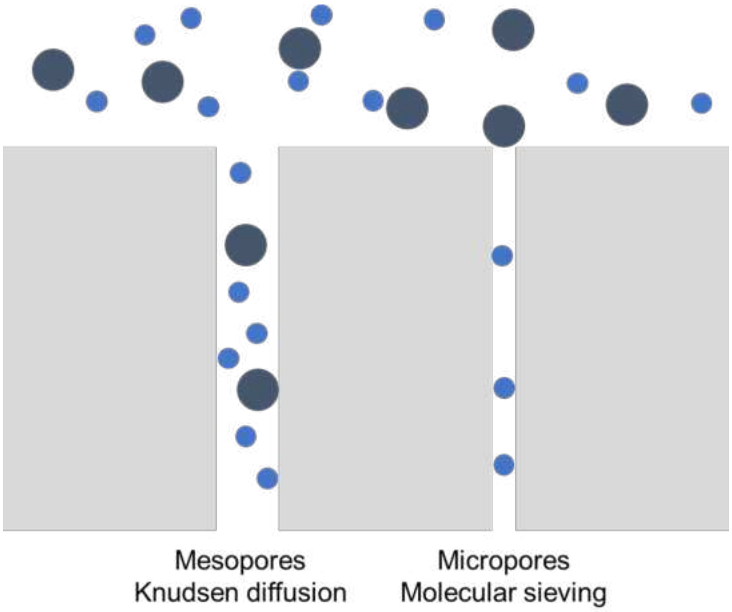

Figure 7: Schematic difference between Knudsen diffusion and molecular sieving.

3 Experimental

3.1 Materials

In Table 5, all used materials used for the experimental part are shown. The polyvinylsilazane is a commercially available polymer, where 20 percent of the silicon atoms are substituted with a methyl and a vinyl group, whereas the other 80 percent are merely substituted with a methyl group. An exemplary structure of the polymer is shown in Fig. 8. The data on the test tubes as received by atech innovations GmbH is shown in Table 6 and a picture of a 25 mm raw substrate tube as recieved is shown in Fig. 9.

Table 5: Materials used in the experimental part.

Name	Producer	Chemical Formula
Durazane 1800 (PSZ)	durXtreme GmbH	See Fig. 8
Dicumylperoxide (DCP)	Fluka	$[C_6H_5C(CH_3)_2]_2O_2$
Alumina substrates	atech innovations gmbh	Al_2O_3

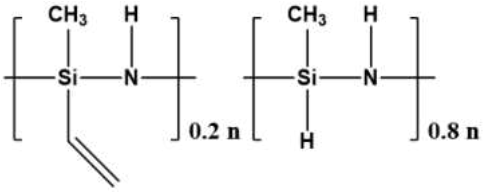

Figure 8: Structure of the used pre-ceramic polymer.

Table 6: Data provided by atech innovations GmbH regarding the substrate tubes.

Material bulk support	Al_2O_3
Material membrane layer	Al_2O_3
Pore size membrane layer	0.05 µm
ID	6 mm
OD	10 mm
length	25/50 mm[1]

---

[1] 25 mm samples were used for coating experiments, 50 mm samples were used for permeance experiments

Figure 9: Picture of a 25 mm substrate tube as recieved.

3.2 Characterisation of the substrate tubes

The test tubes were characterised with regard to their porosity, pore structure, and their surface properties. For that, the porosity was determined geometrically, the pore distribution was measured using mercury porosimetry (ThermoScientific Pascal 140/440), whereas the surface and a cross section was examined via scanning electron microscopy (FEI Quanta 200). For the geometrical determination of the average porosity $\bar{p}$ of the sample tubes, their geometry was assumed as a perfect hollow cylinder with a density $\rho(\text{sample})$ calculated as in (5) and a porosity as in (6). In these formulas, m is the mass of a test tube with a length of L (the experiment was performed with two cut off rings with a length of 4.2 mm each), while $O.D.$ and $I.D.$ being their outside and inside diameters. For the cross section, a thin ring was cut from the sample tube and subsequently broken to avoid alteration of the layer formed during cutting. A schematic of the observation angles of the layers is shown in Fig. 10.

While cleaning the sample, it was observed that the mesoporous intermediate layer is prone to deterioration while being cleaned in an ultrasonic bath. Thus, cleaning of the samples was performed only by thoroughly rinsing the samples with isopropyl alcohol (IPA) and leaving it in a drying oven for 30 minutes at 110 °C, allowing excess IPA to evaporate.

$$\rho(sample) = \frac{m}{\left(\frac{O.D.-I.D.}{2}\right)^2 \cdot \pi \cdot L} \tag{5}$$

$$\bar{p} = 1 - \frac{\rho(sample)}{\rho(Al_2O_3)} \tag{6}$$

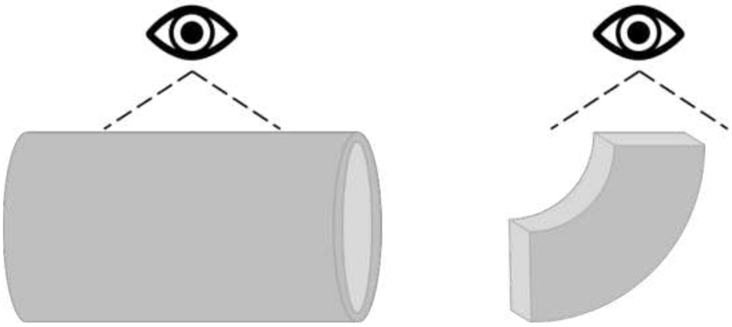

Figure 10: Observation angles of the layers during examination via scanning electron microscopy.

3.3 Preparation of the membrane layers

The coating of the samples was performed by dip-coating the plugged sample into a 1 wt% solution of DCP in PSZ. A picture of the dip-coating setup is shown in Fig. 11. The dip-coater is a custom-built Arduino-based system. It consists of a clamp, where the sample substrates can be fixed to, and a stepper motor responsible for dipping parameters such as the dipping and withdrawal speeds as well as the holding time in the liquid.

Figure 11: Setup used for dip-coating.

The coating procedure performed in this work was done as follows: The samples were plugged with PP vial caps and attached to the dip-coater. Hereby was important that the sample was hanging perpendicularly to the surface of the coating liquid to assure uniform coating. The samples were lowered until they were completely submerged by the polymer, held here for a set time of 1 second and raised again at a set speed, which was varied to achieve different layer thicknesses. After the sample had no more contact to the liquid, the plugs were removed from the sample and the coated sample was put into an oven, where the sample was crosslinked for 12 h under a nitrogen flow of 0.4 L/min at 130 °C, with the heating performed with a ramp of 1 K/min.

Following that step, it was possible to keep the samples at atmospheric conditions for the characterisation of the layer, as nearly all reactive silicon atoms were crosslinked.

After crosslinking, the samples were once again put into an oven, where the layer was pyrolysed for 4 h under a nitrogen flow of 0.4 L/min at 600 °C. The heating was divided into two steps with different ramps, at first, a ramp of 3 K/min was used until a temperature of 300 °C was reached, after that, heating was performed with a ramp of 1 K/min.

Schematic summaries of the temperature programs of the process and the chemical structures of the separation layers after each step are shown in Fig. 12 and Fig. 13.

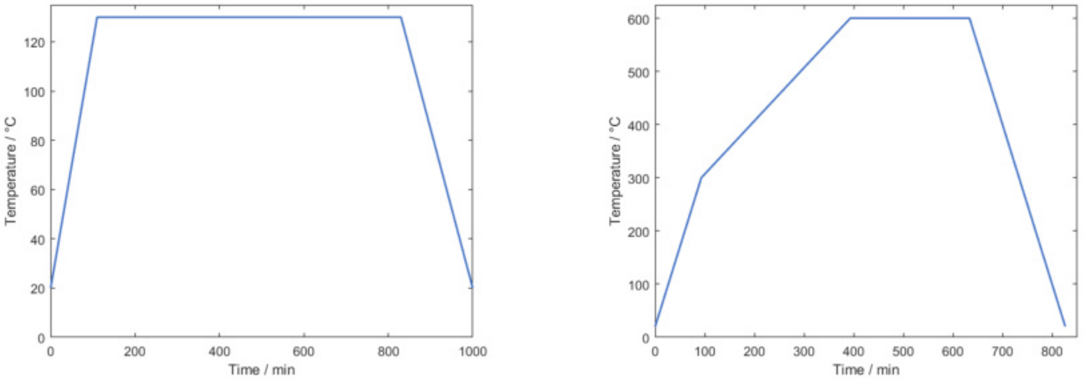

(a) During crosslinking

(b) During pyrolysis

Figure 12: Temperature programs for the two heat-treatment steps.

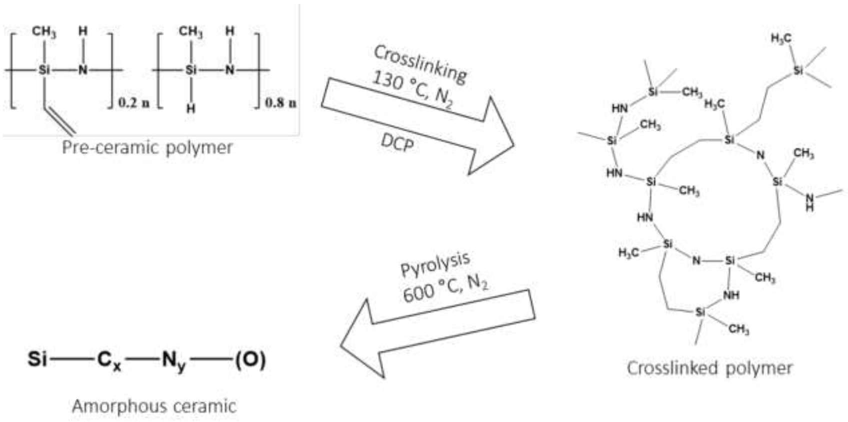

Figure 13: Schematic summary of the process steps performed during coating.

In this work, mostly the withdrawal speed of the coating steps has been varied in regard to the Landau-Levich model ((1) on page 9), making the other variables of the equation constants. In Table 7, a summary of all experiments performed with regard to the quality of the membrane layers in this work is shown. For the summary of samples prepared for the use in permeance experiments, see Table 8.

Table 7: Withdrawal speed parameters of the experiments performed.

Sample no.	1. coating	2. coating	3. coating
1	20 mm/min		
2	50 mm/min		
3	140 mm/min	50 mm/min	
4	300 mm/min		
5[1]	300 mm/min		
6	140 mm/min	100 mm/min	50 mm/min
7[2]	140 mm/min	120 mm/min	50 mm/min
8	140 mm/min	140 mm/min	
9[3]	140 mm/min	120 mm/min	
10[3]	140 mm/min	140 mm/min	
11	140 mm/min	100 mm/min	140 mm/min

---

[a] coating step performed with cooled polysilazane to increase viscocity

[b] delamination of membrane layer after third coating step, not examined via scanning electron microscopy

[c] coated twice without pyrolysis step between the two coating steps

Table 8: Withdrawal speed parameters of the experiments performed to obtain membranes for testing.

Sample no.	1. coating	2. coating	3. coating
1p	140 mm/min	140 mm/min	
2p	140 mm/min	100 mm/min	50 mm/min
3p	140 mm/min	100 mm/min	

3.4 Characterisation of the membrane layers

The membrane layers were characterised with regard to their surface properties (such as the microstructure and morphology), as the pore distribution could not be measured with mercury porosimetry due to their microporosity. To measure the pore distribution, other methods such as nitrogen physisorption are suitable, which were not used in this work, need be used. For the surface properties, the surface and a cross section as shown in Fig. 10 were examined via scanning electron microscopy (Quanta 200) and compared with the surface of the uncoated samples.

For the samples measured in the test rig, only the surface was examined, as the properties of the cross section were assumed the same as in the test sample. Before measuring, the membranes were only examined using an optical microscope to rule out large defects. The reason for that is, that the layers can delaminate when being removed from the carbon tape used for SEM. Therefore, examination of the membrane layers via SEM was performed after testing of separation characteristics.

4 Realisation of the membrane test rig

4.1 Requirements for the completed test rig

The main goal of the work was the realisation of a membrane test rig and the implementation of an automated software solution to control each part of the test rig remotely. The completed test rig should be able to fulfil the following tasks:

- Measure the permeance of single gases through microporous membranes at different temperatures up to 500 °C
- Measure the selectivity of microporous membranes for gas mixtures containing nitrogen, helium, methane, ethane, carbon dioxide and hydrogen at different temperatures up to 500 °C

4.2 Planning of the test rig

To achieve the two tasks the test rig should be able to perform, a blueprint of such a test rig had been designed in the research group prior to this work. The blueprint and a division into the five core elements of the test rig is shown in Fig. 14, whereas in Fig. 15, a picture of the completed test rig from above is shown. These five core elements are:

1. A console to feed different gas mixtures into the system
2. An extra line to further feed nitrogen into the downstream area if its pressure is not sufficient to start gas chromatography experiments
3. A furnace in which the samples can be mounted and heated to reach the target temperature
4. A steel cylinder raising the volume of the downstream area to improve the sensitivity of the permeance measurement
5. A gas chromatograph to measure the selectivity of the membranes for different gas mixtures

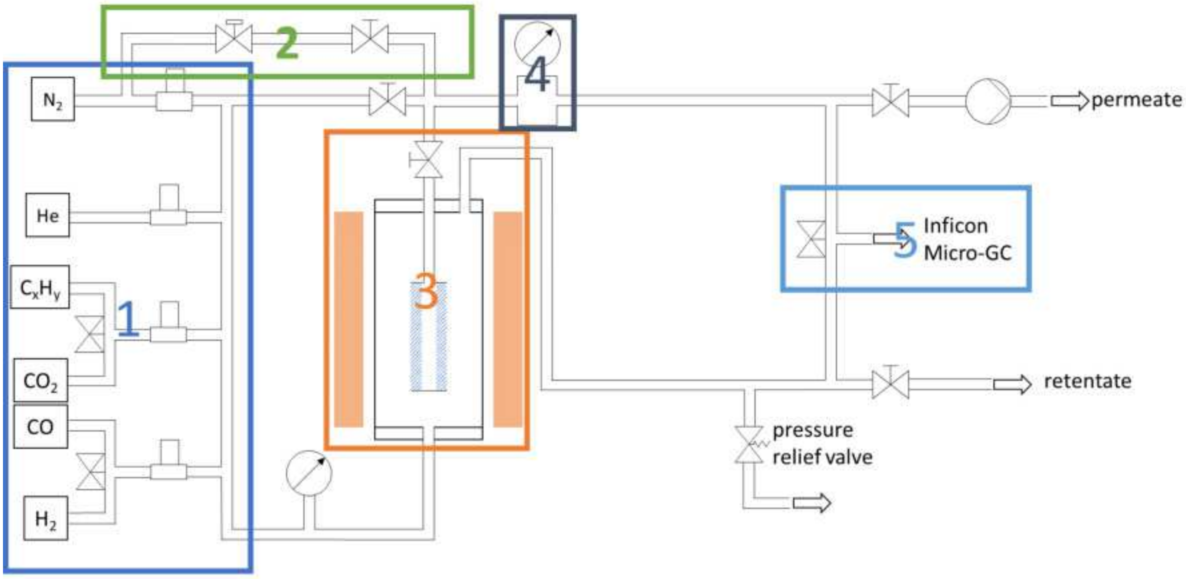

Figure 14: Sketch of the test rig.

Figure 15: Picture of the completed test rig from above.

4.3 Integrated components

4.3.1 Gas mixture console

To perform multi gas permeance experiments, a gas mixture console had to be planned. To reduce dead volume, the four mass flow controllers (MFCs) were mounted on a platform as shown in Fig. 16.

The console consists of 4 mass flow controllers (MKS Instruments: type GE50A) with maximum flow rates of 500, 200, 100, and 20 sccm. The 500 sccm MFC is here used for feeding nitrogen, the 200 sccm MFC for Helium, the 100 sccm MFC for hydrocarbons and carbon dioxide and the 20 sccm MFC is used for feeding safety-relevant gases such as hydrogen and, if required in the future, carbon monoxide. They are connected to the LabVIEW automated MKS PAC 100 CPU via a serial connection, which is further explained in chapter 4.4.

Figure 16: Gas mixture console implemented in the membrane test rig.

The ratio of the partial pressures of the feed gas mixture is approximated by the ratio of the single gas flows as shown in (7), where p is the partial pressure of the test gas or the total feed pressure while $\dot{V}$ being the gas flow rate of the test gas or the total feed flow.

The total feed pressure is measured by a MKS Instruments Baratron Type 722B Absolut Pressure Transducer with a pressure range of 0-2666 mbar, which is also connected to the LabVIEW automated MKS PAC 100 CPU via a serial connection.

$$\frac{p_{gas}}{p_{total}} = \frac{\dot{V}_{gas}}{\dot{V}_{total}} \tag{7}$$

4.3.2 Permeation system

The feed gas flows into a Carbolite Gero EST 1200 split tube oven with a Eurotherm 2132 temperature controller as overtemperature protection (set at 520 °C) and a Eurotherm 3508 temperature controller (controlled by a LabVIEW integrated solution, described in chapter 4.4), where the sample membrane is mounted as shown in Fig. 17.

In a permeation experiment, gas streams by the membrane and a fraction of it permeates through the membrane (permeate). The rest, which is held back by the membrane, exits the furnace and leaves the test rig through the exhaust (retentate). The process of this permeation experiment is schematically shown in Fig. 18.

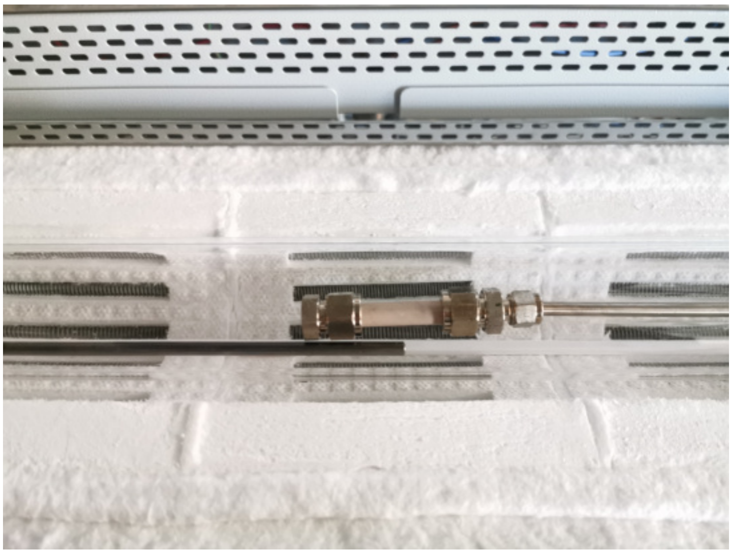

Figure 17: Sample mounted in the furnace.

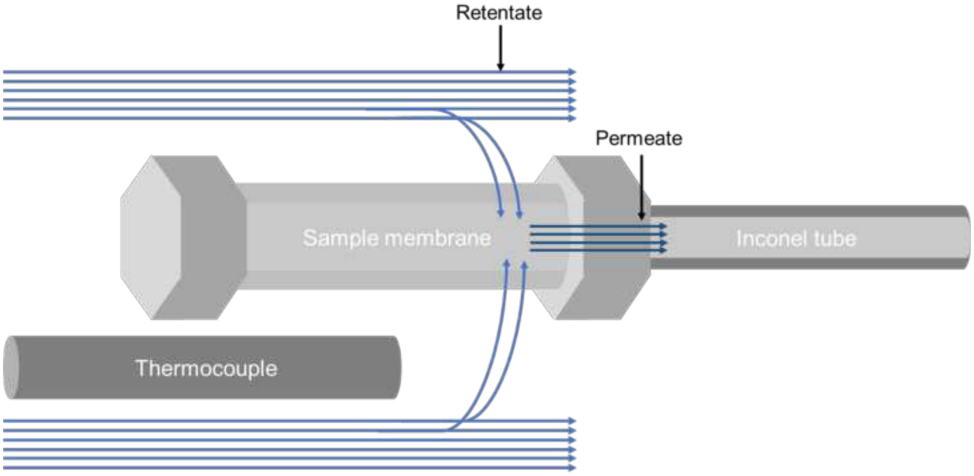

Figure 18: Schematic procedure of a permeation experiment.

The permeate then leaves the furnace and enters the downstream area, which was evacuated prior to the experiment, where the pressure slowly rises. This pressure increase is measured by a MKS Instruments Baratron Type 722B Absolute Pressure Transducer with a pressure range of 0-133 mbar and logged with the LabVIEW automated MKS PAC 100 CPU. As the feed gas total pressure stays constant over the course of the experiment, the pressure difference Δp as used in (3) on page 10 decreases over time, thus leading to a slower permeation as shown in the same equation. It can however be assumed, that a pressure increase of less than one percent of the feed pressure is almost negligible, which allows that small pressure increases can be seen as linear, as shown in Fig. 19.

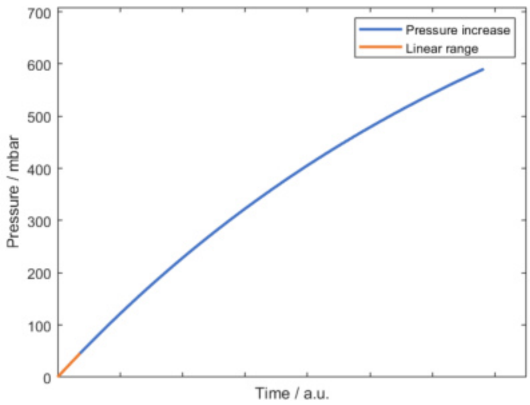

Figure 19: Pressure over the course of a permeation experiment.

4.3.3 Gas analysis

If a gas mixture is used as feed gas, the composition of this mixture as well as the permeate composition have to be determined. For that, a two module Inficon Micro GC Fusion gas chromatograph (Fig. 20) is utilised. The two modules feature different type of columns to analyse as many gases as possible. Module A features a Molesieve 5A column, making it possible to analyse hydrogen, oxygen, nitrogen, methane and carbon monoxide, whereas module B features a PLOT Q column, making it possible to analyse water, methane, carbon dioxide, ethane, acetylene, propane, propylene, C4-C8 hydrocarbons and hydrogen sulfide. In both columns, a thermal conductivity detector is used.

In Table 9, instrument parameters during the Micro GC measurements are listed. These parameters stay constant during the course of the experiment with the exception of the column temperature of module B, which starts heating with a rate of 1.5 K/s 20 seconds after the start of the measurement to elute bigger hydrocarbons in a reasonable time.

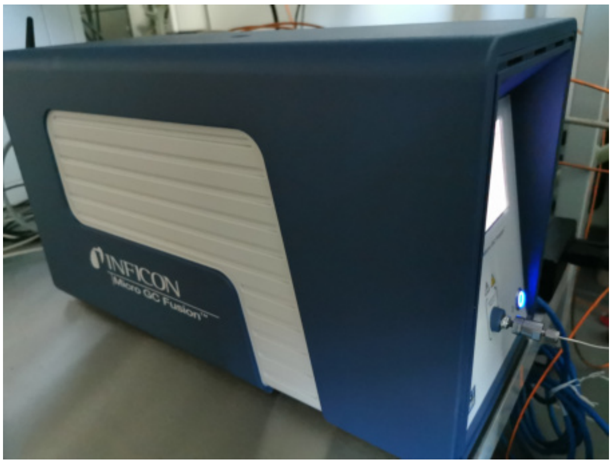

Figure 20: Picture of the Inficon Micro GC Fusion.

Table 9: Instrument parameters during the Micro GC measurements.

	Module A	Module B
Front entry temperature	100 °C	100 °C
Run time	140 s	140 s
Flow manifold heating	55 °C	55 °C
Injection temperature	90 °C	90 °C
Column temperature	90 °C	60 °C
Column pressure	30 psi	20 psi
Detector temperature	85-90 °C	85-90 °C

4.4 Automation of the test rig

The PAC 100

As already stated in chapter 4.1, one of the main goals for the completed test rig was its automation and the possibility of a remote control panel. To achieve that, all parts of the test rig but the furnace temperature control are connected to a central CPU, the MKS Instruments PAC 100. The PAC 100 is a modular system, which consists of a main CPU, onto which different modules can be stacked. In Fig. 21,[24] a typical PAC 100 module stack is shown as displayed in the PAC 100 user manual.

Figure 21: Picture of a typical PAC 100 module stack.[24]

In this stack, the leftmost module is the CPU, whereas the other modules are adding the possibility to add more input/output devices. In the PAC 100 customised for this work, an analog I/O module, where thermocouples can be connected to, a digital I/O module, where solenoid valves and the vacuum valve can be connected to and modules for the MFCs and Baratrons to be connected to were stacked. The CPU was connected to two 24 V power sources (one for the CPU and the modules, respectively; the CPU requires 5 A maximum current whereas the I/O modules require 12 A maximum current), connected to the master computer via Ethernet and put into a case. A photo of the whole setup inside the case is shown in Fig. 22.

Figure 22: Picture of the PAC 100 setup inside the case.

Automation of the PAC 100

The communication between the PAC 100 and the master computer works over Modbus TCP/IP. In this communications protocol, a single IP address is separated into multiple registers. This makes it possible to connect multiple devices to the same network. There are two separate connections for the PAC 100 and the Eurotherm 3508. In Table 10, relevant Modbus register addresses and functions for the two connections are listed.

Table 10: Relevant Modbus register addresses and their function.

Modbus register	Commands	Function
	PAC 100	
11000	Read Input Registers	Read TC temperature values
14000	Read Input Registers	Read processed MFC flow values
14000	Write Input Registers	Write MFC flow values
14300	Write Single Register	Control valves
15000	Read Input Registers	Read Baratron pressure values
	Eurotherm 3508	
1	Read Input Registers	Read current furnace temperature
2	Write Single Register	Write temperature set point

These Modbus register commands are then fed into the MB Modbus Master Query function in LabVIEW, writing an array into the registers or receiving one. For the MFCs and the Baratrons, MKS provided sample solutions containing conversion factors to calculate the flows and pressures from the raw count values. For the valves, a linear combination of unsigned integers (1, 2, 4, 8, ...) for each valve are fed as values. Following this, if a value of 12 (4+8) is fed as value, valves 3 and 4 are opened. For the thermocouples, two registers with the MSB (most significant bit) and LSB (least significant bit) halves starting at 11000 are needed for each thermocouple, needing to be combined to deliver correct temperature values.

Another thing that needed to be considered was the calibration of the MFCs with nitrogen, needing conversion factors (listed in Table 11 for gases used in this work) if using gases other than nitrogen.

Table 11: Gas correction factors (GCF) for the used gases.

Gas	GCF
Nitrogen	1.00
Helium	1.45
Methane	0.72
Ethane	0.50
Carbon Dioxide	0.70
Hydrogen	1.01

The desired process flows for each gas needed to be divided by the factors to deliver correct flows. This was realised by a calculator tab to avoid misuse by entering flows which are too high to process for the MFCs, leading to wrong gas mixtures. This calculator is shown in a screenshot of the program in Fig. 23(②), where a corrected setpoint for a flow of 20 sccm carbon dioxide is calculated. The other functions as shown in Fig. 23 are described below the figure.

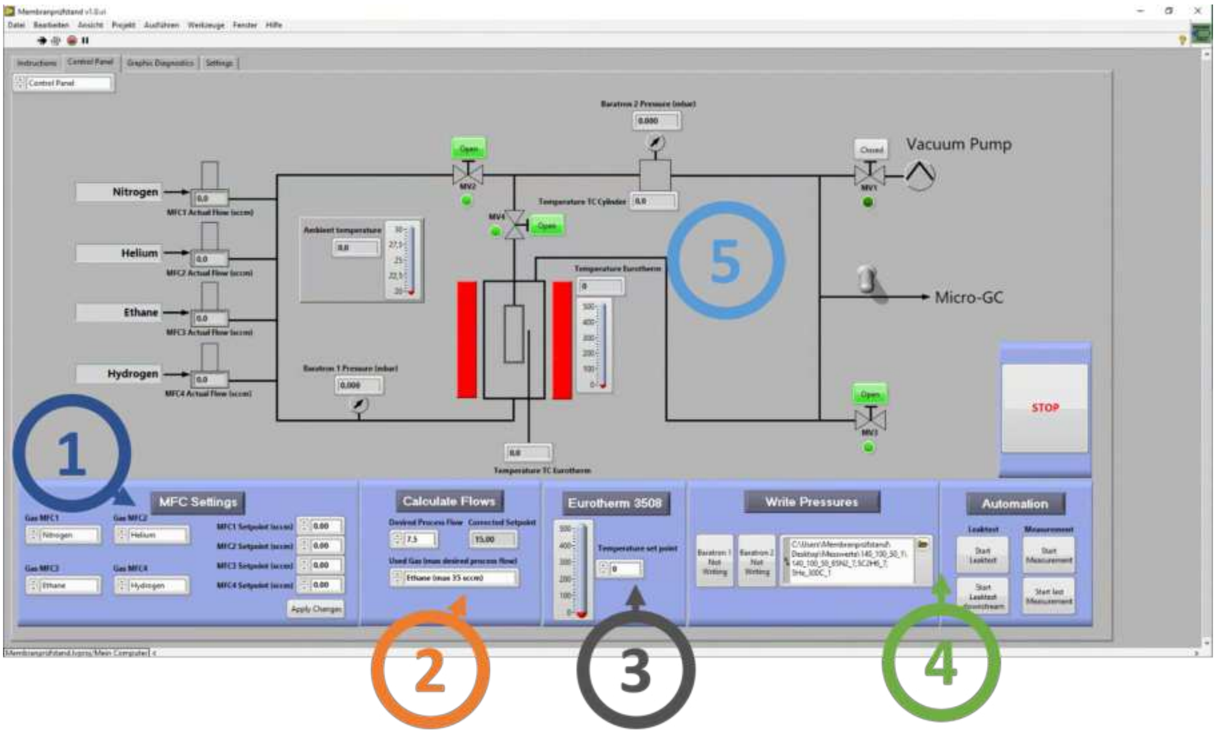

MFC1 Actual Flow (sccm): 0.0
MFC2 Actual Flow (sccm): 0.0
MFC3 Actual Flow (sccm): 0.0
MFC4 Actual Flow (sccm): 0.0
Ambient temperature: 0,0
Baratron 1 Pressure (mbar): 0,000
Baratron 2 Pressure (mbar): 0,000
Temperature TC Cylinder: 0,0
Temperature Eurotherm: 0
Temperature TC Eurotherm: 0,0
Gas MFC1: Nitrogen
Gas MFC2: Helium
Gas MFC3: Ethane
Gas MFC4: Hydrogen
MFC1 Setpoint (sccm): 0.00
MFC2 Setpoint (sccm): 0.00
MFC3 Setpoint (sccm): 0.00
MFC4 Setpoint (sccm): 0.00
Desired Process Flow: 7.5
Corrected Setpoint: 15.00
Used Gas (max desired process flow): Ethane (max 35 sccm)
Temperature set point: 0
C:\Users\Membranprüfstand\Desktop\Messwerte\140_100_50_1\140_100_50_65N2_7.5C2H6_7.5He_300C_1
Membranprüfstand.lvproj/Mein Computer

Figure 23: Screenshot of the LabVIEW user interface.

① Input field for MFC settings: The gases and flows fed through the MFCs are entered here and confirmed below the setpoints, allowing a seamless transition between different gas mixtures.

② Flow calculator as described above.

③ Temperature input for the furnace: If the program is stopped, the temperature input will automatically change to 0 to prevent the furnace to continue heating in case of failure. The heating rate is defined by the energy output of the furnace and can not be changed to avoid too high rates, which can destroy the quartz glass tube.

④ Logging functions further described in chapter 4.5.5.

⑤ Diagnostics and control system to check all flows, temperatures and valves over the course of the experiment.

4.5 Implementation of the test rig

4.5.1 Leak checking the test rig

After completing the assembly of the test rig, it had to be leak checked, as permeation experiments require a high level of leak-tightness. This is especially true for experiments performed with gas mixtures as feed gas, as even small levels of leaked gas can alter the results from the gas chromatograph.

To check that, a routine which is easy to reproduce had to be implemented. As seen in ④ in Fig. 23, the option 'Start Leaktest' can be found in the 'Automation' section of the program. After evacuating the test rig, clicking this button closes the valve leading to the vacuum pump, and automatically logs the pressure curve caused by leakage in the whole test rig. After clicking 'Stop Leaktest' on the same button, the leaktest stops, and the data can be analysed. If only the downstream area needs to be checked, which should be done before and after each measurement, 'Start Leaktest Downstream' should be clicked. An exemplary leak test performed following this routine is shown in Fig. 24.

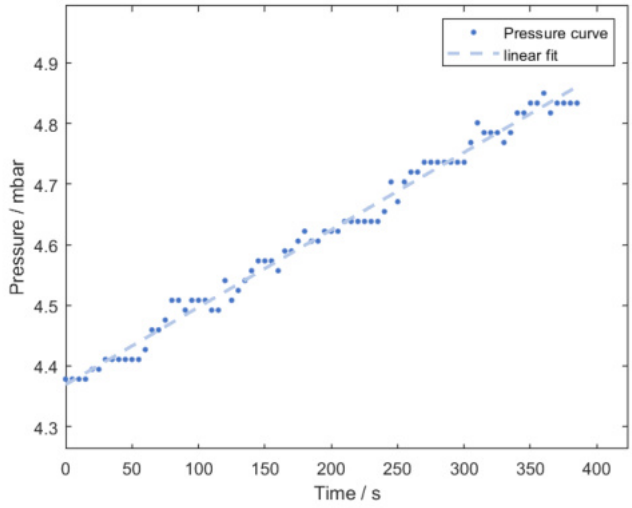

Figure 24: Examplary leaktest of the whole test rig.

The leakage of the test rig as measured in Fig. 24 is equivalent to a pressure rise of 0.0013 mbar/s, which is barely acceptable for the experiments performed. Only leak checking the downstream volume however leads to much lower leakage, equivalent to a pressure rise of under 0.00026 mbar/s. The downstream area has also been externally checked with a helium leak detector, confirming the leak rate to be in range of the internal leak rate of the used fittings. Therefore, a leak rate equivalent to a pressure rise below 0.0005 mbar/s in the downstream area is seen as acceptable to not alter the results greatly by leakage, and has to be determined before every experiment to check and to ensure consistent experiment conditions in the test rig.

4.5.2 Calibration of the gas chromatograph

The calibration of the Micro GC Fusion gas chromatograph was done internally by feeding gas mixtures into the system and measuring them as well as with an external calibration gas done during the initial setup of the GC system. The composition of this calibration gas is shown in Table 12. The internal calibration was done by evacuating and filling the system three times with the calibration mixture. Here, the gas mixtures were fed with a total flow of 100 sccm. After filling the system, the gas exhaust valve was opened and six measurements were started. The first three measurements were not included for the calibration, as they were used for purging the columns of the gas chromatograph.

In Table 13, parameters of the calibrations for all gases relevant to the system are listed. The calibration graphs are shown in the appendix. The range is here the range of concentrations (in Vol%), in which the calibration was performed. For flammable gases, the upper limit had to be below 15 Vol% due to safety reasons. Oxygen was only calibrated with the external calibration gas as well as with laboratory air to be able to quantify the effects of possible leaks.

Table 12: Composition of the external calibration gas.

Gas	Vol%
N_2	81.5
O_2	1
CO_2	1
C_2H_6	0.1

Table 13: Calibrations for the gases relevant to the system.

Y=k·X	k	R^2	Range
He	9896.1	1.0000	0-65 %
N_2	1458.5	0.9997	0-98 %
O_2	1725.5	0.9999	0-21 %
H_2	16579	1.0000	0-8 %
CH_4	3560.6	1.0000	0-15 %
CO_2	103409	0.9994	0-40 %
C_2H_6	118322	1.0000	0-15 %

4.5.3 Sealing of the membranes with graphite ferrules

Sealing of the prepared samples was performed in accordance with the procedure proposed by Fernandez et al.,[25] however slight adjustments were made to fit the sample membranes. At first, the graphite ferrules (Ohio Valley Specialty Co., 10 mm 100 % Graphite Ferrules) had to be conditioned with a 316 Stainless steel tube with an outside diameter of 10 mm. For that, the dummy tube was fitted to the connectors and tightened with a maximum torque of 12 Nm. Afterwards the dummy tube was removed from the connectors, leaving a smooth surface on the inside of the ferrules. In succession, the sample membranes were fitted to the connectors and carefully tightened with a maximum torque of 8 Nm. A schematic representation of the sample sealing is shown in Fig. 25.

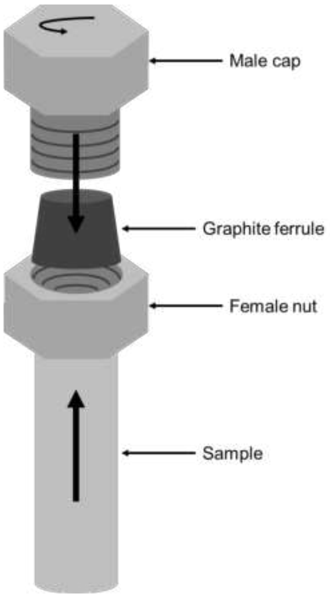

Figure 25: Schematic representation of the sample sealing.

To check the quality of the sealing with graphite ferrules, the connected dummy tube was tested for leakage in the test rig. For that, leak tests were performed for the downstream area including the graphite sealed dummy tube. The resulting pressure curve of this leak test is shown in Fig. 26. The resulting pressure rise was determined as 0.00026 mbar/s as mean value of three experiments, which is in line with the pressure rises of the downstream area without the sample sealing.

The main disadvantage of the method is, as stated in Fernandez et al.,[25] that a big amount of the membrane area is lost because of the connection, as seen in Fig. 27. Therefore a minimum length of 50 mm is needed for the sample tubes to have sufficient membrane area.

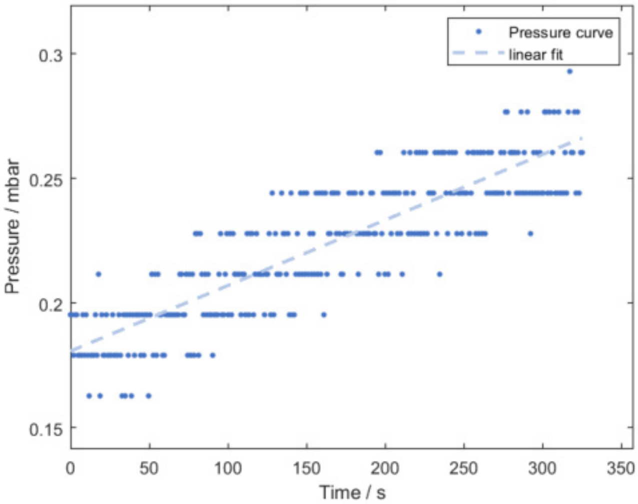

Figure 26: Pressure curve of the leak test of the downstream area including the graphite sealed dummy tube.

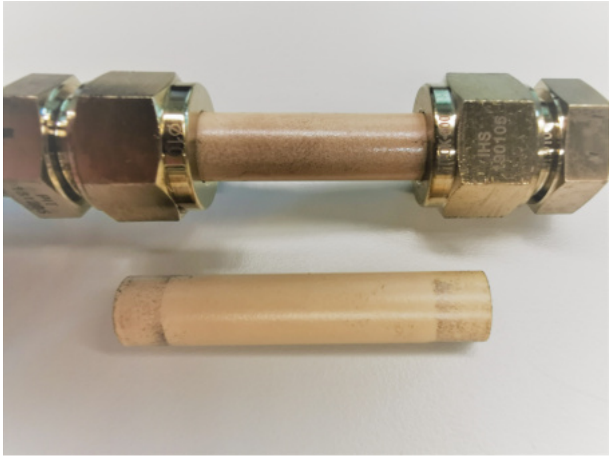

Figure 27: Image of the membrane area lost because of the connection.

4.5.4 Calculation of the downstream volume

To calculate the permeances of the sample membranes, the downstream volume of the test rig was determined (see (2) on page 10). For that, the volumes of all used parts were calculated (if not specified) and added. In table 14, these volumes are shown as calculated by the inside diameter and length, assuming cylindrical shapes for all parts. The values printed in blue are as specified by the manufacturer, the values in orange were measured by a calliper for smaller parts and a measuring tape for larger parts.

Table 14: Calculated downstream volumes.

Part	Tubes	Cylinder	Elastic tube	3-way valve	Solenoid valve
I.D. in mm	4		10.6	10	3.175
l in mm	1600		250	15	25
V in mm^3	20106	1000000	22062	1178	198
Part	Vacuum valve	Particle filter	Quick coupling	Female tees	Union cross
I.D. in mm	15	19.1	10	5	4.8
l in mm	50	75.2	58.4	119.2	23.2
V in mm^3	8836	21546	4587	2340	420
Total V in mm^3		**1081273**	**Total V in mL**		**1081.273**

4.5.5 Development of a method to measure the theoretical selectivities of membranes-Single gas testing

To calculate the theoretical selectivities of membranes, the ratio of the permeances of single gases are calculated as in (8).

$$n_{th}(X/Y) = \frac{P(X)}{P(Y)} \tag{8}$$

Thus, a method for consistently measuring the permeances of single gases had to be established as follows:

1. Before conducting an experiment, a leak test was performed to determine the pressure rise caused by leakage (see (2) on page 10). After that, the system was evacuated and heated to 300 °C for one hour while evacuating. This was done to degas the membrane. The system stayed evacuated until it was filled with the sample gas.

2. To guarantee a pure atmosphere, the system was evacuated and held at the minimum for 5 minutes and filled with the sample gas with the highest achievable flow. This was done twice to ensure a pure atmosphere. After the final filling step, the gas exhaust valve was opened.

3. After closing the valve connecting the feed and downstream area directly, the downstream area was evacuated again, leaving the valve leading to the membrane opened.

4. After reaching a constant pressure, the vacuum valve was closed and the pressure values in the downstream area were logged until reaching a pressure of 5 mbar. After that, the vacuum valve was opened again. This measurement was conducted three times.

5. The experiments were performed at room temperature, 100 °C, 150 °C, 200 °C, 250 °C, 300 °C, 350 °C and 400 °C. The gases used for single gas measurement were nitrogen, helium and carbon dioxide. Single gas measurements of flammable gases such as methane, ethane and hydrogen were not performed due to safety reasons.

6. After conducting experiments at all temperatures, another leak test was performed to ensure that the system had not changed over the course of the experiment.

The pressure rises used for determining the mass flux (see (2) on page 10) were calculated by linear approximation of the resulting pressure curves. The resulting selectivities (see (8) and section 2.5) were then plotted against the temperature. In Fig. 28, a typical selectivity-temperature plot is displayed.

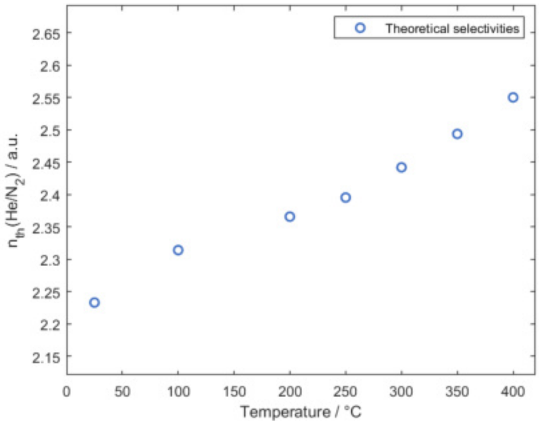

Figure 28: Example of a typical selectivity-temperature plot.

4.5.6 Development of a method to measure the real selectivities of membranes for gas mixtures-Multi gas testing

To calculate the real selectivities of membranes, the ratio of the percentages of gases in mixtures compared to their feed values have to be calculated as in (9).

$$n_{real}(X/Y) = \frac{X_{perm}(V/V)/X_{feed}(V/V)}{Y_{perm}(V/V)/Y_{feed}(V/V)} \tag{9}$$

Thus, a time-saving method for consistently measuring the compositions of feed and permeate of gas mixtures had to be established as follows.

1. Before conducting an experiment, a leak test was performed to check if any new leaks have appeared. After that, the membrane was degased as described in section 4.5.5.
2. To guarantee a pure atmosphere, the system was evacuated and held at the minimum for 5 minutes twice and filled with the sample gas mixture with a total feed flow rate of 100 sccm. After the final filling step, the gas exhaust valve was opened.
3. After closing the valve connecting the feed and downstream area directly, the downstream area was evacuated again, leaving the valve leading to the membrane opened.
4. After reaching a constant pressure, the vacuum valve was closed and the pressure values in the downstream area were logged until reaching a pressure of 5 mbar. After that, the vacuum valve was opened again. This measurement is also conducted three times. The permeances of gas mixtures are calculated the same way as the single gas permeances for the sake of completeness and to compare them with the single gas permeance values.
5. After the third experiment, the vacuum valve stayed closed until the permeate pressure reached 100 mbar. After that, the downstream area was filled with nitrogen until a total pressure of 1000 mbar was reached. The reason for that is, that the Inficon Micro GC Fusion operates at ambient pressure. Filling the downstream area with only permeate is not possible, as the permeation process is too slow.
6. As soon as the pressure reached 1000 mbar, twelve GC measurements were started. The first six measurements however were not included for the results, as the system needs some

time to generate stable values after the addition of a new gas.

7. Experiments were performed at room temperature, 100 °C, 200 °C and 300 °C. The gas mixtures used for the experiments are shown in Table 15.

8. After conducting experiments at all temperatures, another leak test was performed to ensure that the system had not changed over the course of the experiment.

9. If flammable gases were used for the experiments, the system had to be filled with an inert atmosphere afterwards.

Table 15: Gas mixtures used for permeation experiments in this work.

Gas mixture	Vol% N_2	Vol% CH_4	Vol% C_2H_6	Vol% He	Vol% H_2
1	85	0	7.5	7.5	0
2	85	0	7.5	0	7.5
3	85	7.5	0	0	7.5

Limitations of the method

The method described above delivers reliable selectivities in a reasonable amount of time, however there are some limitations and sources of error, which cannot be fully avoided:

- The resolution of module A is not high enough to separate hydrogen and helium reliably, thus making it impossible to measure the selectivities for these two gases together. In Fig. 29, an example of this overlap is shown.

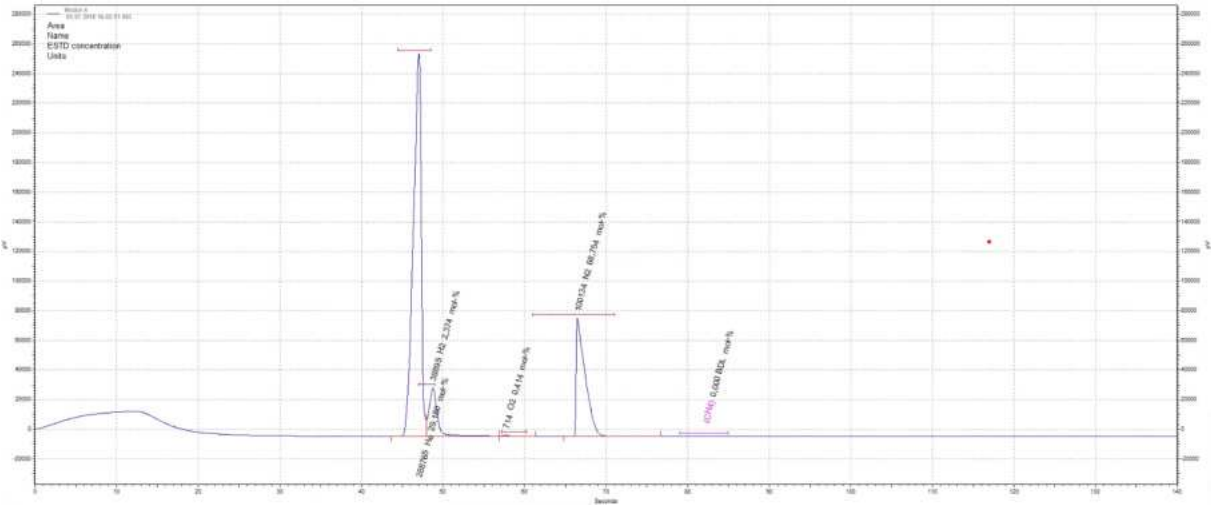

Figure 29: Overlap of the He and H_2 peaks in the gas chromatogram.

- As nitrogen is used for the filling of the downstream area to reach the pressure necessary, it cannot be included for selectivity measurements.
- Whenever the gas chromatograph takes samples, it reduces the pressure of the downstream area, thus adding to the error of the method, as the pressure difference from the ideal operating pressure increases with every measurement.
- Although the filling of the downstream area with nitrogen is a convenient time-saving way of setting the pressure necessary to conduct measurements, it adds to the systematic error of the method. To estimate this error, the method was simulated by feeding a mixture of 90 Vol% He and 10 Vol% CH_4 (X(He/CH_4=9). For this mixture, two experiments were performed, where the downstream area was filled with feed gas until a pressure of 1000 mbar was reached in one. The other experiment was performed to simulate the method used, as the downstream area was filled with feed gas until a pressure of 100 mbar was reached and subsequently filled with nitrogen until a pressure of 1000 mbar was reached.

  In Fig. 30, the results of this experiments are shown. In the right diagram, which shows the results of the experiment performed as in the method described above, it is clearly visible that in the first six measurements, the Micro GC Fusion does not generate stable results; however, after that, the results nearly stay the same. This is also apparent when comparing the results of the two experiments, as the mean value for the last six measurements and for the feed gas as shown in Table 16 are nearly the same. In this table, the nominal deviation σ_{nom} is the deviation from the nominal value, which is the mean value of the feed gas and is calculated as in (10). The minimum error for each dataset is approximated by the coefficient of variation (CV) and is calculated as in (11).

  The minimum total error caused by the Micro GC Fusion is estimated as the sum of errors of the method and the deviation of the nominal value from the set point, which is 9 for the measured gas mixture (X(He/CH_4=9), resulting in an error of 1.56 %. The minimum total error, recieved by adding the minimum error of the method and the minimum error of the GC, equates to 2.66 %.

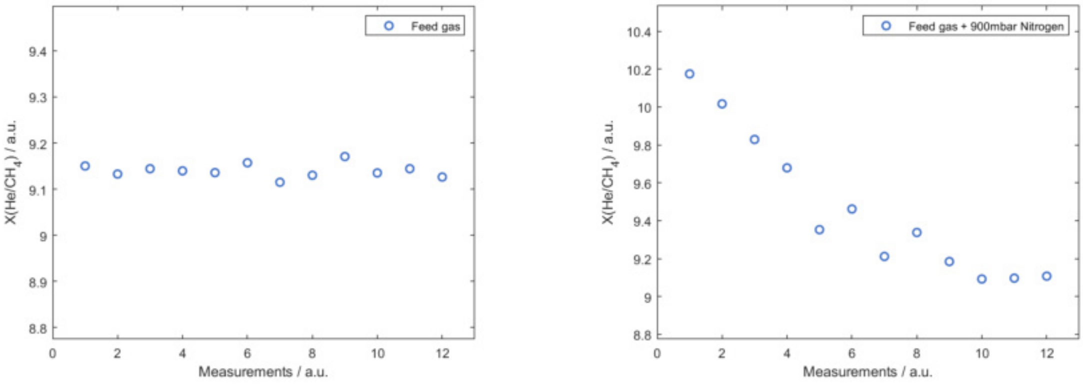

(a) Measuring feed gas (b) Measuring feed gas filled with nitrogen

Figure 30: Effect on the results of filling the feed gas with nitrogen.

$$\sigma_{nom} = \sqrt{\frac{\sum_{i=0}^{n-1}(n_i - n_{nom})^2}{n-1}} \tag{10}$$

$$CV = \frac{\sigma_{nom}}{\bar{n}} \tag{11}$$

Table 16: Estimating the minimum error of the method.

	Filled (1-12)	Filled (7-12)	Feed gas
$\bar{n}$	9.46	9.17	9.14
σ_{nom}	0.255	0.101	0.0147
CV (in %)	2.69	1.11	0.161

5 Results and discussion

5.1 Characterisation of the substrate tubes

All data necessary for the geometrical calculations of the substrate density are shown in Table 17 (the values specified are the mean values of the two rings). The results of the mercury porosimetry is shown in Fig. 31. In this graph, the relative pore volume for each segment is displayed as a bar graph with bars in the median value of each pore range, whereas the cumulative pore volume is shown as function of the pore size. The secondary electron microscopy pictures of the surface and the cross section are shown in Fig. 32.

Table 17: Data for the calculation of the porosity

L (in mm)	4.20
V (in mm^3)	211
m (in g)	0.585
ρ(sample) (in g/cm^3)	2.77
ρ(Al_2O_3) (in g/cm^3)	3.95[6]
$\bar{p}$ (in%)	29.9

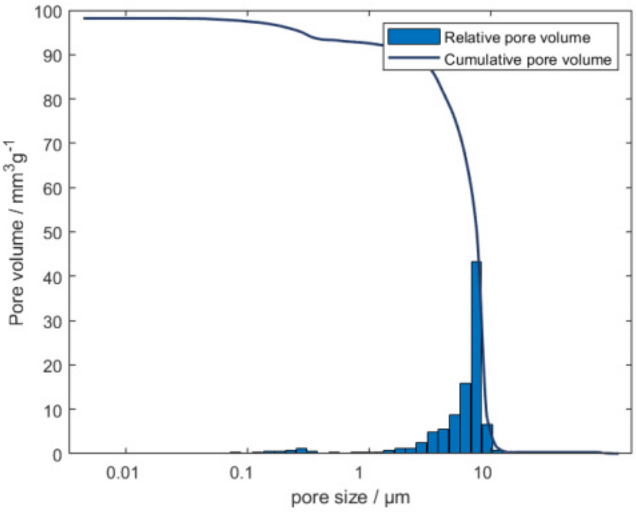

Figure 31: Results of the mercury porosimetry of the alumina supports.

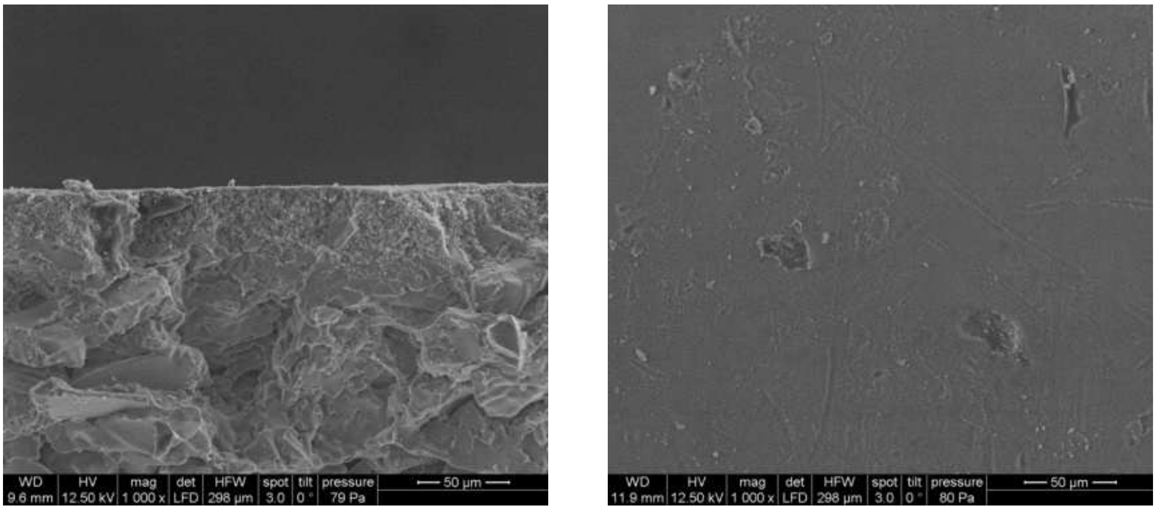

(a) Cross section

(b) Surface

Figure 32: SEM pictures of the substrate tube.

Looking at the surface of the sample, it is covered by a dense looking top layer with minor visible defects, but no apparent cracks.

Combining the results of the SEM images and the mercury porosimetry, two sectors in the sample can be confirmed: a macroporous bulk in the single digit micrometer range, and a macroporous layer in the range of 0.20-0.38 micrometers. However, the proclaimed pore size of the top layer is 0.05 micrometers.

As a small relative pore value caused by another mesoporous layer is nearly invisible in the mercury porosimetry due to the large macroporous bulk, a larger magnification for the cross section (Fig. 33) was looked at. Here, evidence for a denser third layer can be observed, which should match the small relative pore volume peak of $0.2\,\mathrm{mm}^3/\mathrm{g}$ in the pore diameter range of 0.059-0.048 µm, which matches the proclaimed pore size.

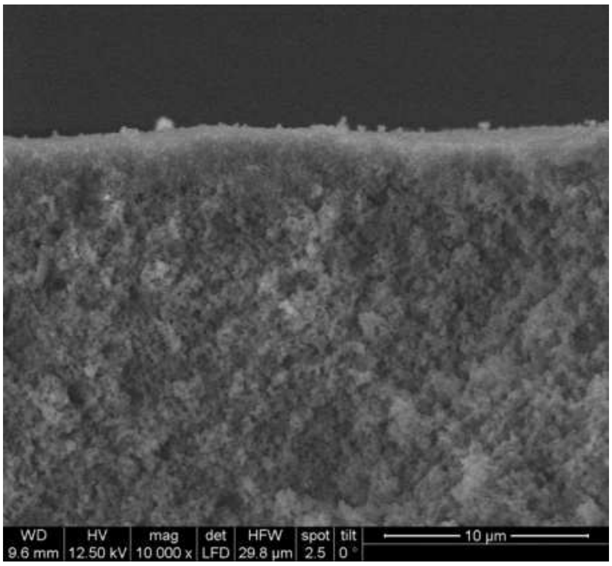

Figure 33: SEM pictures of the cross section of the substrate tube showing the top layer.

5.2 Preparation of microporous ceramic membrane layers

To compare the different samples, the same magnifications have to be chosen for all samples. Pictures were therefore taken with magnifications of 20000x[1], 10000x[2], 5000x[2] and 500x[2]. Only the images with the magnifications of 10000x (for the cross section) and 5000x (for the surface) are included in the main part of this work as they provide the most information, all other magnifications (if not specified otherwise for individual samples) are included in the appendix. The samples are numbered as shown in tables 7 and 8.

---

[1] only for the cross section

[2] for the cross section and the surface

Single coatings

In figures 34-38, SEM pictures of single coated substrate tubes are shown.

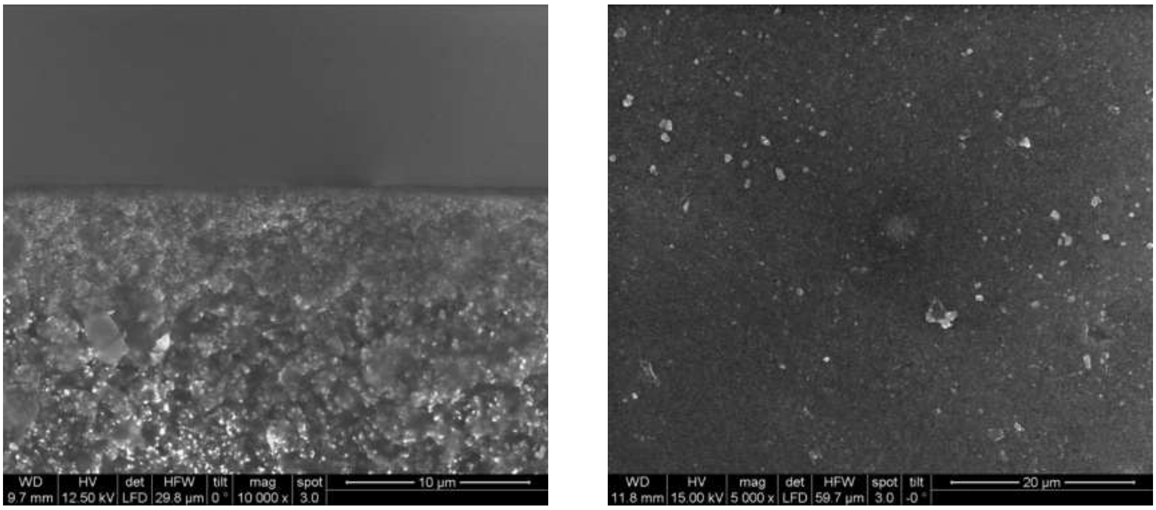

(a) Cross section (b) Surface

Figure 34: Sample 1 coated at a withdrawal speed of 20 mm/min.

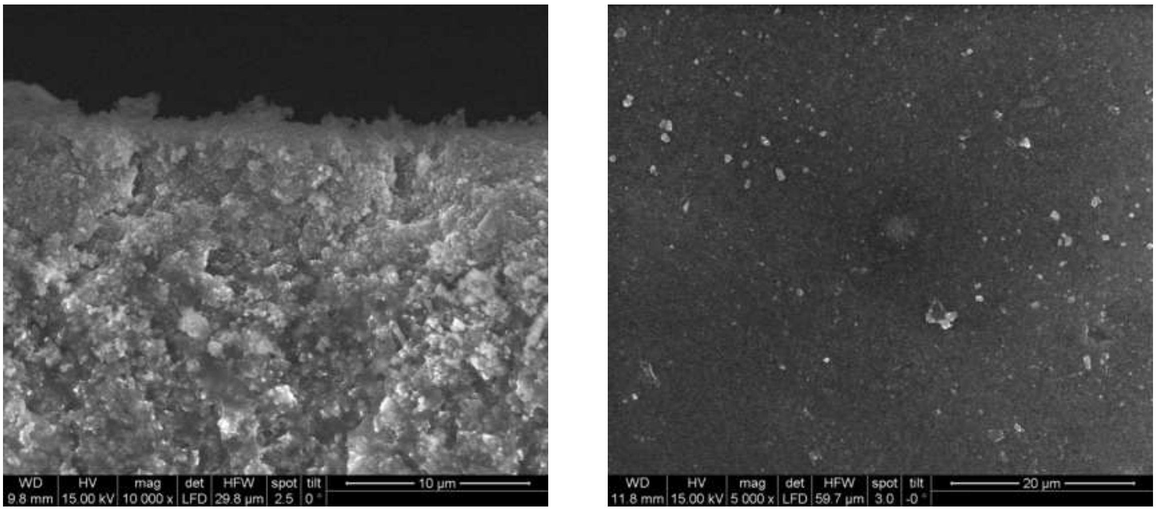

(a) Cross section (b) Surface

Figure 35: Sample 2 coated at a withdrawal speed of 50 mm/min.

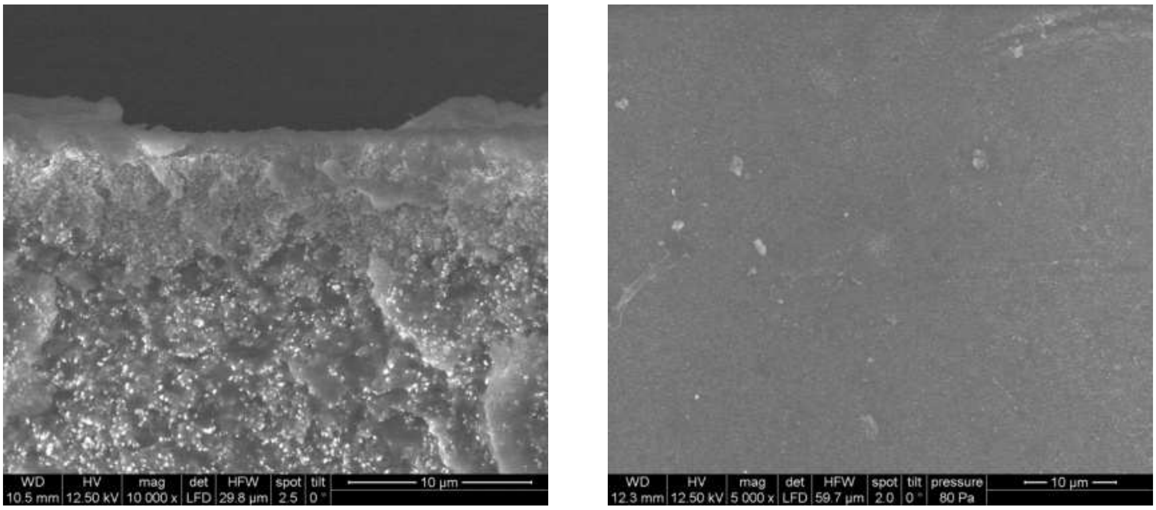

(a) Cross section (b) Surface

Figure 36: Sample 3 coated at a withdrawal speed of 140 mm/min.

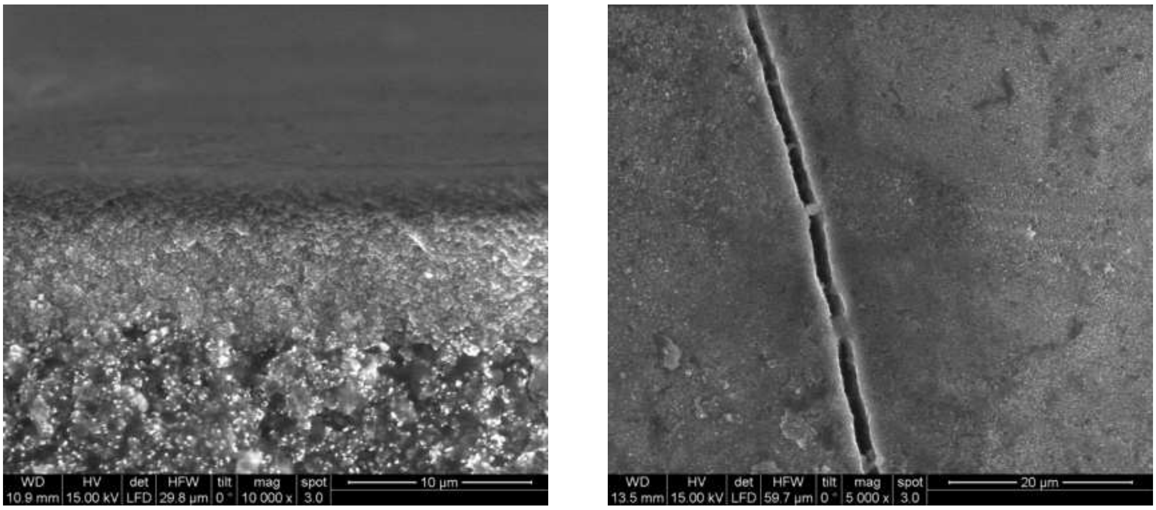

(a) Cross section (b) Surface

Figure 37: Sample 4 coated at a withdrawal speed of 300 mm/min.

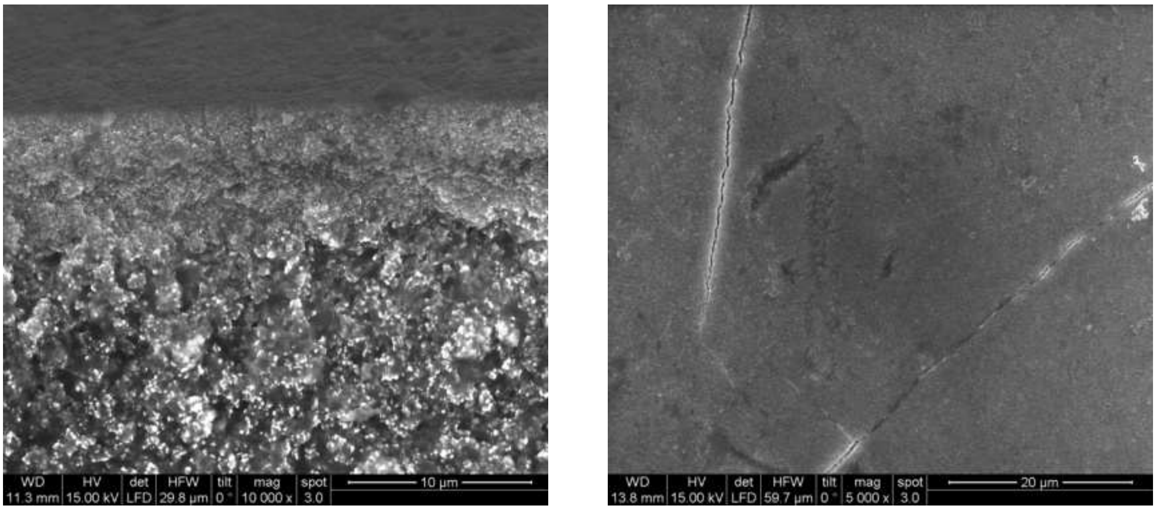

(a) Cross section

(b) Surface

Figure 38: Sample 5 coated with cooled polysilazane at a withdrawal speed of 300 mm/min.

During the observation of the sample surfaces, the emphasis was laid on observing the defects, as any cracks in the surface are problematic for the permeability of membranes. Such cracks were observed with the samples coated with a withdrawal speed of 300 mm/min (Fig. 37 and 38), although cooling the polysilazane led to smaller cracks.

For the observation of the cross sections, the emphasis was laid on the observation of possible dense amorphous layers. No such layers could be observed after coating the samples once. What could be observed, however, is an infiltration of the substrate with polysilazane, visible by the build-up of electrostatic charges through the intermediate layer of the substrate. In the case of the samples coated with a withdrawal speed of 300 mm/min, too much infiltrated polysilazane led to the formation of these cracks.

The next move was performing double coating experiments, with the first coating step infiltrating the layer to an extent where the pores were small enough to inhibit further infiltration. For that, the focus was laid on a withdrawal speed of 140 mm/min, as it was the fastest speed reliably achievable (as faster withdrawal speeds lead to thicker theoretical layers as shown in (1)) where no cracks were observed on the sample surface.

Double coatings

In Fig. 39-42, SEM pictures of the double coated substrate tubes are shown. For all samples, a withdrawal speed of 140 mm/min during the first coating step was used.

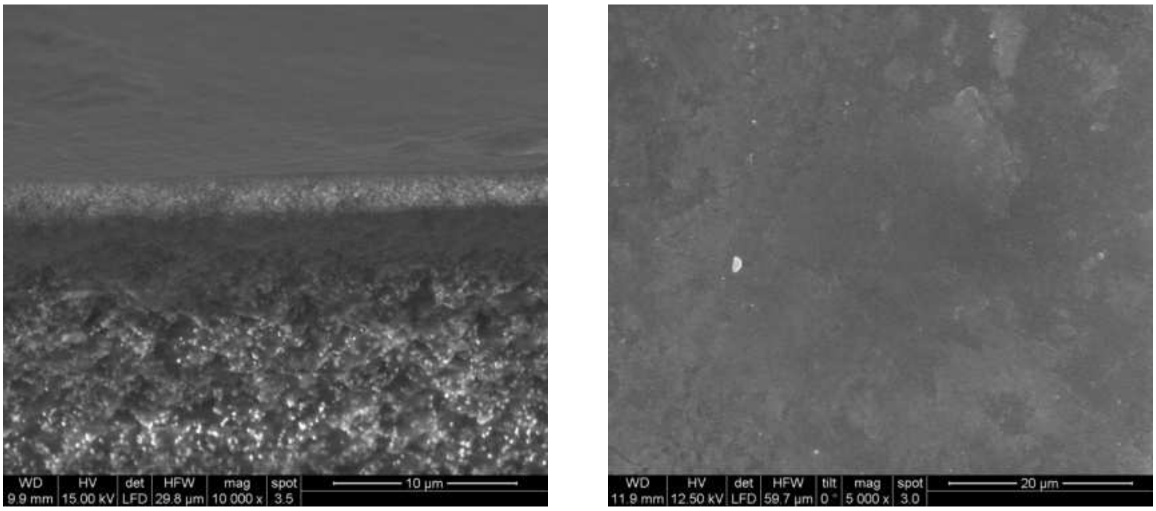

(a) Cross section (b) Surface

Figure 39: Sample 3 after the second coating step at a withdrawal speed of 50 mm/min (Step 1: 140 mm/min).

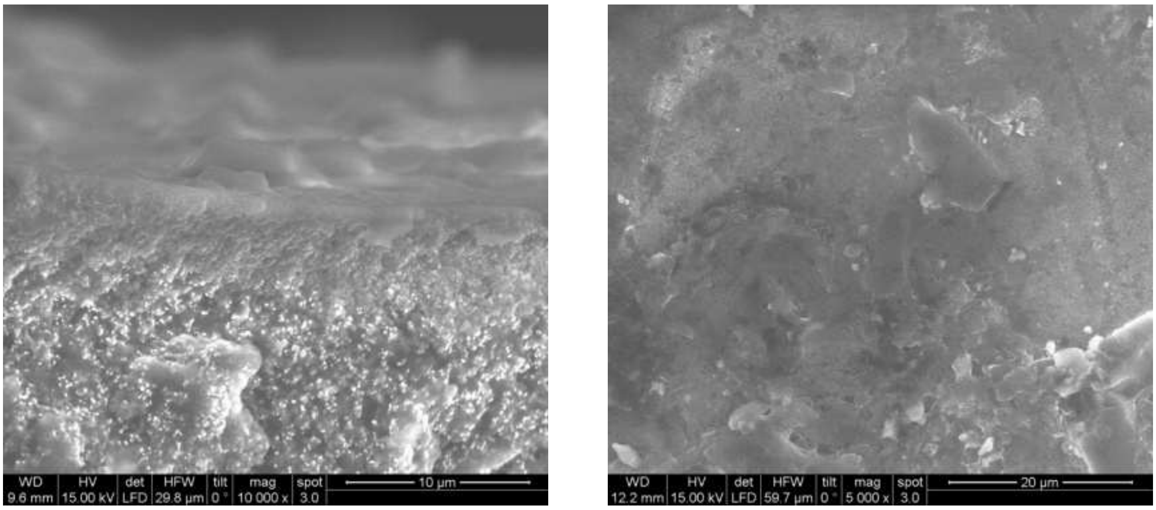

(a) Cross section (b) Surface

Figure 40: Sample 6 after the second coating step at a withdrawal speed of 100 mm/min (Step 1: 140 mm/min).

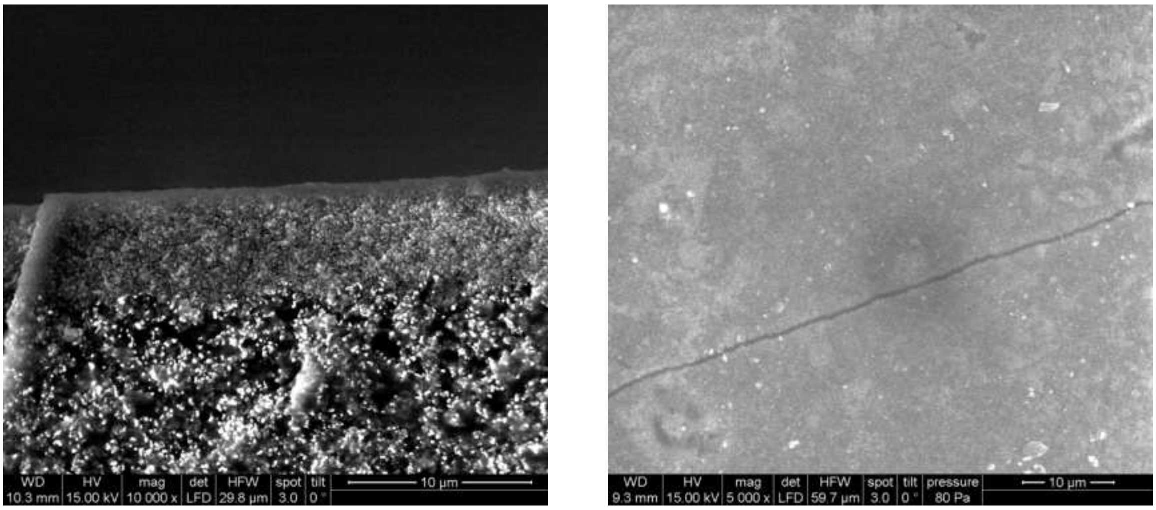

(a) Cross section (b) Surface

Figure 41: Sample 7 after the second coating step at a withdrawal speed of 120 mm/min (Step 1: 140 mm/min).

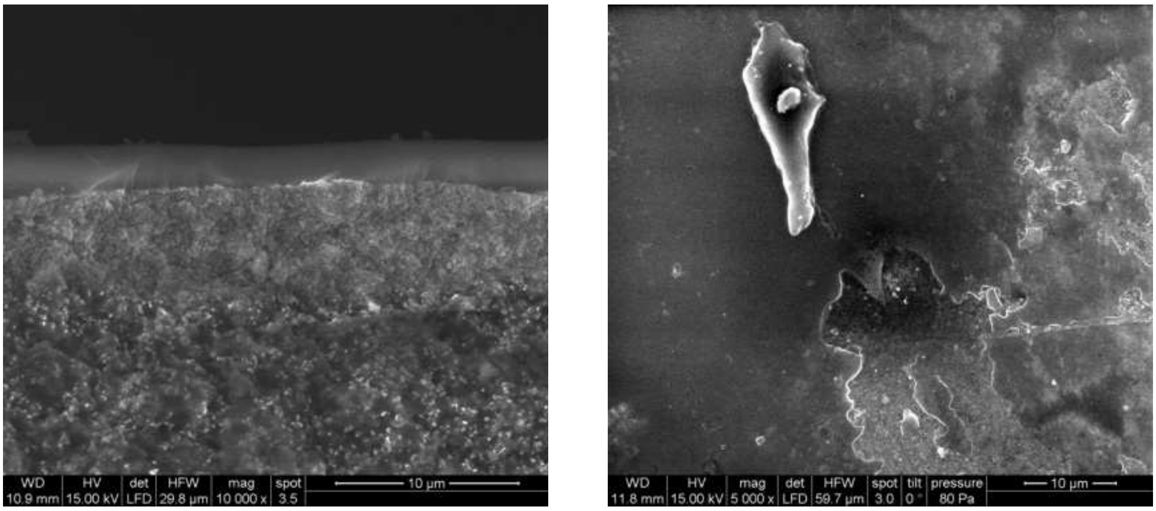

(a) Cross section (b) Surface

Figure 42: Sample 8 after the second coating step at a withdrawal speed of 140 mm/min (Step 1: 140 mm/min).

In contrast to the samples only once, a separation layer could be observed for two samples, the sample coated with 120 mm/min in the second step (sample 7, Fig. 41) and the sample coated with 140 mm/min in the second step (sample 8, Fig. 42). For those samples, layer thicknesses of 0.5 µm (sample 7) and 3 µm (sample 8) were observed. However, these samples both show defects. Sample 7 showed small cracks, whereas sample 8 showed cracks and areas, where there seemed to be no separation layer. However, these areas were limited to a very small total area of the sample.

For the other two samples, no such separation layer could be observed. However, there were no visible defects on the surface.

Next, three approaches were pursued in order to improve the quality of the separation layers:

- During pyrolysis, the crosslinked polymer decomposes, and pores remain. Therefore, the crosslinked layer should be denser than the pyrolysed layer, and applying a layer directly onto a crosslinked layer should limit further infiltration by the liquid polymer, which should result in a higher quality separation layer. To check that hypothesis, two layers with the same withdrawal speeds as in sample 7 and sample 8 were prepared by directly coating the second layer onto the crosslinked first layer.
- Coat another layer onto those samples where no separation layer could be observed. This was done for sample 7 and 8 with a third coating at a withdrawal speed of 50 mm/min as well as for another sample the layer of which was prepared at the same withdrawal speeds as sample 6, but the third coating step was performed at a withdrawal speed of 140 mm/min.
- Coat another layer onto those samples where a separation layer could be observed to fill the cracks. This was only done for sample 7, as previous work in the research group had shown that if the layer thickness exceeds 3 µm, the critical layer thickness is reached for the system used. The third coating step was performed at a withdrawal speed of 50 mm/min.

Direct coating onto a crosslinked layer

In Fig. 43-44, SEM pictures of the layers prepared by directly coating onto crosslinked layers are shown. For sample 10, a different magnification was chosen as the resulting cracks were too big.

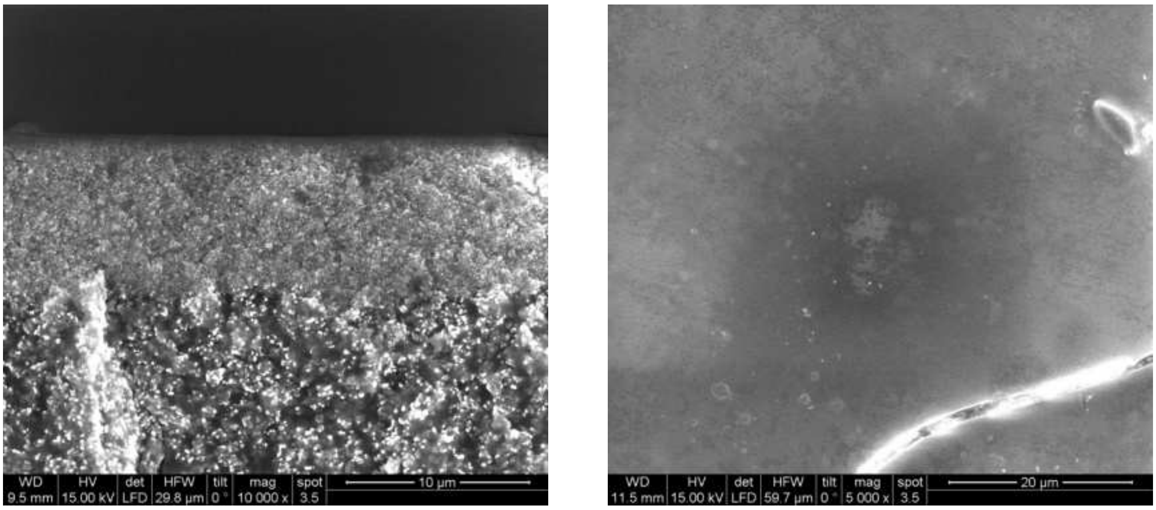

(a) Cross section (b) Surface

Figure 43: Sample 9 after the second coating step at a withdrawal speed of 120 mm/min (Step 1: 140 mm/min).

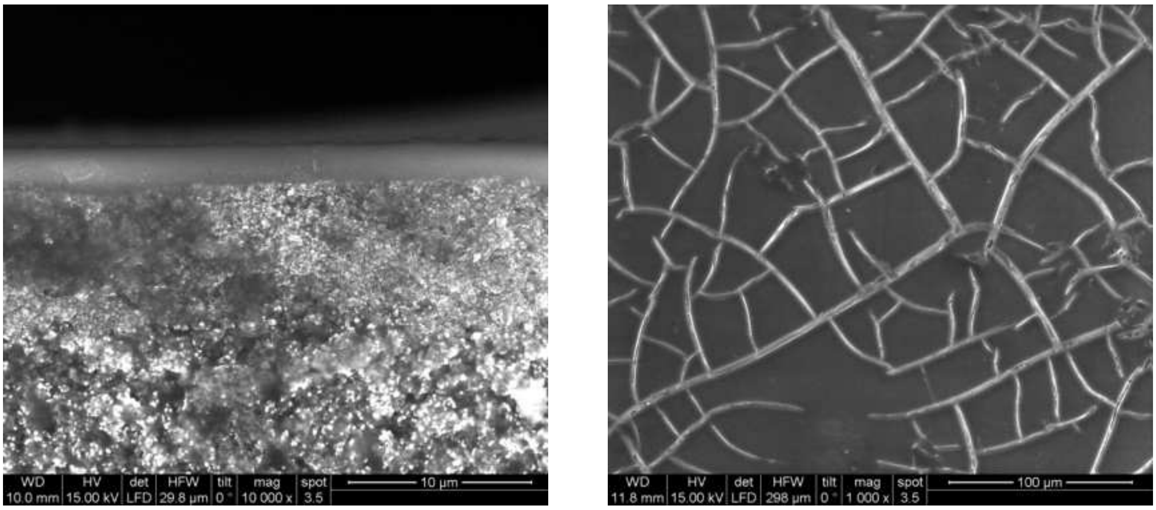

(a) Cross section (b) Surface

Figure 44: Sample 10 after the second coating step at a withdrawal speed of 140 mm/min (Step 1: 140 mm/min).

As clearly visible in the images, the layers prepared by directly coating onto crosslinked layers show the same thicknesses as the layers prepared by coating onto pyrolysed layers when working with the same withdrawal speeds. However, there are more and bigger cracks, especially with sample 10. Apparently the opposite of the desired effect took place, as even more of the polymer infiltrated the pores, forming a network of large cracks over the whole surface.

Triple coatings

In Fig. 45-46, SEM pictures of the triple coated samples are shown. For sample 7, which showed a thin layer and small cracks after the second coating, no picture is shown, as the sample delaminated during the pyrolysis.

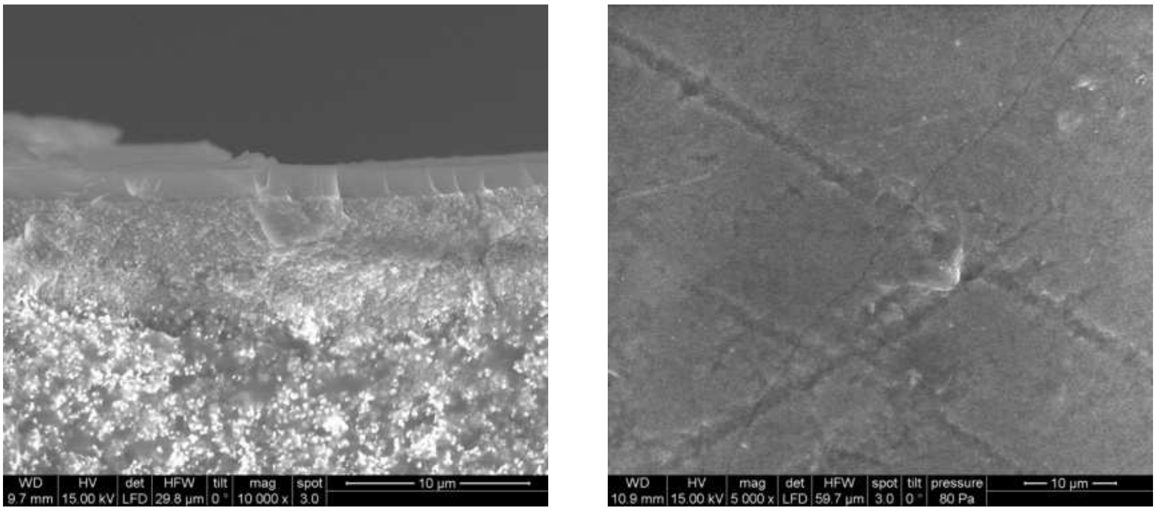

(a) Cross section (10000x)

(b) Surface (5000x)

Figure 45: Sample 6 after the third coating step at a withdrawal speed of 50 mm/min (Step 1: 140 mm/min, Step 2: 100 mm/min).

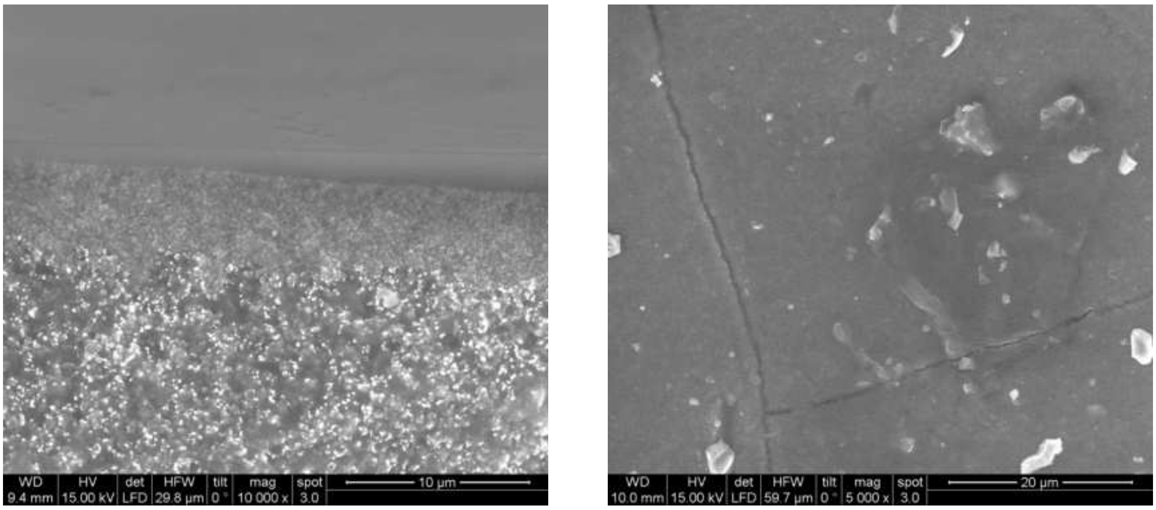

(a) Cross section (10000x)

(b) Surface (5000x)

Figure 46: Sample 11 after the third coating step at a withdrawal speed of 140 mm/min (Step 1: 140 mm/min, Step 2: 100 mm/min).

As visible in the images, separation layers were formed in both experiments, however also cracks are visible. For those samples, layer thicknesses of 2 µm (sample 6, Fig. 45) and 1.5-3.5 µm (sample 11, Fig. 46) were observed. For sample 11, the layer thickness could not be determined explicitly as no even layer could be prepared.

Summary of the coating experiments

After concluding the coating experiments of test samples, a few trends could be observed:

- As the infiltration of the intermediate layer plays such a big role in the first coating steps, the Landau-Levich model cannot be applied for these coatings to predict layer thicknesses. Therefore only models based on empirical findings could be used for estimating layer properties. Even then, the high variance of layer properties obtained by using these models suggest a very complex system.
- The biggest obstacle in preparing membrane layers is to prevent cracks in the intermediate or separation layers.
- A few procedures seem to be unsuitable to obtain crack free layers, such as the use of excessive withdrawal speeds during the first coating step, as well as the direct coating onto a crosslinked layer.

- The most promising procedure is coating the sample multiple times while decreasing the withdrawal speed for each consecutive step.

In Table 18, all samples where separation layers could be achieved, are listed together with their layer thickness and crack width. There was no sample for which a crack free separation layer could be obtained.

Table 18: Summary of samples for which separation layers could be obtained.

Sample no.	Coatings	Layer thickness (in µm)	Crack width (in µm)
6	3	2	0.1
7	2	0.5	0.4
8	2	3	1.5
9	2	0.5	1.2
10	2	3	5.2
11	3	1.5-3.5	0.6

As already seen in fig.43-44, samples 9 and 10, where the second layer was directly coated onto a crosslinked layer, show very high crack widths larger than their layer thickness. For sample 7, the crack width is in the same range as the layer thickness. However, for samples 6, 8 and 11, the crack width is lower than the layer thickness, making it possible that the cracks are not going through the whole separation layer.

Therefore, the coating procedure carried out to obtain these samples 6 and 8 were chosen for testing of separation characteristics in the membrane test rig. The layer of sample 11 was deemed too uneven to be measured in the test rig. Additionally, a sample without a visible separation layer was measured in the test rig to show the impact of a separation layer on the selectivity. The coating procedures of the measured samples are once again shown in Table 19, along with their equivalent samples used for evaluation of layer characteristics.

Table 19: Summary of samples, where separation layers could be obtained.

Sample no.	1. coating	2. coating	3. coating	Equivalent to sample
1p	140 mm/min	140 mm/min		8 (two coatings)
2p	140 mm/min	100 mm/min	50 mm/min	6 (three coatings)
3p	140 mm/min	100 mm/min		6 (two coatings)

5.3 Preparation of membranes for the measurement in the test rig

In Fig. 47, a picture of the samples after gas separation testing is shown. Sample 1p is darker colored than the other two samples, which can be explained by slight impurities in the oven atmosphere during pyrolysis. These impurities, however, do not lead to a significant difference in the layer quality, which is why the membrane was also used for testing.

The SEM pictures of the membrane layers are shown in Fig. 48-50. For sample 2p and sample 3p, magnifications of 10000x are shown, as the cracks are only barely visible in a magnification of 5000x. The crack widths and separation layer thicknesses (as in chapter 5.2, measured digitally) for each sample measured in the test rig are shown in Table 20.

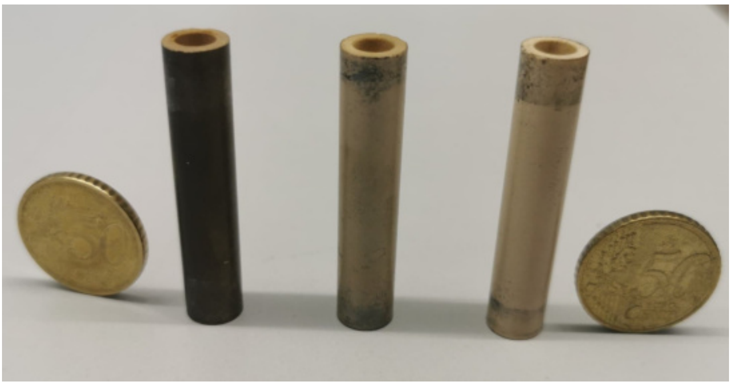

,

Figure 47: Picture of the samples (1p: left, 2p: middle, 3p: right) after measuring.

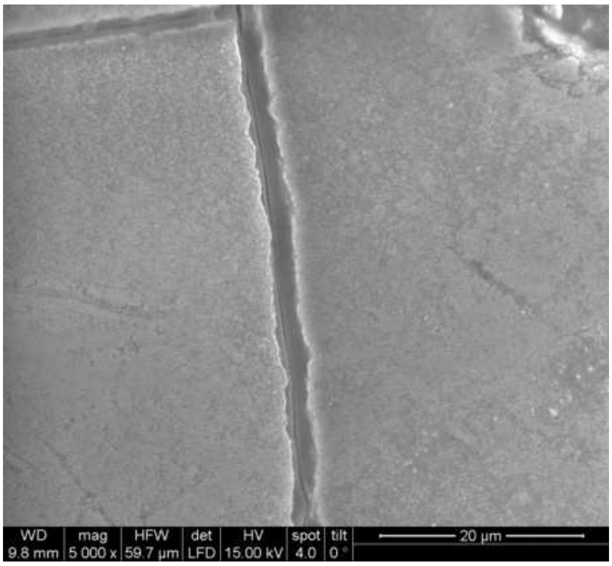

Figure 48: Sample 1p after gas separation testing.

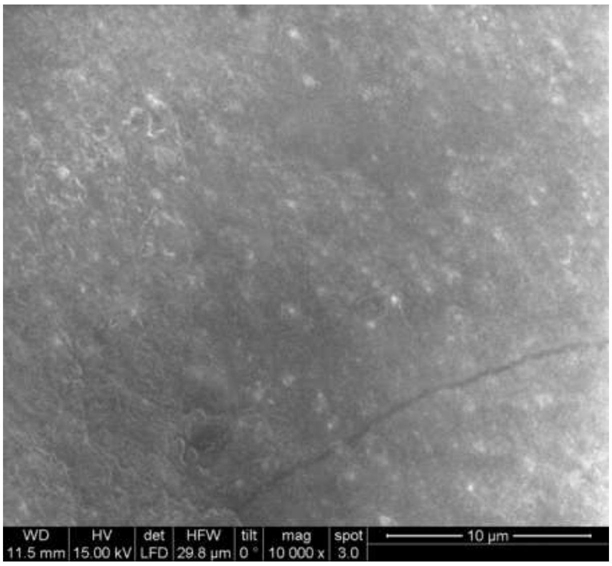

Figure 49: Sample 2p after gas separation testing.

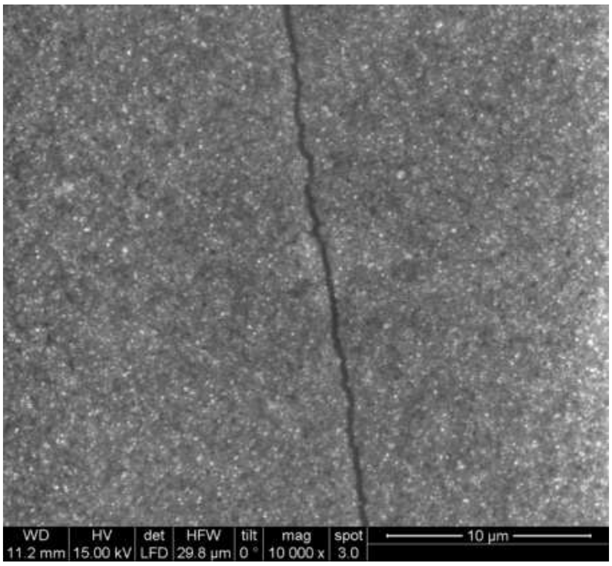

Figure 50: Sample 3p after gas separation testing.

Table 20: Layer thicknesses as in chapter 5.2 and crack widths of the measured membranes.

Sample no.	layer thickness	crack width
1p	3 µm	2.3 µm
2p	2 µm	0.1 µm
3p	0 µm	0.2 µm

One thing that immediately stands out while looking at the crack widths in Table 20 is that they are not consistent with the crack widths seen in chapter 5.2. For sample 1p, cracks 50 % bigger than the ones in the test sample can be observed. For sample 2p, the cracks are only half the size than the ones in the test samples. For sample 3p, cracks could be observed on the membrane surface, which could not be found on the test samples. These results show the high variance of layer properties for layers prepared.

5.4 Permeance properties of the prepared membranes

For sample 1p, only single gas measurements using nitrogen, carbon dioxide, and helium were conducted. For samples 2p and 3p, single gas measurements and gas mixture measurements with gas mixtures as described in Table 15 on page 35 were conducted. For all samples, the tested length excluding the membrane sealing was kept at 30±1 mm.

The permeance measurement of an uncoated sample specimen with N_2 as test gas resulted in very high permeance values, which were too high to be measured in the linear range of the pressure rise curve. The experiment at room temperature showed pressure rises larger than 70 mbar/s resulting in a permeance larger than $3.8 \cdot 10^{-4}\,\mathrm{mol\,s^{-1}Pa^{-1}m^{-2}}$ (compared to permeances smaller than $1 \cdot 10^{-6}\,\mathrm{mol\,s^{-1}Pa^{-1}m^{-2}}$ for the coated samples). Thus, no further tests at higher temperatures or with other gases were performed.

5.4.1 Single-gas permeance properties

Sample 1p

In Table 21 and Fig. 51-52, the results of the single gas permeance measurements of sample 1p are shown. All permeances are shown in $10^{-6}\,\mathrm{mol\,s^{-1}Pa^{-1}m^{-2}}$.

Table 21: Results of the single gas measurements for sample 1p, as well as calculated Knudsen selectivities.

T (in °C)	P(He)	P(CO_2)	P(N_2)	n_{th}(He/CO_2)	n_{th}(He/N_2)
28	1.76	1.07	0.95	1.64	1.85
100	1.61	0.82	0.83	1.96	1.93
150	1.54	0.73	0.78	2.12	1.99
200	1.50	0.67	0.74	2.25	2.04
250	1.47	0.63	0.71	2.35	2.07
300	1.44	0.61	0.70	2.37	2.07
350	1.44	0.62	0.73	2.30	1.96
400	1.46	0.68	0.79	2.16	1.84
			Knudsen	3.3	2.6

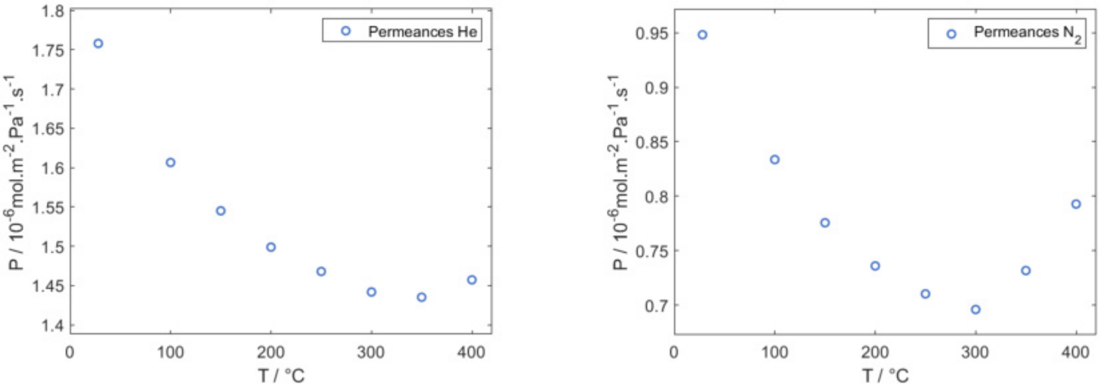

(a) Helium (b) Nitrogen

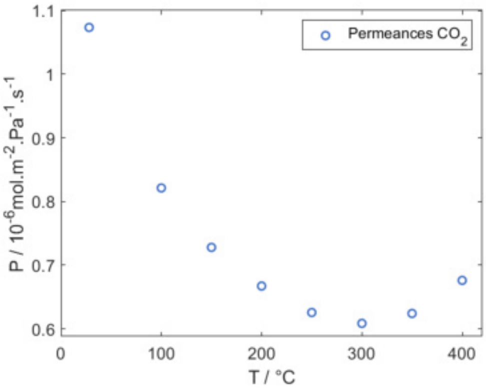

(c) Carbon dioxide

Figure 51: Permeance-temperature plots of sample 1p for He, N_2 and CO_2.

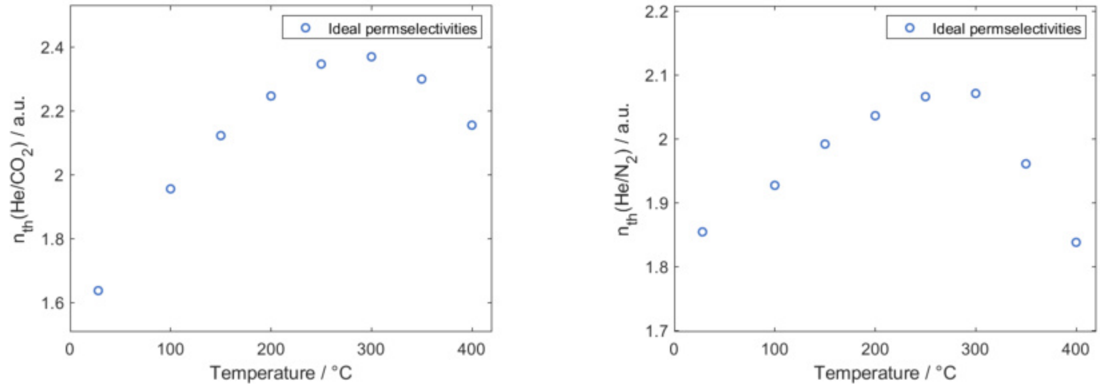

(a) He/CO_2 (b) He/N_2

Figure 52: Ideal permselectivity-temperature plots for theoretical selectivities of sample 1p.

As visible in the results of single gas permeance tests of sample 1p, the aforementioned cracks on the surface of sample 1p (as seen in Fig. 48 on page 51) have a big effect on the selectivity of the membrane. This can be postulated, as the selectivity is well below the theoretical Knudsen selectivity for both He/N_2 and He/CO_2. This suggests cracks going through the whole mesoporous layer, leading to non-Knudsen gas transport through the membrane. However, a trend of a slight increase of selectivity with higher temperatures can be observed, leading to the conclusion that microporous regions in the separation layer lead to this behaviour. This can be said, as Knudsen selectivity only depends on the ratio of the square roots of the molar masses of the gases (as shown in Table 4), and not on the temperature.

However, this fact can not be used to explain the decrease of permeances and selectivities at temperatures higher than 300 °C. A possible explanation for this behaviour is that gas molecules are adsorbed in the pore structures at lower temperatures, thus blocking some pores, leading to smaller permeabilities. At higher temperatures, these gas molecules desorb, opening the pores again, leading to higher permeabilities. This, however, could not be prevented, as degassing the membrane at 300 °C after each measured temperature would increase the time needed for each experiment exorbitantly. Another possible explanation for the aforementioned behaviour is that the graphite sealing deteriorates at higher temperatures; however Prasad described in his Ph.D. thesis[26] that graphite ferrule sealing should be stable up to temperatures of 450 °C.

As the results for this sample, caused by excessively large cracks, were not expected to change for gas mixtures, no experiments with gas mixtures were performed for sample 1p.

Sample 2p

In Table 22 and Fig. 53-54, the results of the single gas permeance measurements of sample 2p are shown. All permeances are shown in $10^{-6}\,\mathrm{mol\,s^{-1}Pa^{-1}m^{-2}}$.

Table 22: Results of the single gas measurements for sample 2p, as well as calculated Knudsen selectivities.

T (in °C)	P(He)	P(CO_2)	P(N_2)	n_{th}(He/CO_2)	n_{th}(He/N_2)
28	0.68	0.39	0.27	1.73	2.47
100	0.65	0.28	0.23	2.32	2.79
150	0.65	0.24	0.22	2.69	2.99
200	0.65	0.22	0.20	2.96	3.16
250	0.65	0.20	0.20	3.20	3.29
300	0.65	0.19	0.19	3.38	3.40
350	0.65	0.18	0.19	3.54	3.49
400	0.66	0.18	0.19	3.68	3.51
			Knudsen	3.30	2.60

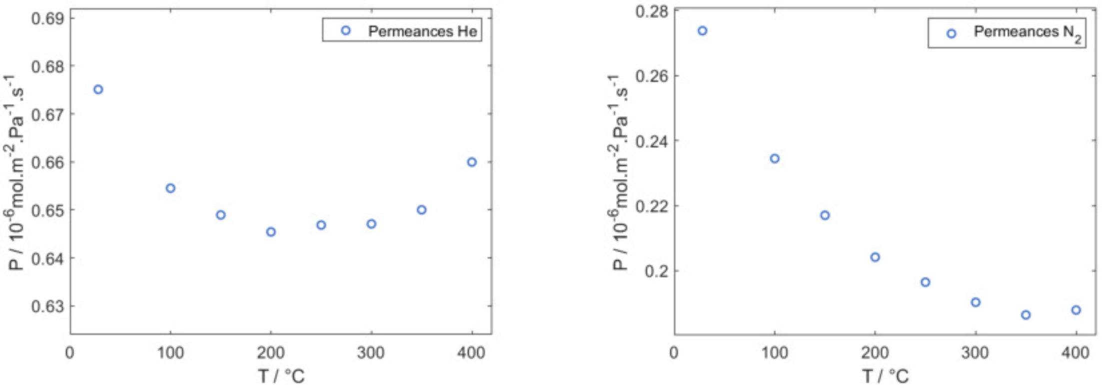

(a) Helium (b) Nitrogen

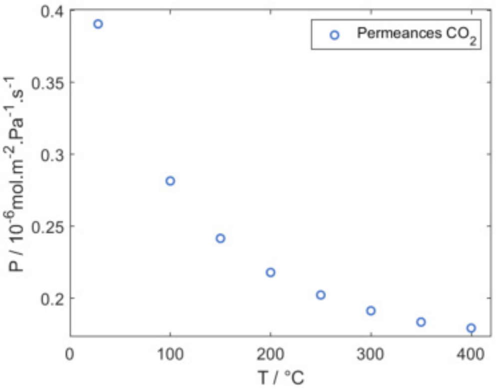

(c) Carbon dioxide

Figure 53: Permeance-temperature plots of sample 2p for He, N_2 and CO_2.

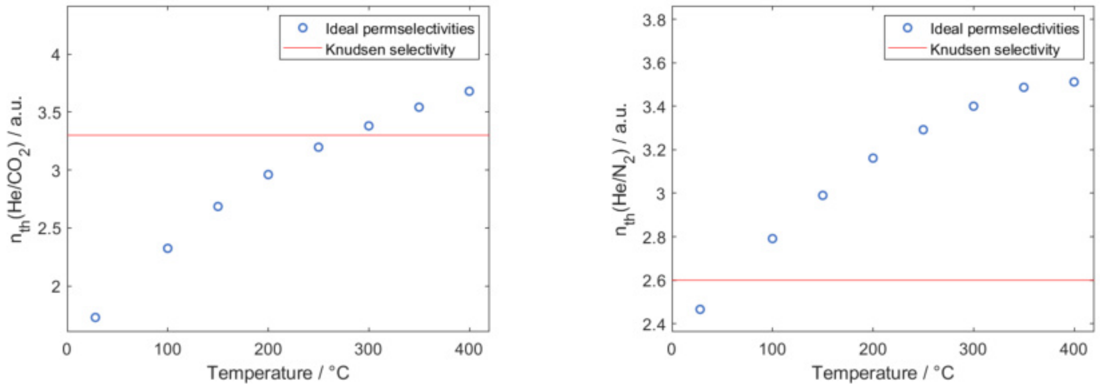

(a) He/CO_2 (b) He/N_2

Figure 54: Selectivity-temperature plots for theoretical selectivities of sample 2p.

As visible in the results of single gas permeance tests of sample 2p, even with very low crack widths, non-Knudsen gas transport through the membrane is limiting the selectivity of the membrane, albeit to a much lower extent compared to sample 1p. For both He/N_2 and He/CO_2, the theoretical Knudsen selectivities are exceeded at increased temperatures, indicating molecular sieving behaviour for parts of the membrane. Another hint pointing towards molecular sieving behaviour is the fact that, just like for sample 1p, the selectivities increase with higher temperatures. The lower crack width leads to a higher increase in selectivities. However, this comes at the cost of the permeances being approximately only a third of those measured for sample 1p. For sample 2p, an increase of permeances at higher temperatures could also be observed, though only for helium and nitrogen. For helium, this has to be put in relation with the fact that the permeance of helium only varies 5 % in the observed temperature range. This is also another hint pointing towards molecular sieving behaviour, as helium is too small to be held back by the pores in the system, whereas nitrogen and carbon dioxide are large enough to see their permeance reduced at higher temperature. Nonetheless, the increase of permeances at higher temperatures remains a problem.

Sample 3p

In Table 23 and Fig. 55-56, the results of the single gas permeance measurements of sample 3p are shown. All permeances are shown in $10^{-6}\,\mathrm{mol\,s^{-1}Pa^{-1}m^{-2}}$.

Table 23: Results of the single gas measurements for sample 3p, as well as calculated Knudsen selectivities.

T (in °C)	P(He)	P(CO_2)	P(N_2)	n_{th}(He/CO_2)	n_{th}(He/N_2)
28	1.19	0.82	0.54	1.46	2.21
100	1.11	0.56	0.46	1.99	2.44
150	1.08	0.46	0.42	2.32	2.58
200	1.05	0.41	0.39	2.57	2.68
250	1.03	0.37	0.37	2.78	2.78
300	1.02	0.35	0.36	2.96	2.82
350	1.02	0.33	0.35	3.08	2.92
400	1.02	0.32	0.35	3.19	2.91
			Knudsen	3.30	2.60

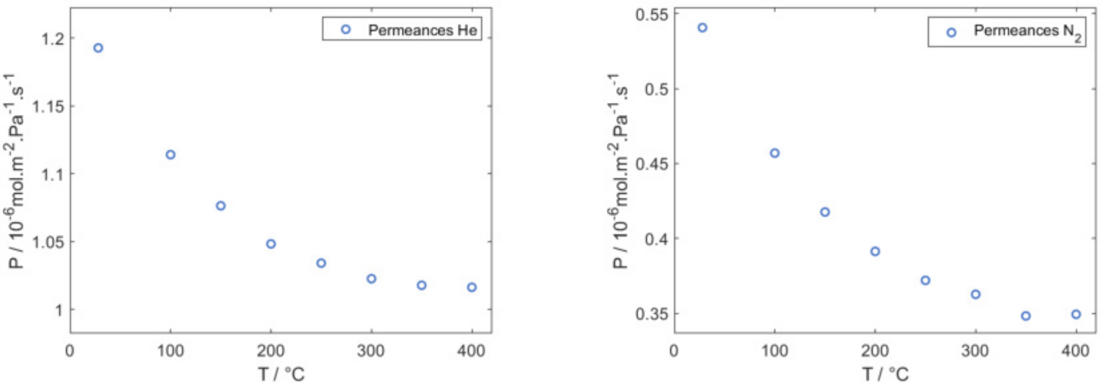

(a) Helium (b) Nitrogen

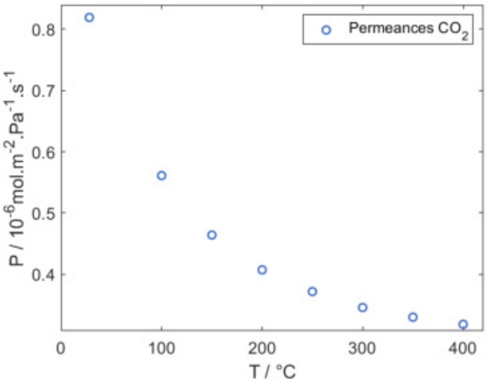

(c) Carbon dioxide

Figure 55: Permeance-temperature plots of sample 3p for He, N_2 and CO_2.

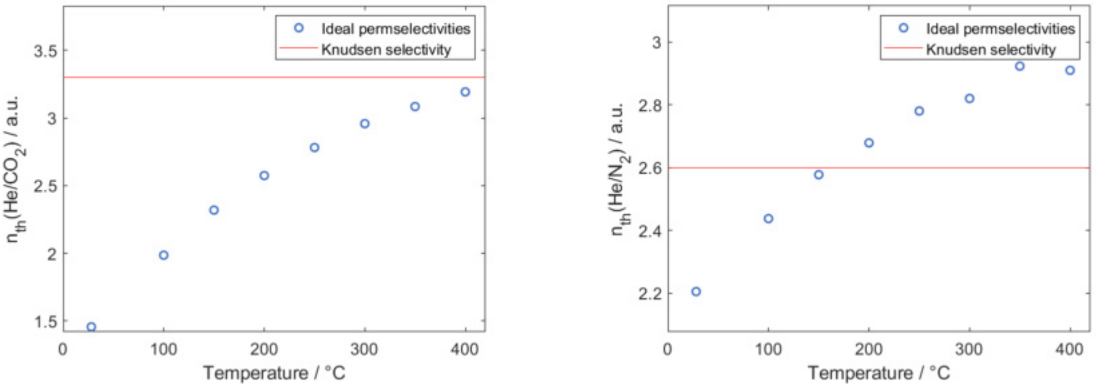

(a) He/CO_2 (b) He/N_2

Figure 56: Selectivity-temperature plots for theoretical selectivities of sample 3p.

As visible in the results of single gas permeance tests of sample 3p, although no separation layer is visible in the SEM image, there seems to be molecular sieving behaviour for the membrane layer. This leads to the conclusion that the infiltrated intermediate layer also takes part in the gas separation process. Although the He/CO_2 selectivity of sample 3p doubled comparing ambient temperature and 400 °C, Knudsen selectivity could not be reached, indicating larger defects in the sample. Comparing the results of theoretical selectivity measurements for samples 2p and 3p, it is apparent that applying an additional layer onto the membrane further increases the theoretical selectivities by approximately 0.25 (at ambient temperature) and 0.5 (at 400 °C). This serves as further proof for the molecular sieving qualities of the separation layer, as a thicker separation layer (as in sample 2p) increases the temperature effect for the selectivity.

Also for sample 3p, an increase of permeance for nitrogen and helium could be observed at higher temperatures, leading to a slower selectivity increase at higher temperatures. A comparison of the selectivity-temperature plots for samples 2p and 3p (Fig. 57) shows that the curve shapes seem to be matching. The curves were fitted with parabolic functions, with the fit parameters listed in Table 24.

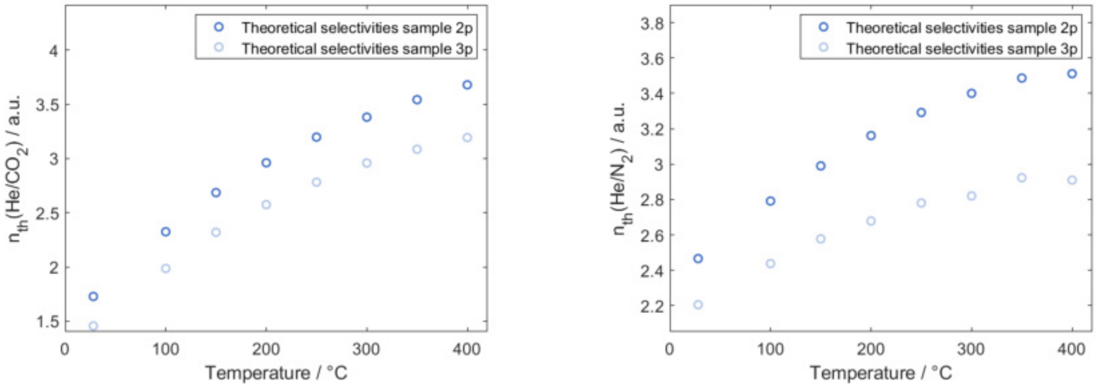

(a) He/CO_2 (b) He/N_2

Figure 57: Selectivity-temperature plots for theoretical selectivities of samples 2p and 3p.

Table 24: Parabolic fits of the selectivity-temperature plots for theoretical selectivities of samples 2p and 3p.

	He/CO_2		He/N_2	
n_{th}=-aT^2+bT+c	2p	3p	2p	3p
a	$9.53 \cdot 10^{-6}$	$9.09 \cdot 10^{-6}$	$6.04 \cdot 10^{-6}$	$4.28 \cdot 10^{-6}$
b	$9.24 \cdot 10^{-3}$	$8.51 \cdot 10^{-3}$	$5.43 \cdot 10^{-3}$	$3.75 \cdot 10^{-3}$
c	1.49	1.23	2.31	2.11
R^2	0.9994	0.9997	0.9997	0.9961

Looking at the fit data, a correlation of the selectivity plots can be suggested, as the polynomial coefficients for the fits are in the same order of magnitude and further seem to be dependent on the ordinate intercept c. However, the sample size and the results are not enough to definitively prove a connection. It can be assumed that the cause of the curve of the plot resides either in the graphite sealing, in a general trend of the selectivity of the chosen membrane, or in a systematic error of the method which is larger than the one estimated.

5.4.2 Permeance and selectivity measurements of gas mixtures

Sample 2p

In Tables 25-26 and Fig. 58-59, the results of the gas mixture experiments for sample 2p are shown. The numbering of the gas mixtures refers to Table 15 on page 35. All permeances are shown in $10^{-6}\,\mathrm{mol\,s^{-1}Pa^{-1}m^{-2}}$.

Table 25: Permeabilities of the gas mixtures for sample 2p.

T (in °C)	P(1)	P(2)	P(3)
27	0.31	0.27	0.31
100	0.27	0.25	0.26
200	0.23	0.21	0.23
300	0.22	0.20	0.20

Table 26: Real selectivities derived from the gas mixture experiments for sample 2p, as well as calculated Knudsen selectivities.

T (in °C)	$n_{real}(He/C_2H_6)$	$n_{real}(H_2/C_2H_6)$	$n_{real}(H_2/CH_4)$
27	2.12 ± 0.14	2.23 ± 0.29	2.36 ± 0.05
100	2.49 ± 0.19	2.55 ± 0.16	2.51 ± 0.09
200	2.91 ± 0.22	2.87 ± 0.23	2.74 ± 0.12
300	3.71 ± 0.09	3.36 ± 0.28	2.91 ± 0.01
Knudsen	2.7	3.9	2.8

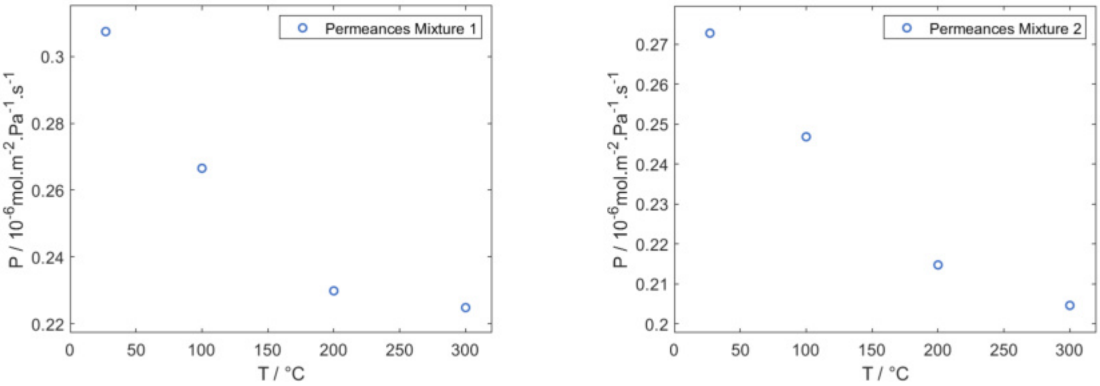

(a) Mixture 1 (85 % N_2, 7.5 % C_2H_6, 7.5% He)   (b) Mixture 2 (85 % N_2, 7.5 % C_2H_6, 7.5% H_2)

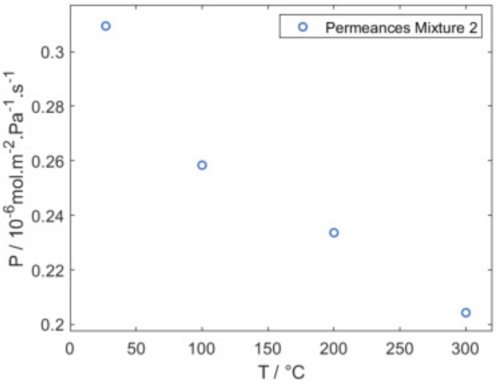

(c) Mixture 3 (85 % N_2, 7.5 % CH_4 7.5% H_2)

Figure 58: Permeance-temperature plots of sample 2p for the gas mixtures used.

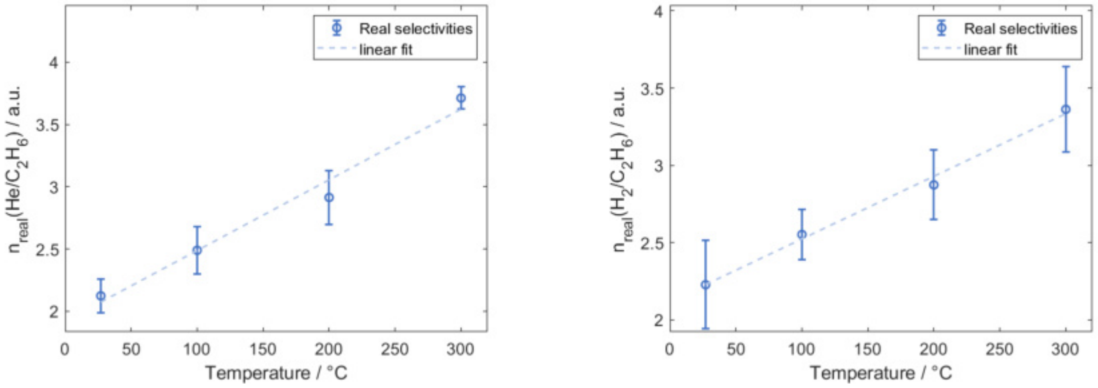

(a) He/C_2H_6 (b) H_2/C_2H_6

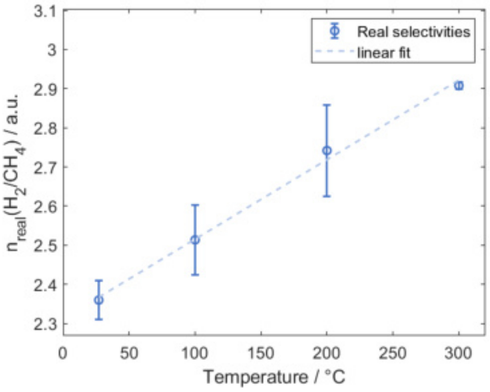

(c) H_2/CH_4

Figure 59: Selectivity-temperature plots derived by using the gas mixtures for sample 2p.

Looking at the permeance values first, it is apparent, that all curves are looking similar and are located around the same permeance values. This was expected, as nitrogen makes up 85 % of all three mixtures. The permeance values are slightly higher than those of pure nitrogen, which can be explained by the addition of hydrogen. Interaction between the gas molecules plays an important role in absolute permeance values, hence linear combination can not be used to estimate single gas permeance values for flammable gases.

Selectivity values only surpass the theoretical Knudsen values at temperatures higher than 200 °C for He/C_2H_6 and at temperatures higher than 300 °C for H_2/CH_4. The real selectivity increases with higher temperature could be fitted with linear functions, with fit parameters shown in Table 27.

Table 27: Linear fits of the selectivity-temperature plots for real selectivities of sample 2p.

n_{real}=aT+b	He/C_2H_6	H_2/C_2H_6	H_2/CH_4
a	$5.68 \cdot 10^{-3}$	$4.06 \cdot 10^{-3}$	$2.03 \cdot 10^{-3}$
b	1.92	2.12	2.31
R^2	0.9781	0.9934	0.9955

For all used gas mixtures, the resulting selectivity-temperature plots can be fitted linearly with R^2-values larger than 0.975. This leads to the conclusion that the flattening of the curve for all single gas measurements can be explained by differences in method execution for each single gas. One likely problem during single gas measurements could be the different heating speeds for different gases depending on the heat conductivity differences of the used gases. This will be further discussed in the summary of the permeance experiments.

Furthermore the He/C_2H_6 selectivity of sample 2p increases at a higher rate than the H_2/C_2H_6 selectivity. Assuming that the increase in selectivity is due to the molecular sieving properties of the membrane, this can be explained by the difference in kinetic diameters, as helium has a lower kinetic diameter than hydrogen (Table 3). This explanation also fits the much lower increase in H_2/CH_4selectivity of sample 2p, as methane is smaller than ethane, causing a reduced separation performance. However, the selectivities of the membrane at lower temperatures seem to be inversed, as the highest selectivity at ambient temperature was found for H_2/CH_4, followed by H_2/C_2H_6 and He/C_2H_6. This difference is rather small compared to the difference in the increase of selectivities, especially considering the range of deviation for the measurements.

Sample 3p

In Tables 28-29 and Fig. 60-61, the results of the gas mixture experiments for sample 3p are shown. The numbering of the gas mixtures refers to Table 15 on page 35. All permeances are shown in $10^{-6}\,\mathrm{mol\,s^{-1}Pa^{-1}m^{-2}}$.

Table 28: Permeabilities of the gas mixtures for sample 3p.

T (in °C)	P(1)	P(2)	P(3)
27	0.66	0.64	0.66
100	0.56	0.55	0.56
200	0.48	0.47	0.49
300	0.45	0.44	0.45

Table 29: Real selectivities derived from the gas mixture experiments for sample 3p, as well as calculated Knudsen selectivities.

T (in °C)	$n_{real}(He/C_2H_6)$	$n_{real}(H_2/C_2H_6)$	$n_{real}(H_2/CH_4)$
27	1.65 ± 0.10	1.94 ± 0.19	2.12 ± 0.07
100	1.77 ± 0.13	2.52 ± 0.20	2.31 ± 0.10
200	2.19 ± 0.16	2.79 ± 0.19	2.42 ± 0.09
300	2.51 ± 0.22	3.09 ± 0.22	2.53 ± 0.09
Knudsen	2.7	3.9	2.8

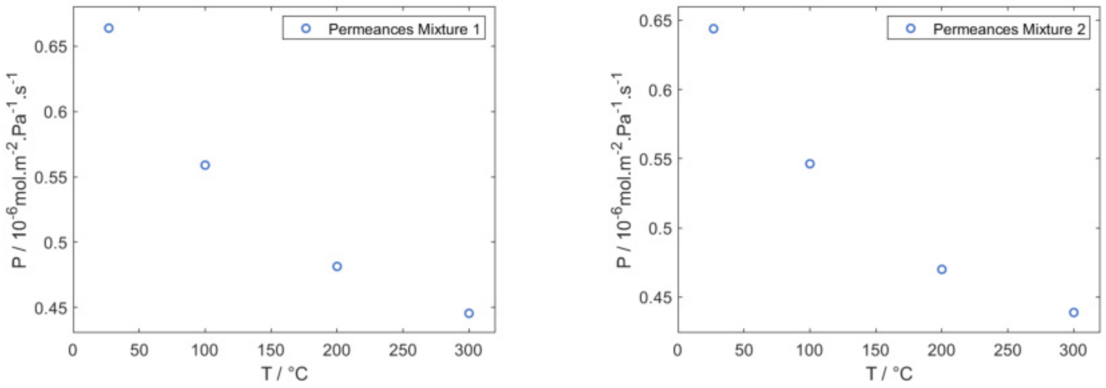

(a) Mixture 1 (85 % N_2, 7.5 % C_2H_6, 7.5% He) (b) Mixture 2 (85 % N_2, 7.5 % C_2H_6, 7.5% H_2)

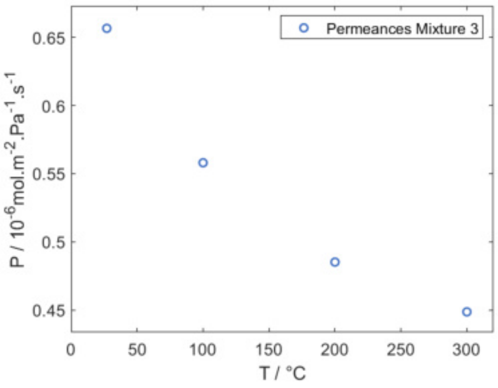

(c) Mixture 3 (85 % N_2, 7.5 % CH_4, 7.5% H_2)

Figure 60: Permeance-temperature plots of sample 3p for the gas mixtures used.

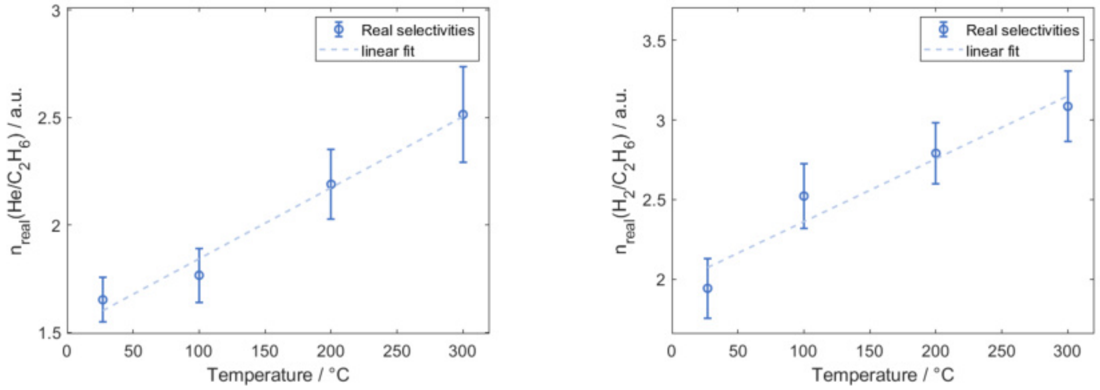

(a) He/C_2H_6 (b) H_2/C_2H_6

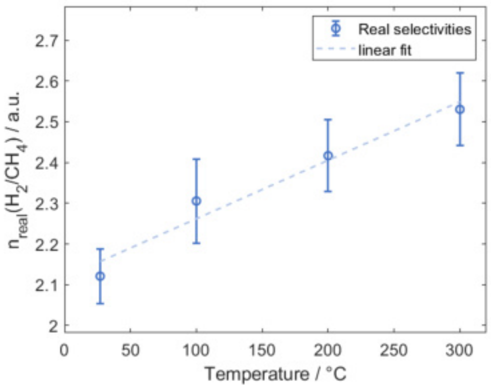

(c) H_2/CH_4

Figure 61: Selectivity-temperature plots derived by using the gas mixtures for sample 3p.

Looking at the permeance values first, again all curves look comparable, even more than for sample 2p. The permeance values are also slightly higher than those of pure nitrogen. The permeance values of sample 3p are approximately twice as high as those of sample 2p, which is in line with the results of the single gas measurements.

Selectivity values did not surpass the theoretical Knudsen values for any gas mixture, regardless of the temperature. The real selectivity increases with higher temperature could also be fitted with linear functions, with fit parameters shown in Table 30.

Table 30: Linear fits of the selectivity-temperature plots for real selectivities of sample 3p.

n_{real}=aT+b	He/C_2H_6	H_2/C_2H_6	H_2/CH_4
a	$3.31\cdot10^{-3}$	$3.95\cdot10^{-3}$	$1.44\cdot10^{-3}$
b	1.51	1.97	2.12
R^2	0.9813	0.9319	0.9596

For all used gas mixtures, the resulting selectivity-temperature plots can be fitted linearly with R^2-values larger than 0.925. These R^2-values are smaller than those of sample 2p, which may be caused by the relatively high standard deviations due to the method. A linear relation can still be assumed, as no trend for a consistent curvature compared to the linear fit could be observed. Unlike for sample 2p, the H_2/C_2H_6 selectivities of sample 3p are higher than the He/C_2H_6 selectivities of sample 3p. This suggests that for sample 3p, the molecular sieving behaviour does not affect the selectivities as much as in sample 3p. This explanation does not fit the lower increase in He/C_2H_6 selectivities of sample 3p, as the increase of selectivities at higher temperatures should only be caused by the molecular sieving qualities of the membrane layer. Therefore most of this can be accounted to general experimental uncertainties, which makes it possible to assume, that helium behaves in a similar way to hydrogen regarding the selectivities. As a consequence, helium can be used as a model gas to roughly simulate and estimate the single gas permeance behaviour of hydrogen.

Again the highest selectivity at ambient temperature could be measured for H_2/CH_4, followed by H_2/C_2H_6 and He/C_2H_6.

5.4.3 Summary of the permeance experiments

Selectivities of the prepared membranes

In Table 31, a summary of the theoretical selectivity values of the measured membranes put into relation with their separation layer qualities is given and compared to the Knudsen values and compared to the selectivity reached by Mori et al.[3] for a similar system.

Table 31: Summary of ideal permselectivities of the prepared membranes.

	1p	2p	3p	1p	2p	3p
Layer thickness (µm)	3	2	0	3	2	0
Crack width (µm)	2.3	0.1	0.2	2.3	0.1	0.2
T	$n_{th}(He/CO_2)$			$n_{th}(He/N_2)$		
27	1.64	1.73	1.46	1.85	2.47	2.21
100	1.96	2.32	1.99	1.93	2.79	2.44
150	2.12	2.69	2.32	1.99	2.99	2.58
200	2.25	2.96	2.57	2.04	3.16	2.68
250	2.35	3.20	2.78	2.07	3.29	2.78
300	2.37	3.38	2.96	2.07	3.40	2.82
350	2.30	3.54	3.08	1.96	3.49	2.92
400		3.68	3.19		3.51	2.91
Knudsen		3.30			2.60	
Mori et al.[3]		2.65			2.41	

The prepared membrane layers show promising selectivity behaviour in single gas experiments, especially at higher temperatures, where sample 2p exceeds the theoretical Knudsen values for He/CO_2 as well as for He/N_2. Even sample 3p, where no separation layer could be observed, exceeded the Knudsen selectivity for He/N_2 in single gas experiments. Only for sample 1p, where large cracks could be observed, Knudsen selectivity could not be reached in any experimental setup. For samples 2p and 3p, the literature selectivity values could be exceeded, albeit with permeances 5 to 10 times lower than those reported by Mori et al.[3]

In Table 32, a summary of the real selectivity values of the measured membranes put into relation with their separation layer qualities is given and compared to the Knudsen values. For the chosen gas mixtures, no comparisons for similar systems could be found in the literature.

Table 32: Summary of real selectivities of the prepared membranes.

	2p	3p	2p	3p	2p	3p
Layer thickness (µm)	2	0	2	0	2	0
Crack width (µm)	0.1	0.2	0.1	0.2	0.1	0.2
T	$n_{real}(He/C_2H_6)$		$n_{real}(H_2/C_2H_6)$		$n_{real}(H_2/CH_4)$	
27	2.12	1.65	2.23	1.94	2.36	2.12
100	2.49	1.77	2.55	2.52	2.51	2.31
200	2.91	2.19	2.87	2.79	2.74	2.42
300	3.71	2.51	3.36	3.09	2.91	2.53
Knudsen	2.7		3.9		2.8	

The promising trend of selectivity behaviour continues for the measurements with gas mixtures, although only sample 2p could exceed the theoretical Knudsen values for He/C_2H_6 as well as for H_2/C_2H_6. A clear trend of higher selectivities at higher temperatures could be observed, suggesting molecular sieving behaviour for the used system. Applying more layers also noticeably improved the selectivities, whereas the permeances decrease by about 50 % when applying three layers compared to two layers, which is a reasonable amount and bearable considering the higher selectivities. The only problem encountered is that cracks in the separation layers limit the potential of the system, as no crackless layers could be achieved.

Troubleshooting

During the test rig experiments, some problems arose, leading to possible future optimisations of the methods described in this work:

- One of the main problems during the single gas measurements is the flattening of the selectivity curves at higher temperatures. A possible reason for that are different experiment durations for the measured gases due to heat conductivity differences and therefore different heating rates.

  This issue could be easily tackled by evacuating the test rig after each measurement and filling it after the target temperature has been reached to create equal measurement conditions for each gas. If this does not prove to be the reason for this trend, other approaches have to be chosen, for example checking the sealing of the graphite ferrules at higher temperatures.

- Although the method for determining the real selectivity showed small nominal deviation for the chosen test gas mixture (methane/helium) in chapter 4.5.6, other gas mixtures show considerably higher standard deviations with the chosen method. A reason for that can be differences in density for the other gases. Given the mixture of hydrogen and ethane, hydrogen has a density fifteen times lower than ethane.[10] Therefore, gas stratification effects could happen inside of the cylinder. This can be checked and avoided by doing method calibrations for each chosen gas mixture.

6 Summary and Conclusions

Microporous ceramic membrane layers were deposited onto a commercially available alumina tubular support by dip-coating into a polysilazane based pre-ceramic polymer, crosslinking and pyrolysis. Using that method, separation layers with a thickness of 2.5 µm could be achieved by using different withdrawal speeds. No other parameters were varied in order to keep the system as constant as possible.

However, during this process, several challenges were faced: At first, infiltration of the mesoporous intermediate layer led to the formation of cracks when using excessively high withdrawal speeds. Even when no cracks could be observed, infiltration of the intermediate layer remained a problem, as more infiltrated support material leads to a decrease in permeabilities, which as a consequence also reduces the separation efficiency of the membranes. Cracks were also formed when performing multiple coatings so that no crack free membrane layer could be obtained. Different approaches were chosen to reduce crack formation, for example the direct coating of a crosslinked sample with a second layer to limit further infiltration of the mesoporous intermediate layer. This led to the formation of even larger cracks. Another approach was to continuously coat the sample with decreasing withdrawal speeds for each step. This led to the most intact layers. The smallest cracks while still applying a separation layer could be obtained by triple coating with withdrawal speeds of 140 mm/min in the first step, 100 mm/min in the second step and 50 mm/min in the third steps, all of which were performed with pure pre-ceramic polymer. This led to a separation layer with a thickness of 2 µm and a crack width of 0.1 µm.

A test rig for measuring permeabilities and selectivities of tubular asymmetric membranes was implemented. A LabVIEW integrated remote solution to control the test rig was programmed and a method for performing single gas permeance measurements and selectivity measurements using gas mixtures was developed.

Two sample membranes with promising separation layer thickness to crack width ratio and one sample membrane without a visible separation layer were prepared for measurement in the test rig to check the effect of a separation layer on the permeance and selectivity of the membranes. The sealing of these membranes was performed using graphite ferrules, which allow measurement temperatures up to 450 °C.

During the measurements, several trends regarding the membrane properties were found. Although cracks could be found in all membranes measured, molecular sieving behaviour could be observed in all of them. This was shown by an increase in selectivity at higher temperatures, leading to selectivities exceeding the Knudsen diffusion values. However, it is very important to limit the crack width to an absolute minimum, as even small cracks can lead to a massive loss of selectivity. It was also found out, that even for the sample without a visible separation layer, molecular sieving behaviour can be observed, showing that already during the infiltration of the intermediate mesoporous layer, microporous regions were formed. It could further be shown that the presence of a separation layer enhances the selectivity of the membrane.

7 Outlook

Preparation of membrane layers

During the preparation of the membrane layers, the biggest challenge was the application of crack-free separation layers. In an effort to obtain such crack-free layers, several additional approaches can be taken.

To optimise the results achievable with dip-coating, parameters other than the withdrawal speeds can be varied. For example, the viscosity of the pre-ceramic polymer can be lowered by diluting the pure liquid with a solvent such as toluene. This together with carrying out more coating steps lead to thinner layers being applied during each step, which should limit crack formation. Another thing would be to try other methods of coating. As the infiltration of the intermediate layer with the pre-ceramic polymer persists to be a problem encountered when using dip-coating, different approaches can be chosen to limit this. One of those would be to increase the viscosity of the polymer in order to avoid the infiltration of the intermediate layers. This can be done by partially crosslinking the polymer before coating the substrate. As the viscosity then would be too high to coat the sample using dip-coating, the sample needs to be coated by smearing the viscous polymer onto the substrate using a doctor blade, making the layer as thin as possible. Preliminary tests were performed to check the potential of this method, which hinted to separation efficiencies 15-20 times higher than the membranes prepared by dip-coating in this work. In the Appendix, the results of some preliminary results are shown.

Although the results of this preliminary membrane test were very promising, difficulties in the preparation of the membrane arose. Especially finding the right timing to quench the crosslinking proved to be difficult. Another issue was the fragility of the layer during sealing. Two other samples prepared this way was damaged during the sealing, as the nut sealing the sample left scratches in the layer, thus making the samples useless for membrane testing.

A way of possibly fixing this is combining this method with dip-coating, as the layers prepared by dip-coating proved to be more robust during the sealing process. For that, either a dip-coating step using diluted polymer solution is added before the coating step to improve the adhesion of the layer, or a dip-coating step using diluted polymer solution is added after the coating step to create a more robust layer.

References

[1] X. Cheng et al. A review of pem hydrogen fuel cell contamination: Impacts, mechanisms, and mitigation. *Journal of Power Sources*, (165):739–756, 2007.

[2] J. Dong et al. Microporous inorganic membranes for high temperature hydrogen purification. *Journal of Applied Physics*, (104):121301, 2008.

[3] H. Mori et al. Fabrication of supported Si_3N_4 membranes using the pyrolysis of liquid polysilazane precursor. *Journal of Membrane Science*, (147):23–33, 1998.

[4] Scholze H. Salmang, H. *Keramik*. Springer, 7 edition, 2007.

[5] R. Riedel et al. Crystallization behaviour of amorphous silicon nitride. *Journal of the European Ceramic Society*, (7(1)):21–25, 1991.

[6] J. Shackleford et al. *CRC Materials Science and Engineering Handbook*. CRC Press, 4 edition, 2016.

[7] Non-oxide ceramics – silicon nitride (Si_3N_4), https://www.ceramtec.com/ceramic-materials/silicon-nitride/. Accessed: 2019-11-06.

[8] Silicon carbide, sic ceramic properties, https://accuratus.com/silicar.html. Accessed: 2019-11-06.

[9] Non-oxide ceramics – silicon carbide (SiSiC/SSiC), https://www.ceramtec.com/ceramic-materials/silicon-carbide/. Accessed: 2019-11-06.

[10] William M. Haynes. *CRC Handbook of Chemistry and Physics*. CRC Press, 92 edition, 2011.

[11] Interrante L. Seyferth, D. *Materials Chemistry: An Emerging Discipline*. ACS, 1995.

[12] P. Greil. Polymer derived engineering ceramics. *Advanced Engineering Materials*, (2(6)):339–348, 2000.

[13] H. Schmidt et al. Micro-/macroporous ceramics from preceramic precursors. *Journal of the American Chemical Society*, (84(10)):2252–2255, 2001.

[14] T. Konegger et al. Asymmetric polysilazane-derived ceramic structures with multiscalar porosity for membrane applications. *Microporous and Mesoporous Materials*, (232):196–204, 2016.

[15] J. (chairman) Rouquerol et al. Recommendations for the characterization of porous solids. *Pure and Appl. Chem.*, (66(8)):1739–1758, 1994.

[16] Z.F. Cui and others. Fundamentals of pressure-driven membrane separation processes. *Membrane Technology*, (2010(1)):1–18, 2010.

[17] N. Ismail and others. Effect of intermediate layer on gas separation performance of disk supported carbon membrane. *Separation Science and Technology*, (52(13)):2137–2149, 2017.

[18] L. Landau and B. Levich. Dragging of a liquid by a moving plate. *Acta Physicochimica U.R.S.S.*, (17):42–54, 1942.

[19] A. Ismail et al. *Gas Separation Membranes*. Springer, 2015.

[20] Y.C. Pan et al. Synthesis of ceramic hollow fiber supported zeolitic imidazolateframework-8 (zif-8) membranes with high hydrogen permeability. *Journal of Membrane Science*, (421-422):292–298, 2012.

[21] Y. Yampolskii. *Materials Science of Membranes for Gas and Vapor Separation*. John Wiley and Sons, 1 edition, 2006.

[22] M. Knudsen. Die gesetze der molekularströmung und der inneren reibungsströmung der gase durch röhren. *Annalen der Physik*, (333(1)):75–130, 1909.

[23] L. Ding and others. Mxene molecular sieving membranes for highly efficient gas separation. *Nature Communications*, (9(155)), 2018.

[24] Mks communications module^{TM} / programmable automation controller 100 user manual. ©MKS Instruments-Automation and Control Solutions, 2015–2017.

[25] E. Fernandez et al. Development of thin pd-ag supported membranes for fluidized bed membrane reactors including wgs related gases. *International Journal of Hydrogen Energy*, (40):3506–3519, 2015.

[26] R.M. Prasad. *Polymer-Derived Microporous Ceramics for Membranes and Sensors for High Temperature Hydrogen Purification and Sensing*. PhD thesis, 2012.

Appendix

Results of the preliminary tests for an alternative coating method as presented in the outlook

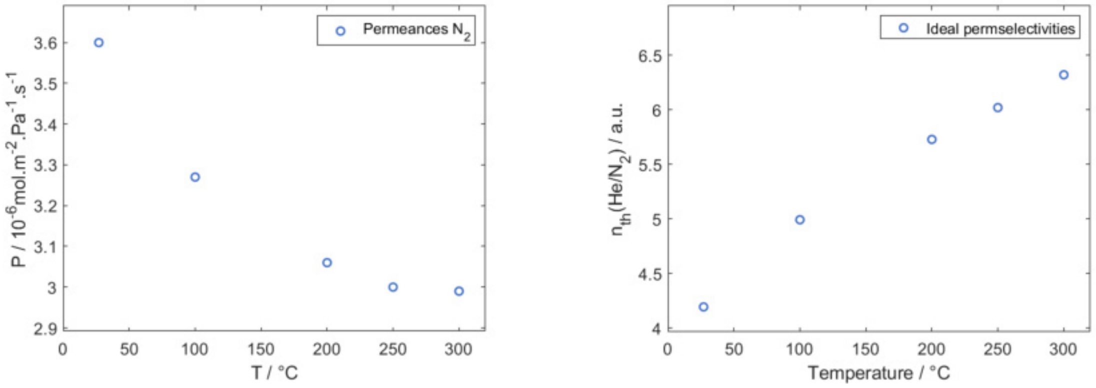

(a) Permeance-temperature plot for N_2 (b) Theoretical selectivity for He/N_2

Figure A.1: Preliminary tests for a sample prepared with the alternative method.

Remaining SEM images

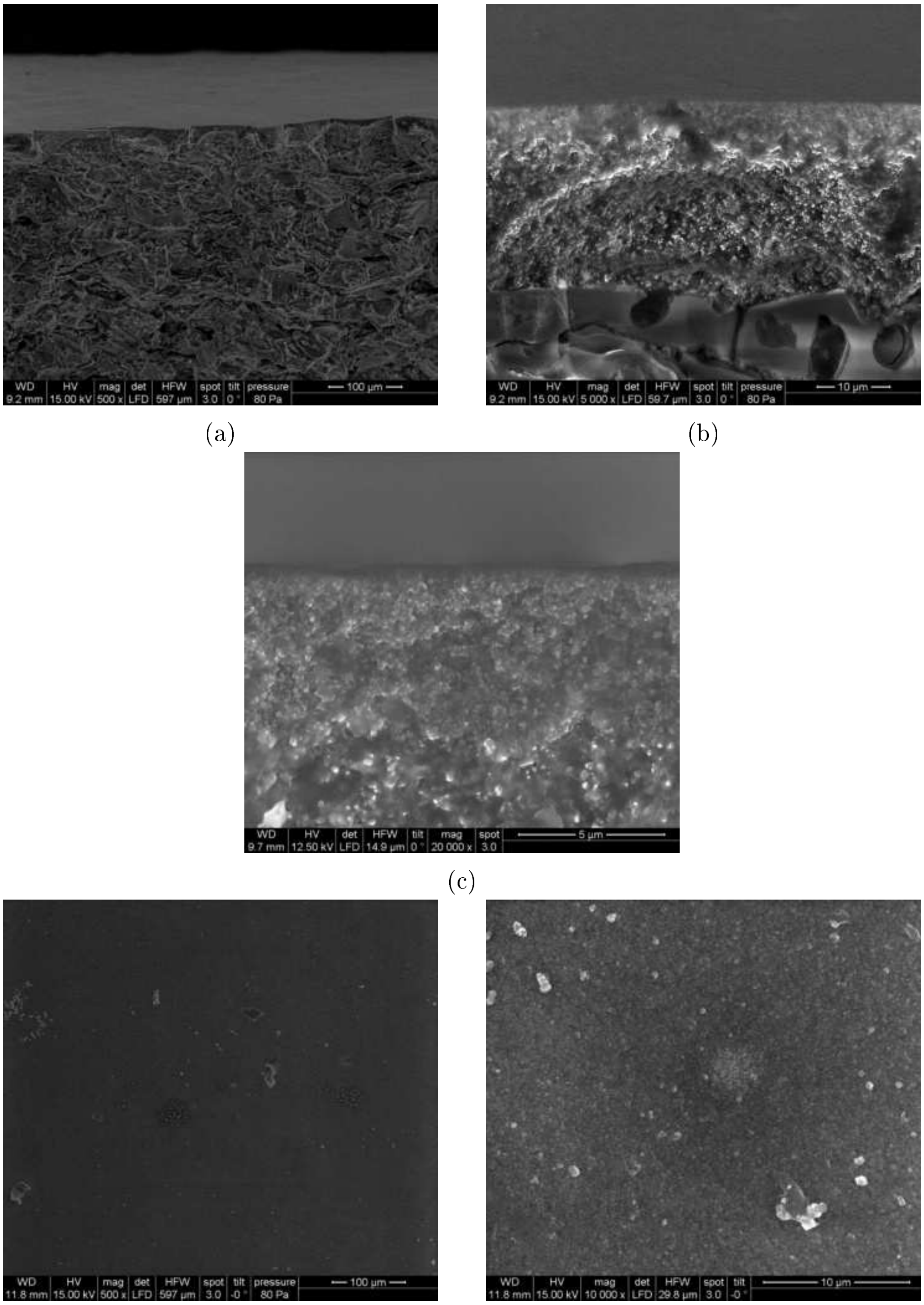

(a) (b)

(c)

(d) (e)

Figure A.2: Remaining images of sample 1 (single coated, withdrawal speed 20 mm/min).
(a)-(c): different magnifications of the cross section.
(d)-(e): different magnifications of the surface.

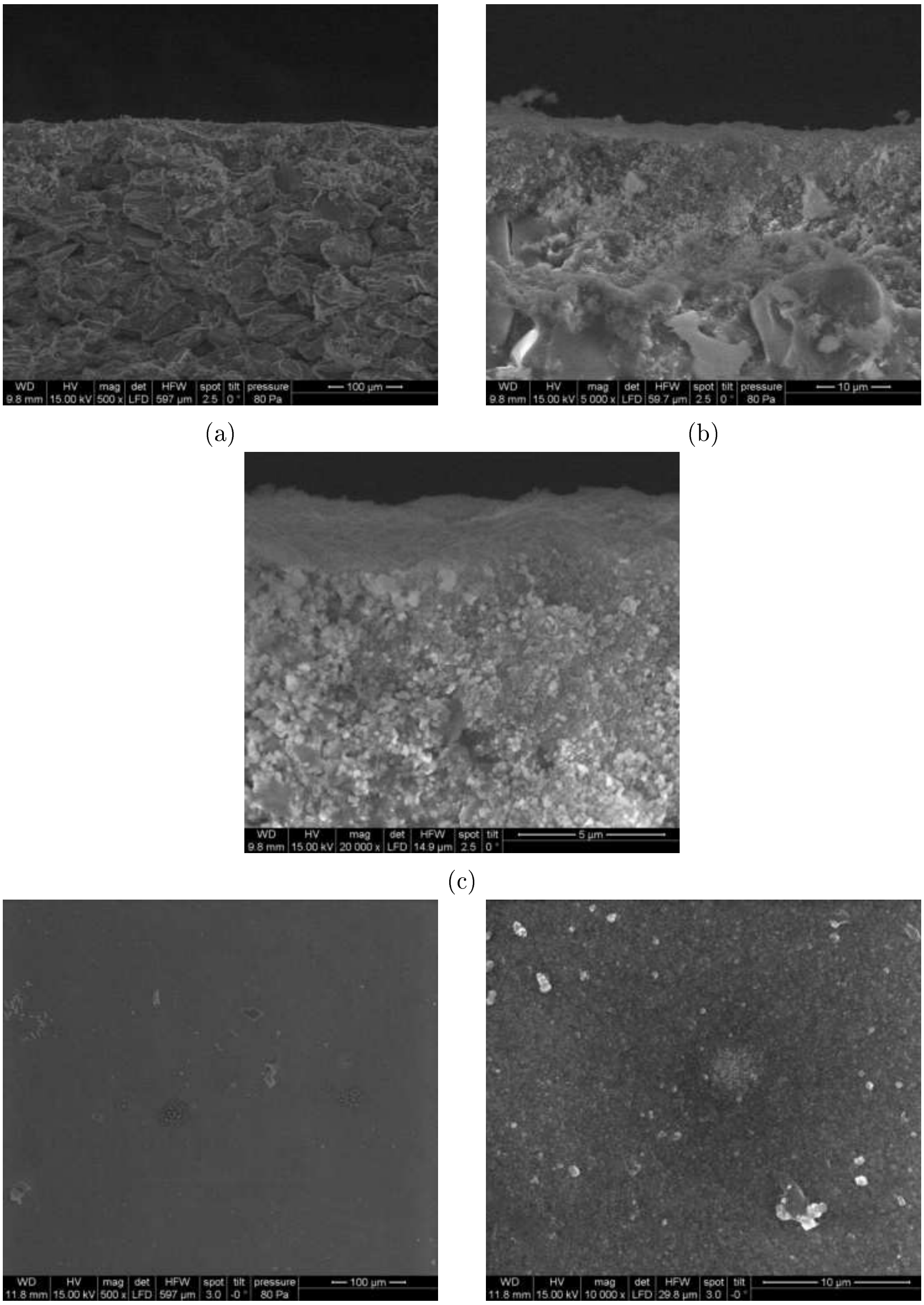

(a) (b)

(c)

(d) (e)

Figure A.3: Remaining images of sample 2 (single coated, withdrawal speed 50 mm/min).
(a)-(c): different magnifications of the cross section.
(d)-(e): different magnifications of the surface.

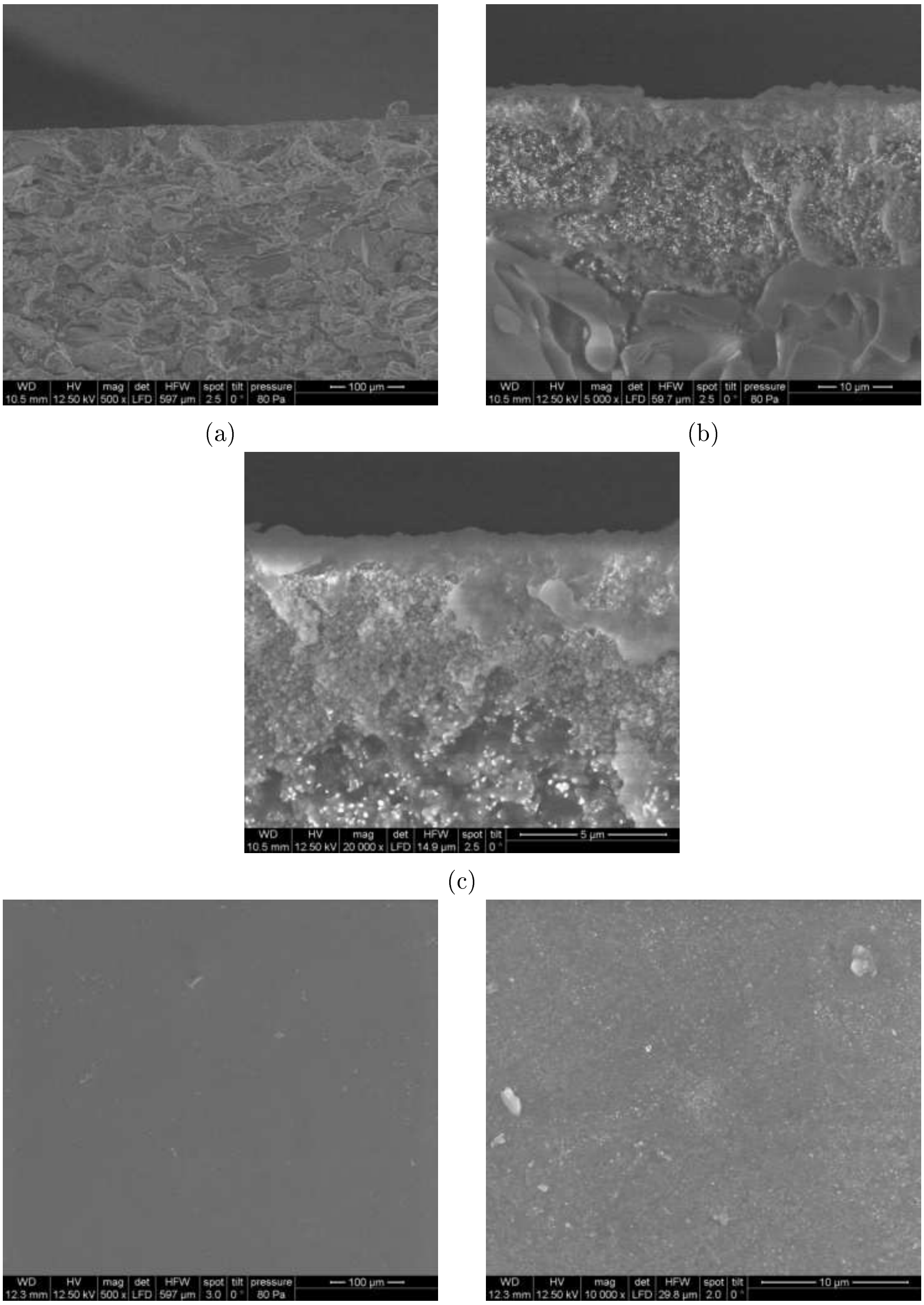

(a) (b)

(c)

(d) (e)

Figure A.4: Remaining images of sample 3 (single coated, withdrawal speed 140 mm/min).
(a)-(c): different magnifications of the cross section.
(d)-(e): different magnifications of the surface.

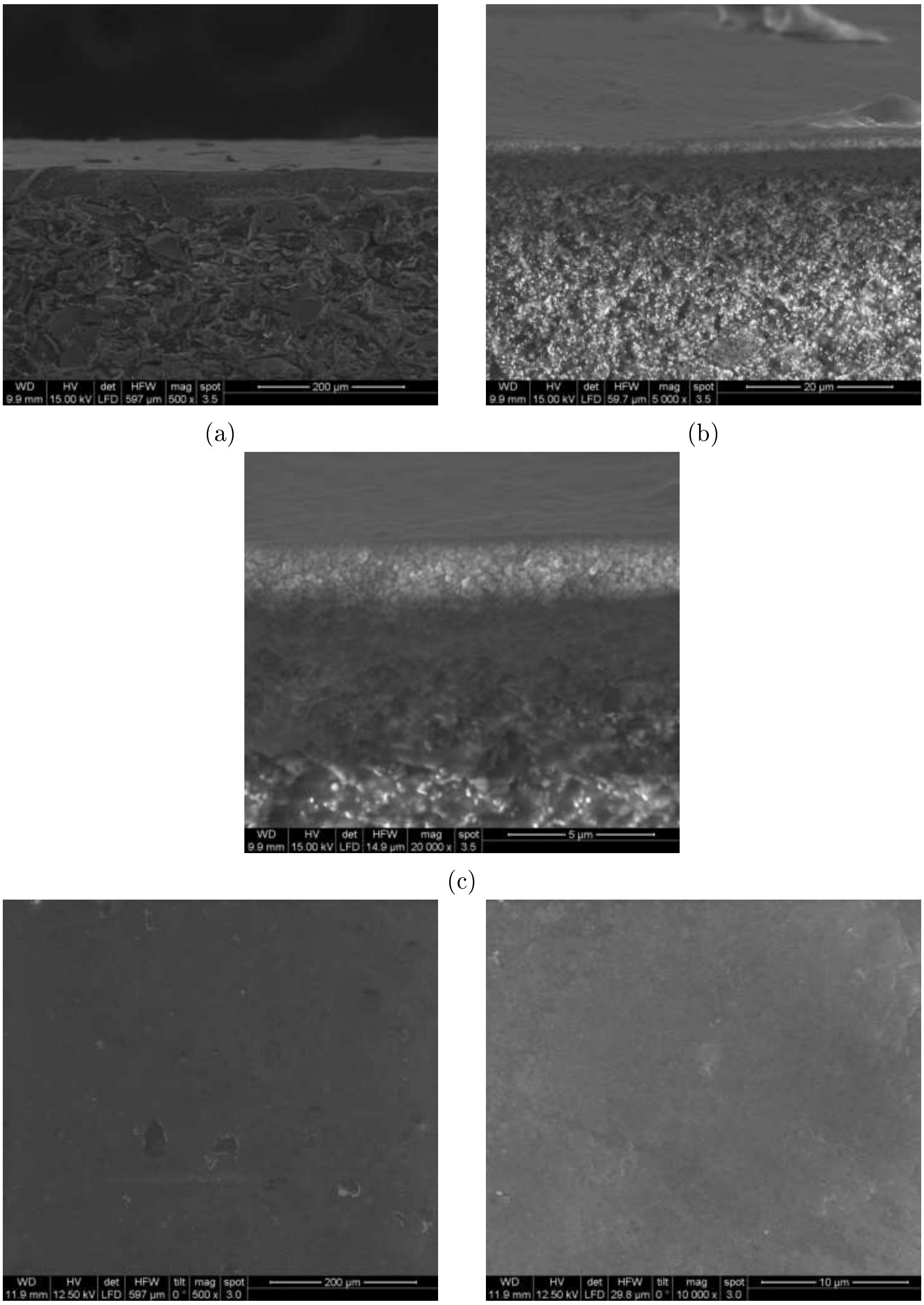

(a) (b)

(c)

(d) (e)

Figure A.5: Remaining images of sample 3 (double coated, first step: 140 mm/min, second step: 50 mm/min).
(a)-(c): different magnifications of the cross section.
(d)-(e): different magnifications of the surface.

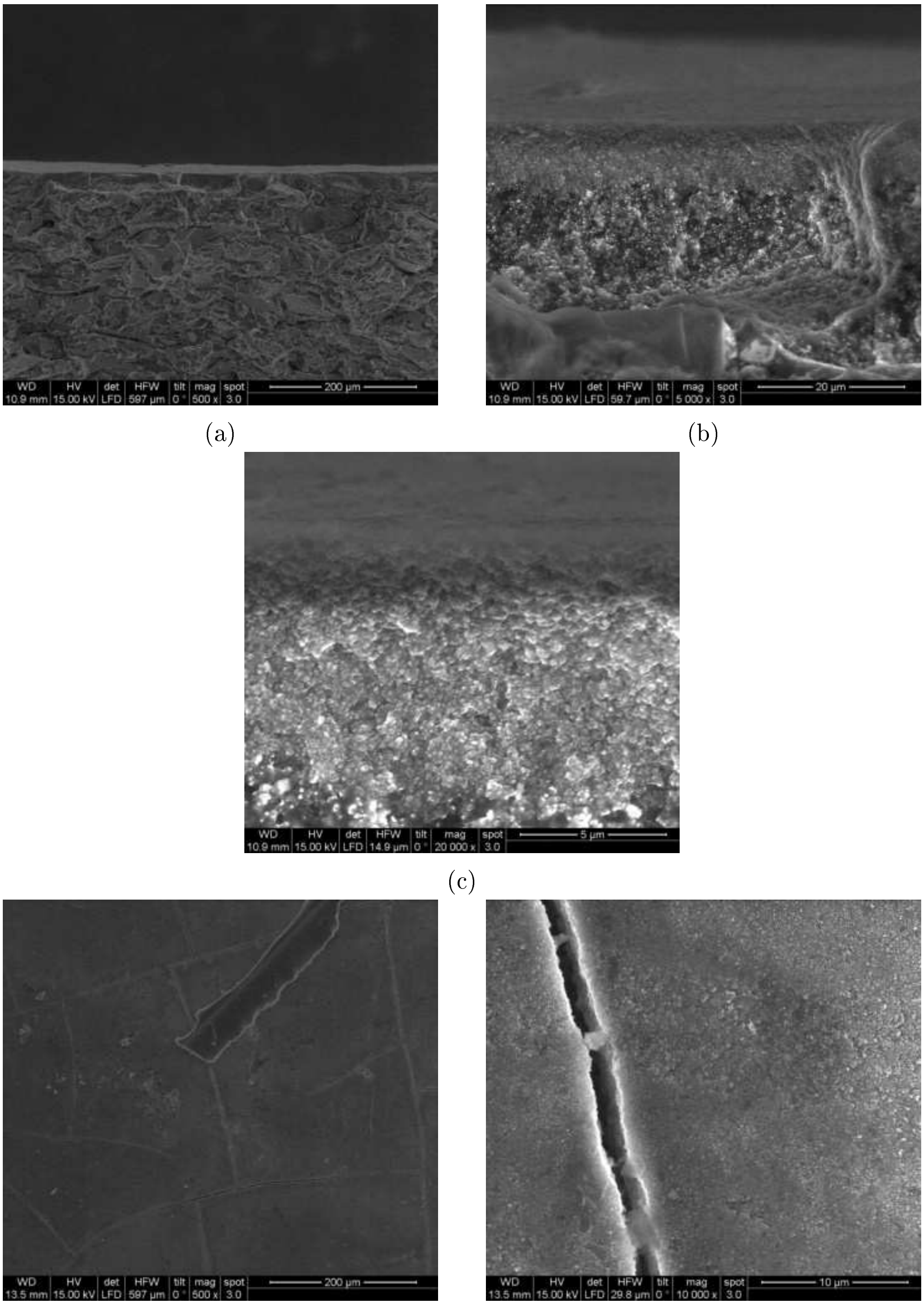

(a) (b)

(c)

(d) (e)

Figure A.6: Remaining images of sample 4 (single coated, withdrawal speed 300 mm/min).
(a)-(c): different magnifications of the cross section.
(d)-(e): different magnifications of the surface.

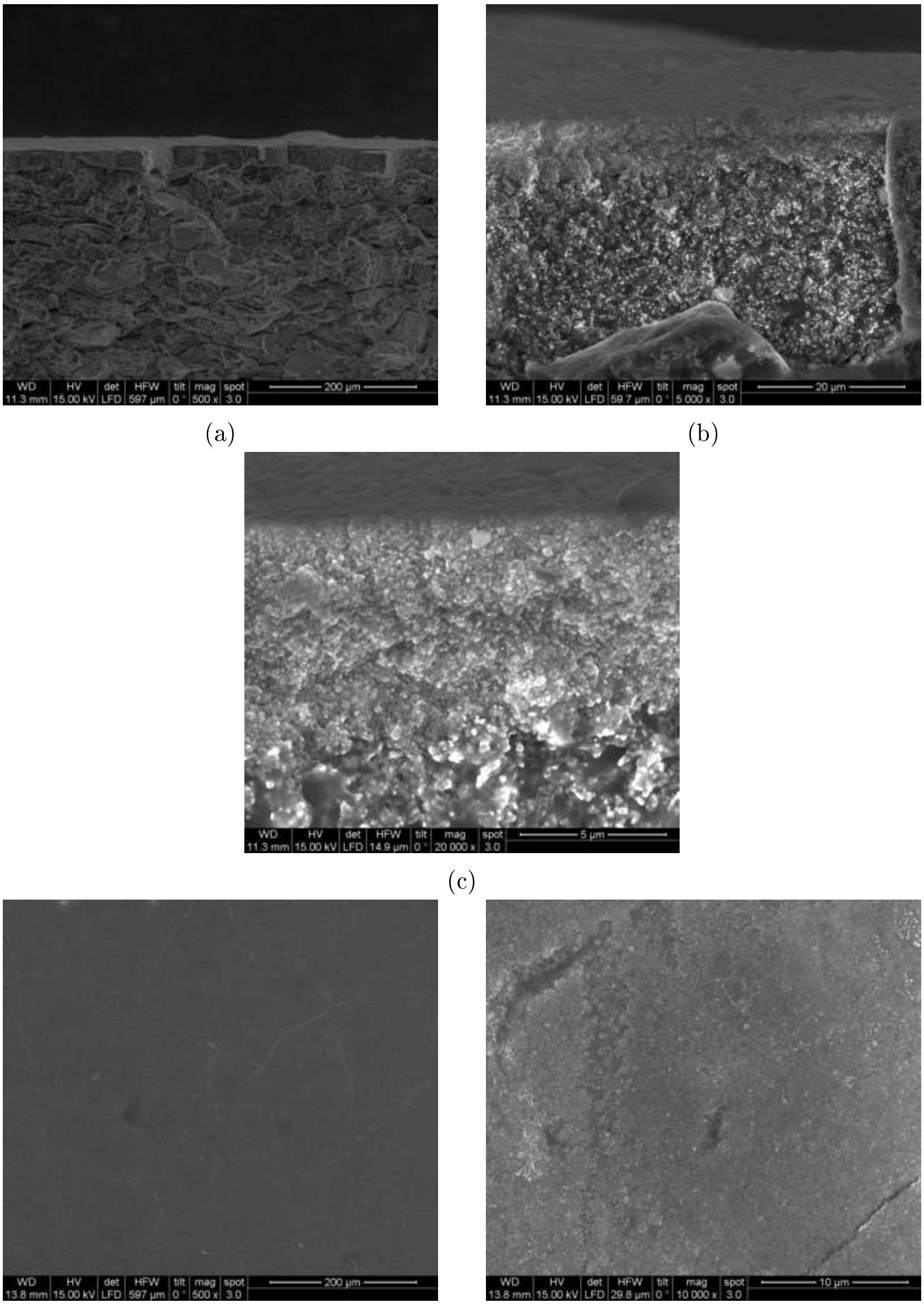

(a) (b) (c) (d) (e)

Figure A.7: Remaining images of sample 5 (single coated with cooled PSZ, withdrawal speed 300 mm/min).
(a)-(c): different magnifications of the cross section.
(d)-(e): different magnifications of the surface.

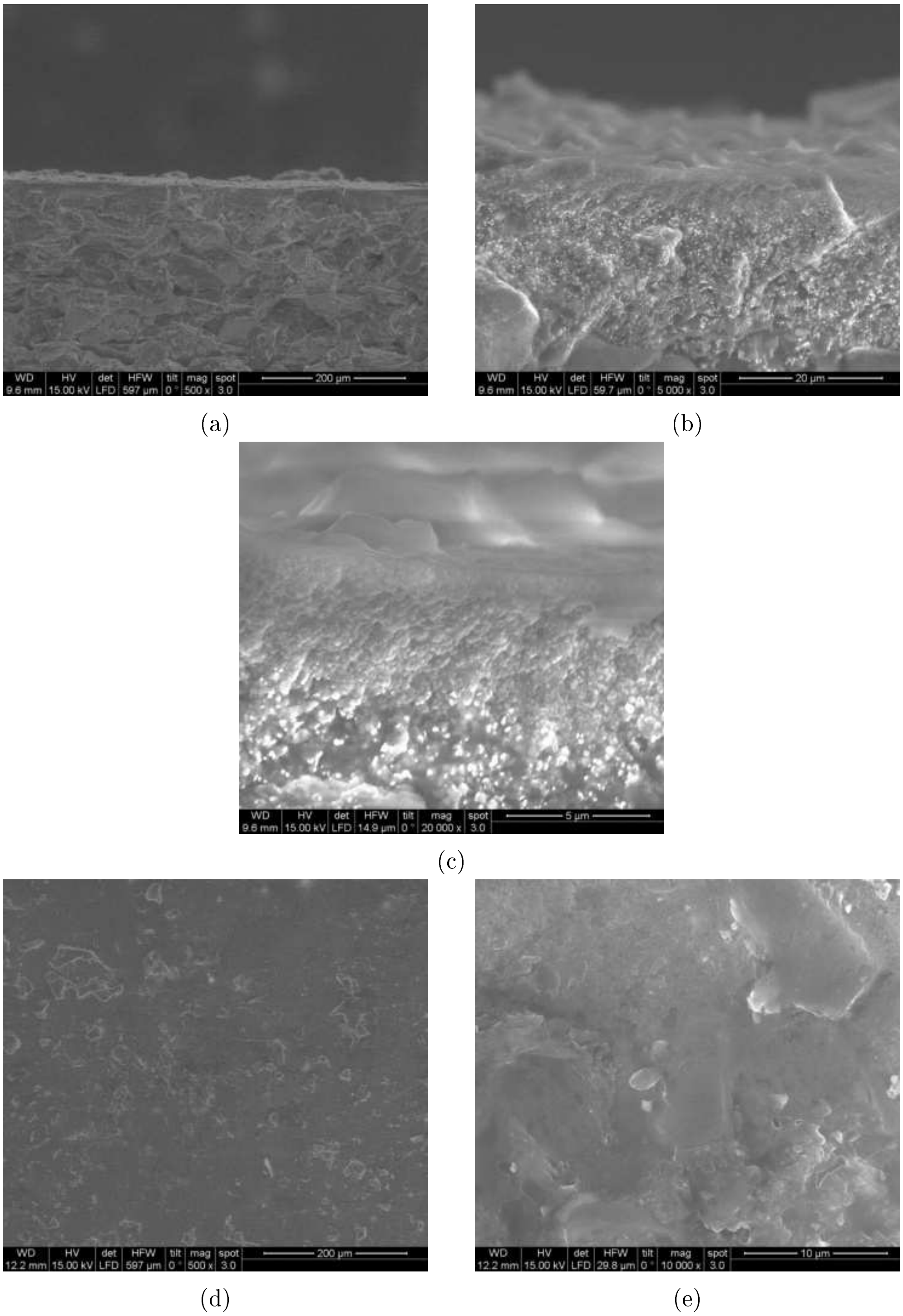

Figure A.8: Remaining images of sample 6 (double coated, first step: 140 mm/min, second step: 100 mm/min).
(a)-(c): different magnifications of the cross section.
(d)-(e): different magnifications of the surface.

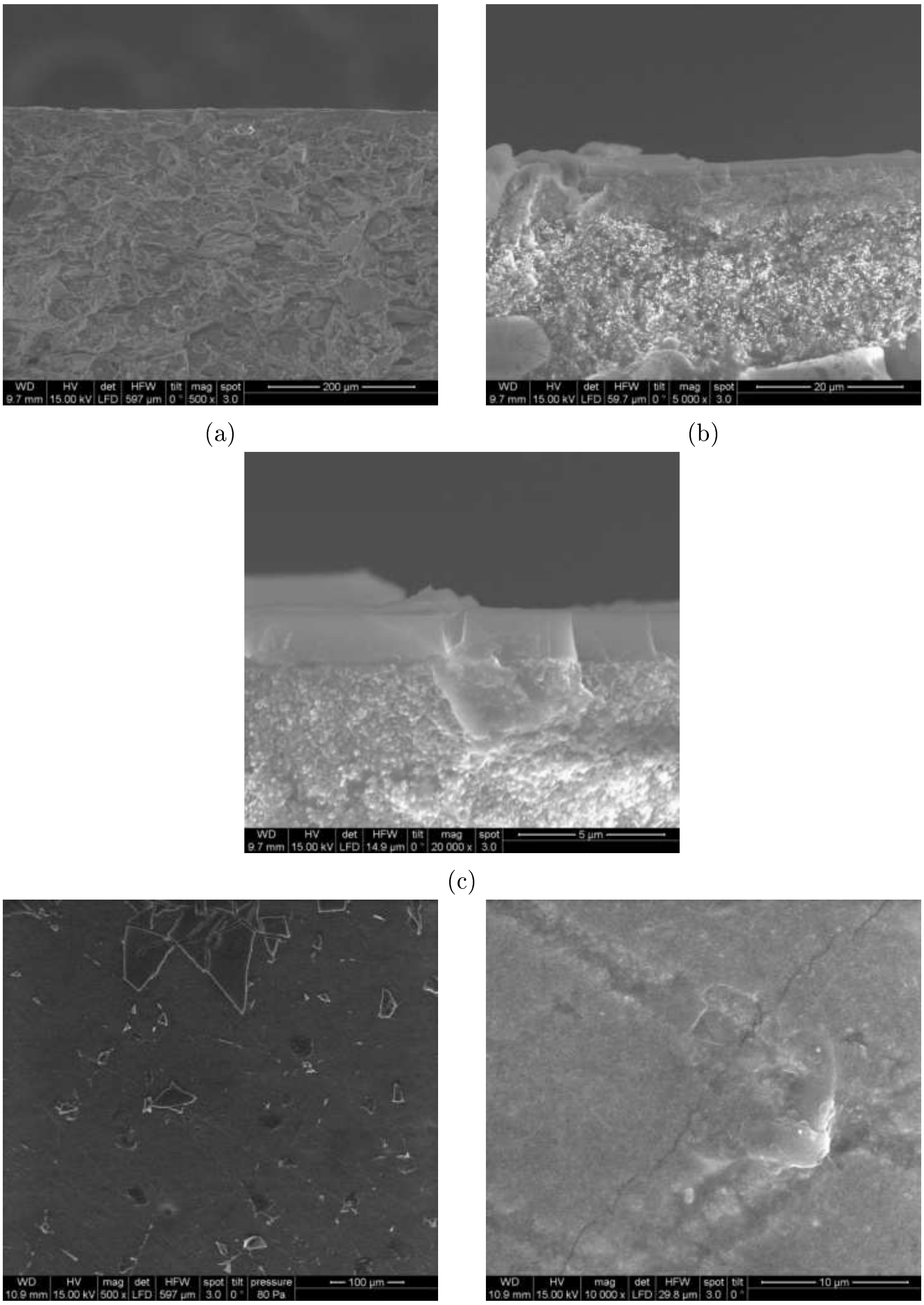

(a) (b)

(c)

(d) (e)

Figure A.9: Remaining images of sample 6 (triple coated, first step: 140 mm/min, second step: 100 mm/min, third step: 50 mm/min).
(a)-(c): different magnifications of the cross section.
(d)-(e): different magnifications of the surface.

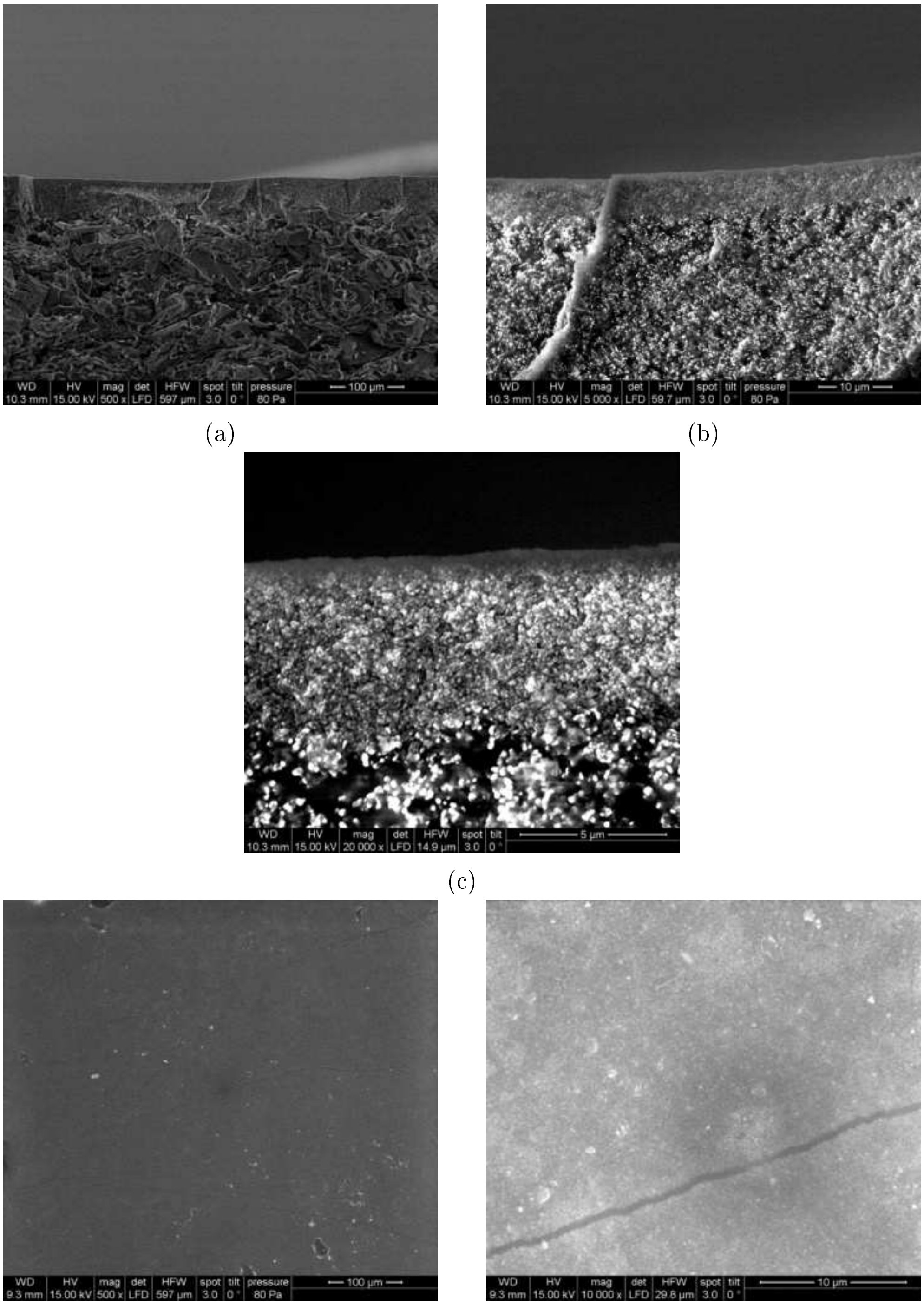

(a) (b)

(c)

(d) (e)

Figure A.10: Remaining images of sample 7 (double coated, first step: 140 mm/min, second step: 120 mm/min).
(a)-(c): different magnifications of the cross section.
(d)-(e): different magnifications of the surface.

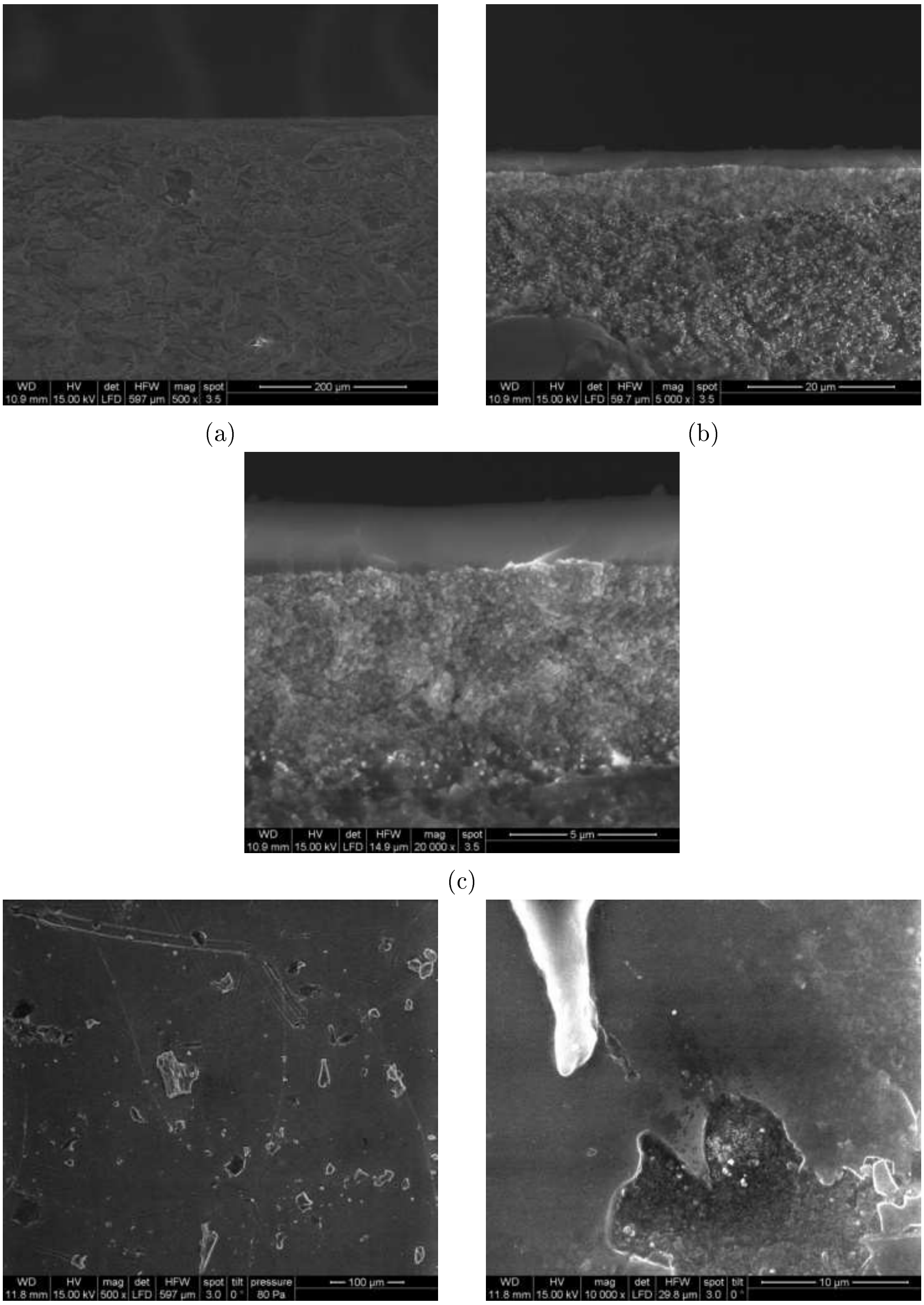

(a) (b)

(c)

(d) (e)

Figure A.11: Remaining images of sample 8 (double coated, first step: 140 mm/min, second step: 140 mm/min).
(a)-(c): different magnifications of the cross section.
(d)-(e): different magnifications of the surface.

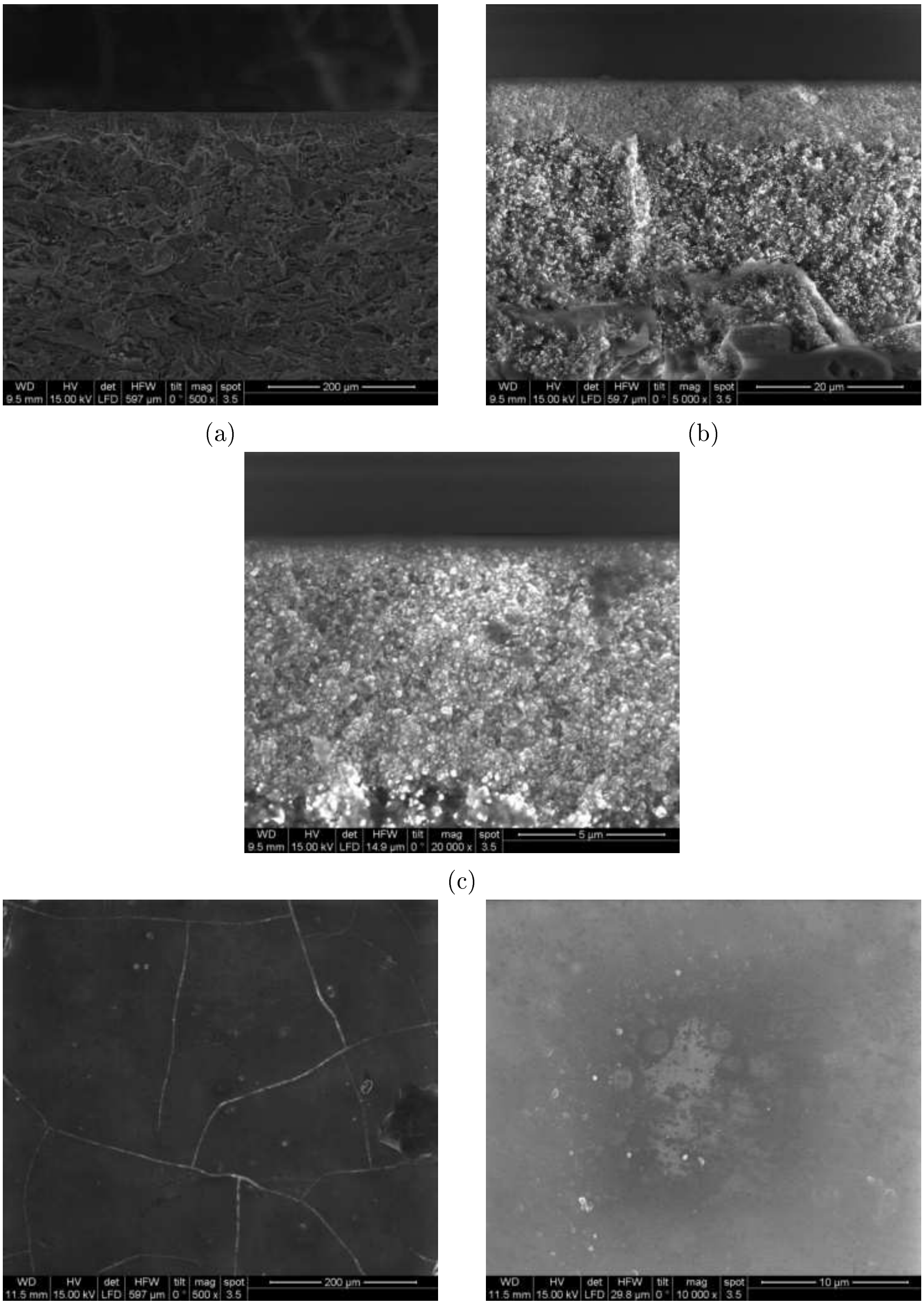

(a) (b)

(c)

(d) (e)

Figure A.12: Remaining images of sample 9 (coated directly onto crosslinked layer, first step: 140 mm/min, second step: 120 mm/min).
(a)-(c): different magnifications of the cross section.
(d)-(e): different magnifications of the surface.

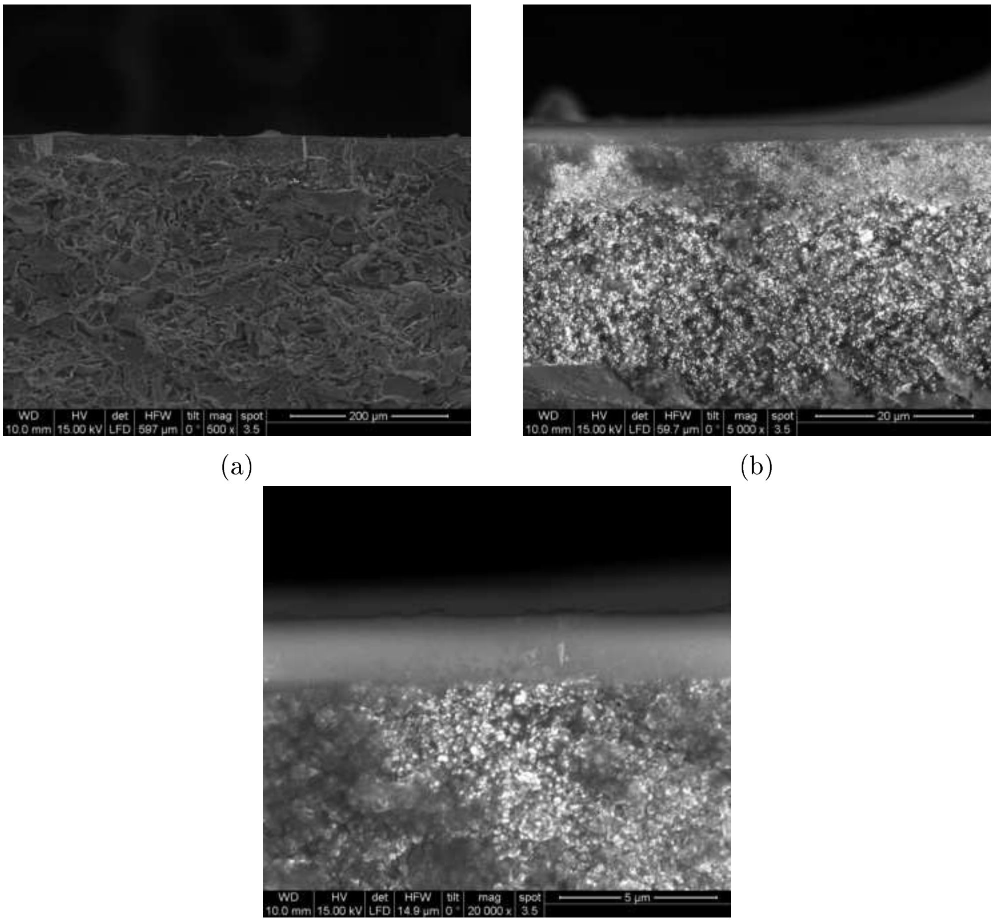

(a) (b)

(c)

Figure A.13: Remaining images of sample 10 (coated directly onto crosslinked layer, first step: 140 mm/min, second step: 140 mm/min).
(a)-(c): different magnifications of the cross section.

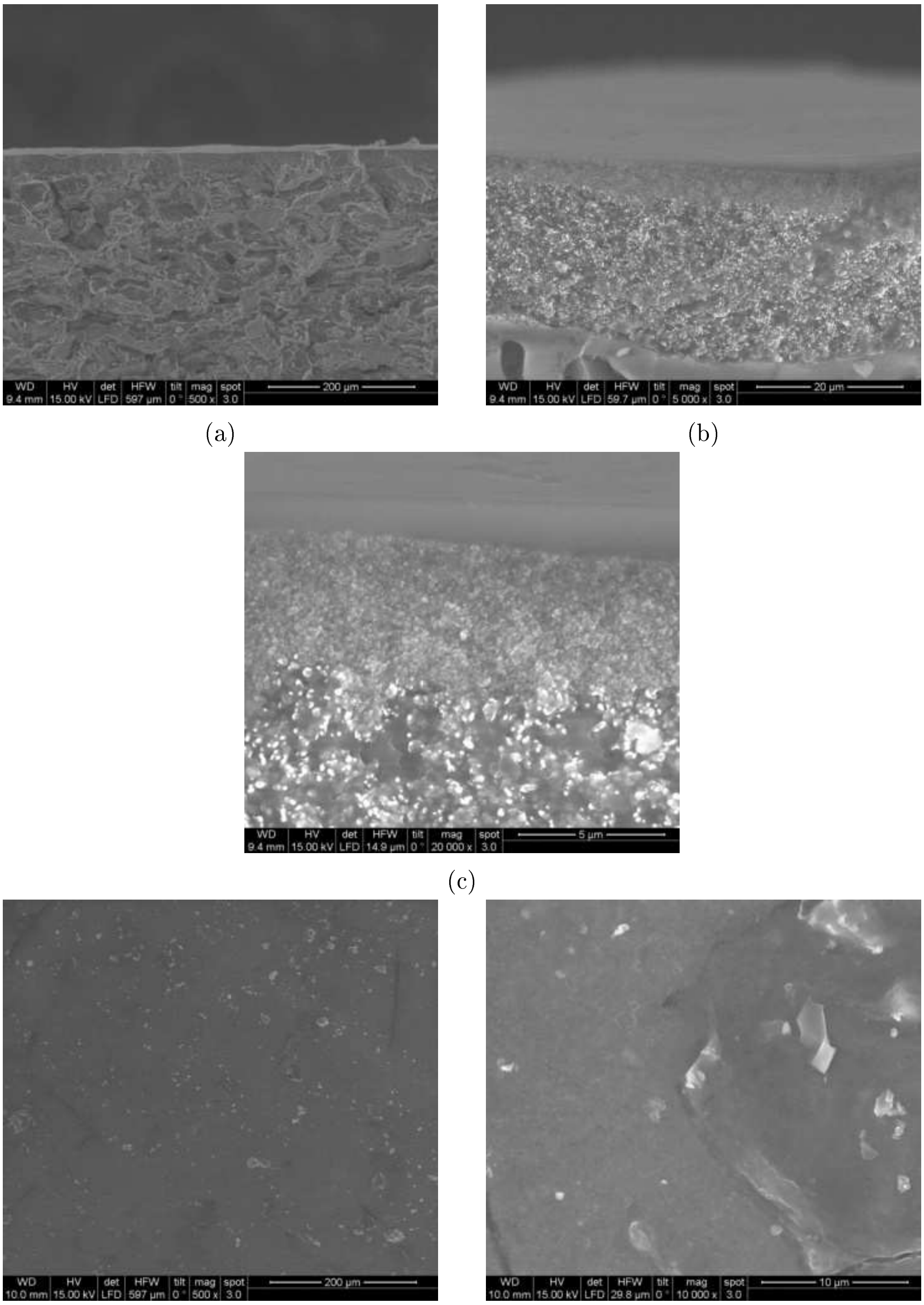

(a) (b)

(c)

(d) (e)

Figure A.14: Remaining images of sample 11 (triple coated, first step: 140 mm/min, second step: 100 mm/min, third step: 140 mm/min).
(a)-(c): different magnifications of the cross section.
(d)-(e): different magnifications of the surface.

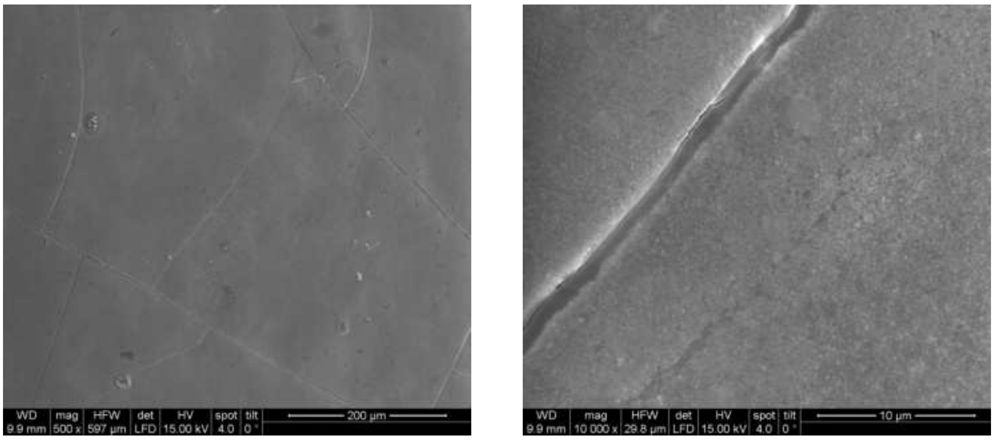

(a) (b)

Figure A.15: Remaining images of sample 1p (double coated, first step: 140 mm/min, second step: 140 mm/min).
(a)-(b): different magnifications of the surface.

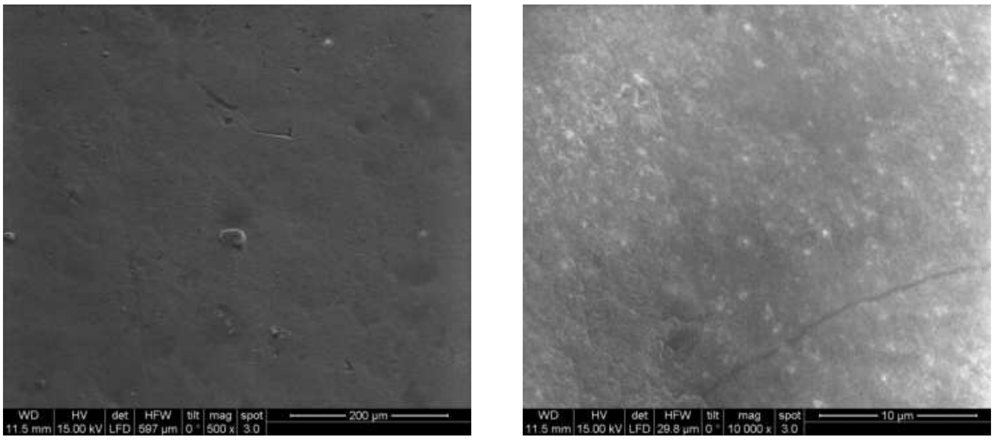

(a) (b)

Figure A.16: Remaining images of sample 2p (triple coated, first step: 140 mm/min, second step: 100 mm/min, third step: 50 mm/min).
(a)-(b): different magnifications of the surface.

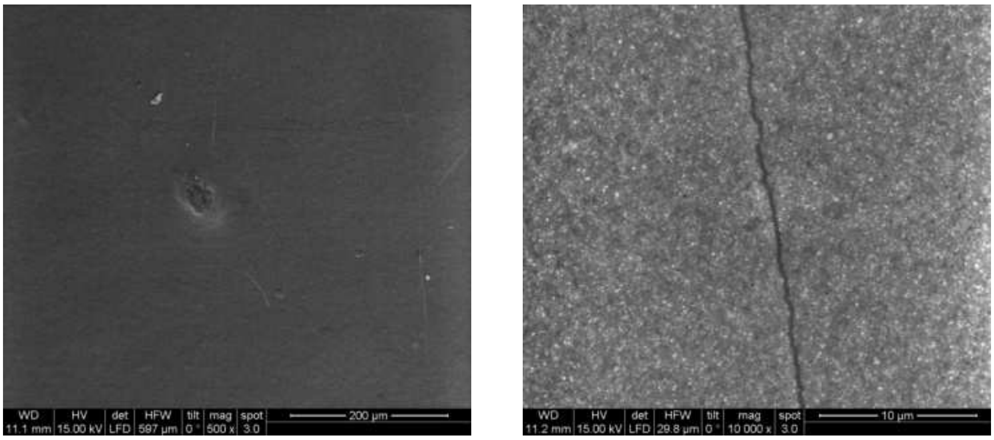

(a) (b)

Figure A.17: Remaining images of sample 3p (double coated, first step: 140 mm/min, second step: 100 mm/min).
(a)-(b): different magnifications of the surface.